

Electrochimica Acta

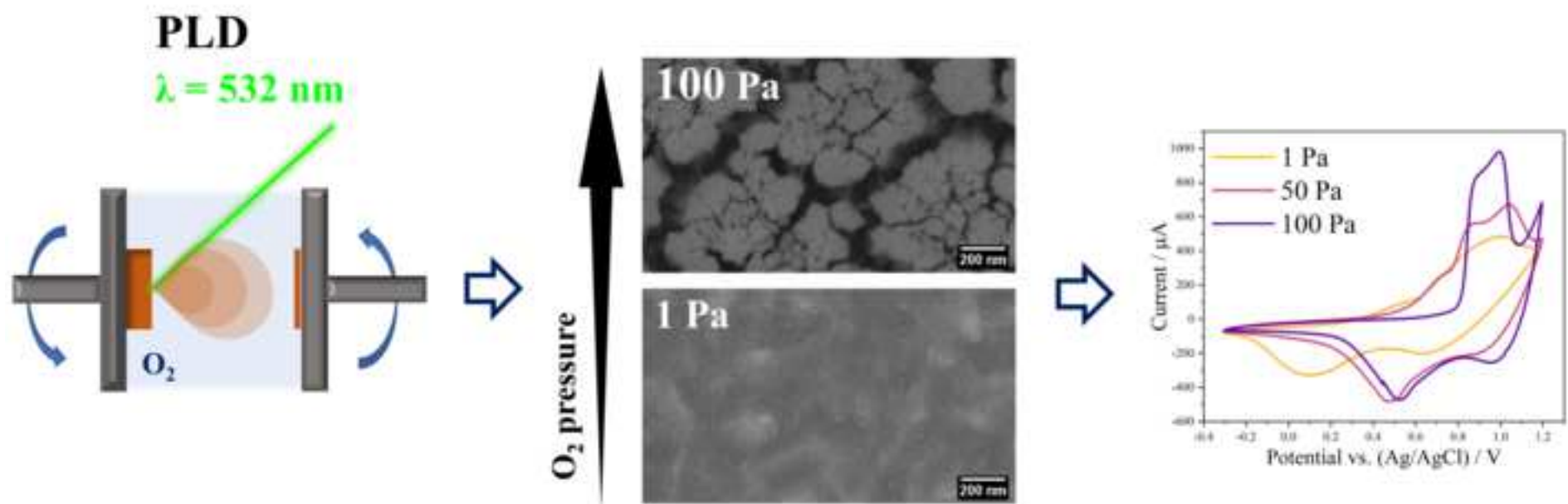
Nanostructured Zn_xMn_{3-x}O₄ thin films by pulsed laser deposition: a spectroscopic and electrochemical study towards the application in aqueous Zn-ion batteries --Manuscript Draft--

Manuscript Number:	EMRS 2022-22-05622R1
Article Type:	VSI: EMRS 2022
Keywords:	Pulsed laser deposition; Zinc-ion batteries; nanostructured cathode materials; ZnMn ₂ O ₄ thin films.
Corresponding Author:	Andrea Macrelli, M.D. Politecnico di Milano Milano, Lombardia ITALY
First Author:	Andrea Macrelli
Order of Authors:	Andrea Macrelli Marco Olivieri Alessio Lamperti Valeria Russo Benedetto Bozzini Marco Menegazzo Gianlorenzo Bussetti Carlo S. Casari Andrea Li Bassi
Manuscript Region of Origin:	ITALY
Abstract:	<p>Aqueous Zn-ion batteries (AZIBs) represent a safe and sustainable technology among the post-lithium systems, though the poor understanding of the material behaviour at the cathode prevents the full development of efficient AZIBs. ZnMn₂O₄ (ZMO) has been considered one of the cathode candidates owing to its analogy to the well-established LiMn₂O₄ cathode for lithium-ion batteries, however its electrochemical mechanism in the presence of Zn ions in aqueous environment is unclear and still debated. In this work, we synthesised nanostructured ZMO thin films by Pulsed Laser Deposition (PLD) and we evaluated, through extensive characterization by microscopic, spectroscopic, and diffraction techniques, how the deposition and annealing conditions affect the film properties. The self-supported nature and the high degree of control down to the nanoscale make a thin film an ideal model system to study the electrochemistry of the material in aqueous solution and to emphasize the impact of the film properties on its electrochemical response. We highlighted the crucial role of the oxygen pressure in the modulation of the film porosity and the combined effect of deposition pressure and annealing temperature to produce a film with tailored properties in terms of morphology, crystallinity, and Zn stoichiometry. A complex redox mechanism involving multiple concurrent reactions and the formation of zinc hydroxide sulphate hydrate (ZHS) was reported, as well as the influence of the film porosity on the voltametric behaviour of the film at higher scan rate. Our results confirm the intricate electrochemical mechanism of the ZMO material, which does not merely involve the Zn²⁺ insertion/extraction but also the crucial participation of Mn²⁺ from the electrolyte, and pave the way for the nanoscale design of engineered ZMO-based electrodes.</p>

Declaration of interests

The authors declare that they have no known competing financial interests or personal relationships that could have appeared to influence the work reported in this paper.

The authors declare the following financial interests/personal relationships which may be considered as potential competing interests:





POLITECNICO
MILANO 1863

Via G. Ponzio 34/3, 20133 Milano, Italy
e-mail: andrea.macrelli@polimi.it

Milano, November -th, 2022

Dear Editor,

please find attached the revised version of the manuscript “*Nanostructured $Zn_xMn_{3-x}O_4$ thin films by pulsed laser deposition: a spectroscopic and electrochemical study towards the application in aqueous Zn-ion batteries*” (Ms. Ref. No.: EMRS 2022-22-05622), authored by A. Macrelli, M. Olivieri, A. Lamperti, V. Russo, B. Bozzini, M. Menegazzo, G. Bussetti, C. S. Casari, and A. Li Bassi. The manuscript was submitted to the Special Issue *Materials for advanced energy storage technologies* of the journal *Electrochimica Acta*, in response to the kind invitation by Dr. Cristina Flox Donoso and Prof. Dr. Olivier Crosnier. In this work, we carried out an in-depth morphological/structural characterization of $Zn_xMn_{3-x}O_4$ (ZMO) thin films produced by Pulsed Laser Deposition (PLD), highlighting the influence of synthesis parameters on film properties, and we investigated the electrochemical behaviour of the films in a typical electrolyte for aqueous Zn-ion batteries (AZIBs).

Following the Reviewer’s comments enclosed in your e-mail dated October 30th, 2022, we carefully revised our work, providing additional relevant electrochemical results coupled with structural analyses and clarifying in detail the objectives of our investigation. Furthermore, we modified some English expressions and formats throughout the text. We would like to thank the Reviewers for their valuable suggestions and comments, which helped us improving the readability, the clarity, and the completeness of our work. Point-by-point responses to each Reviewer comment are supplied in the attached Rebuttal Letter, whereas any change in the original manuscript is highlighted in yellow within the revised manuscript.

We hope that our revisions – based on Reviewer’s comments – make our work suitable for publication in the above-mentioned Special Issue of *Electrochimica Acta*.

Yours sincerely,

Andrea Macrelli
(on behalf of all the co-authors).

Andrea Macrelli, PhD candidate
Micro and Nanostructured Materials Lab (NanoLab)
Department of Energy, Politecnico di Milano
Via G. Ponzio 34/3, 20133 Milano, Italy
E-mail: andrea.macrelli@polimi.it
Telephone: +39 02 2399 6354.



POLITECNICO
MILANO 1863

DEPARTMENT OF ENERGY

Via G. Ponzio 34/3, 20133 Milano, Italy
e-mail: andrea.macrelli@polimi.it

Milano, November -th, 2022

Dear Editor,
Dear Reviewers,

Please find attached a detailed response to Reviewers' comments on our manuscript "*Nanostructured $Zn_xMn_{3-x}O_4$ thin films by pulsed laser deposition: a spectroscopic and electrochemical study towards the application in aqueous Zn-ion batteries*" (Ms. Ref. No.: EMRS 2022-22-05622), authored by A. Macrelli, M. Olivieri, A. Lamperti, V. Russo, B. Bozzini, M. Menegazzo, G. Bussetti, C. S. Casari, and A. Li Bassi and submitted to the Special Issue *Materials for advanced energy storage technologies* of the journal *Electrochimica Acta*.

We would like to thank again every Reviewer for the critical reading of our manuscript and for their valuable suggestions and comments, aimed at improving the quality of our work. The manuscript has been accurately revised according to their recommendations. In the following, we address point-by-point the comments raised by each Reviewer, while any change in the original manuscript is highlighted in yellow within the revised manuscript.

We hope that the revised manuscript is now appropriate for publication in the Special Issue of *Electrochimica Acta*.

Yours sincerely,

Andrea Macrelli
(on behalf of all the co-authors).

Andrea Macrelli, PhD candidate
Micro and Nanostructured Materials Lab (NanoLab)
Department of Energy, Politecnico di Milano
Via G. Ponzio 34/3, 20133 Milano, Italy
E-mail: andrea.macrelli@polimi.it
Telephone: +39 02 2399 6354.



POLITECNICO
MILANO 1863

REPLIES TO REVIEWERS

Here below, we provide the answer (**in blue**) to each comment raised by the Reviewers.

Reviewer #3: This manuscript reported the "Nanostructured $Zn_xMn_{3-x}O_4$ thin films by pulsed laser deposition: a spectroscopic and electrochemical study towards the application in aqueous Zn-ion batteries". A method for the synthesis of ZMO is reported, but the related materials are somewhat lacking in electrochemical tests. This manuscript presents some important results that will contribute to the development of cathodes for AZIBs. Some issues should be addressed before possible publication as follows:

1. Some English expressions and formats need to be modified, for example: In the paper, " Zn^{2+} ions" should be "Zn ions" or " Zn^{2+} ".

In line 5 of the abstract, The "aqueous Zn^{2+} ion" is confusing, this sentence should be rewritten. The abbreviation "aqueous zinc ion batteries" is more scientifically referred to as "AZIBs".

Thank you, we have fixed these issues.

2. Some related works maybe are useful for support and background, such as Energy Storage Mater., 51 (2022) 733, Small Methods 2022, 2200597, J Energy Chem 75 (2022) 135.

Thank you, we have considered and examined the suggested references, which deal with the issues with the Zn metal anodes in AZIBs and with the promising strategies to improve their stability. We have referenced two of them in the Introduction of the revised manuscript.

3. Abstract logic needs to be revised and representative experimental results analysis added.

Thank you, we have revised the Abstract.

4. Introduction is too long and needs to be trimmed.

Thank you, we have revised the Introduction.

5. A simple preparation flow chart can make your preparation process clearer.

A simple preparation flow chart for samples aimed at the electrochemical characterization has been added (see Fig. 6 in the revised manuscript).

6. There are too few relevant electrochemical tests, please explore the cell with ZMO as cathode more carefully.

Thank you for this comment. We added a combined electrochemical-Raman analysis to provide further insight into the material transformations during the electrochemical polarization, in



POLITECNICO
MILANO 1863

particular upon the sequential application of selected potentials. Nevertheless, we would like to emphasize that our work, following the same kind of approach reported in Ref. 94 (now Ref. 81 in the revised manuscript), is mainly focused on the behaviour of the ZMO material during the electrochemical cycles in the ZMS aqueous electrolyte (complementing the electrochemical measurements with microscopic and spectroscopic analyses), rather than to the performance of the ZMO film as cathode in a real AZIB. The careful optimization of the film properties will help us focusing in detail on realistic full cells in future dedicated works.

7. The format of the references is not uniform, e.g., Ref. 78.

Thank you for this comment. However, Ref. 78 (now Ref. 80 in the revised manuscript) does not refer to a research article paper but to a book chapter. We have followed the instructions for References in the Guide for Authors for the journal *Electrochimica Acta*.



Reviewer #4: This paper reported the synthesis of nanostructured ZMO thin films by pulsed laser deposition (PLD), and investigated the effect of deposition pressure and annealing temperature on the morphology, crystallinity, and Zn stoichiometry of ZMO thin films. Although this work gave us a clear vision that how the PDL synthesis process affect the structure of ZMO thin film, the relationship between the structure and the electrochemical performance are still unclear, and the conclusions are lack of convincing evidence. I think it is more suitable for materials special journal rather than EA. The detailed comments are listed below:

1. In the abstract, the author mentioned that " its electrochemical mechanism in the presence of aqueous Zn^{2+} ions is unclear and still debated", however, the mechanism was still not clarified in this work.

Thank you for this comment. We agree that our manuscript does not provide a definitive mechanistic understanding of the complex electrochemical behaviour of ZMO in aqueous electrolyte, but this would be the goal of a long-term, multi-technique research, far beyond the aim of our work. Indeed, we are convinced that we are contributing significantly to the clarification of several aspects, so far not considered in the literature. In particular, as we have restated in the Introduction, we strongly focus on the material point of view – providing a detailed investigation into the impact of the synthesis parameters on the resulting film features –, and we highlight how a thin film with controlled properties can be an ideal candidate to study its electrochemical behaviour in simple cells without the influence of any additive. This approach – methodologically akin to the one reported in Ref. 94 (now Ref. 81 in the revised manuscript) – lays the foundations for a future work fully dedicated to Zn full-cells with ZMO cathodes.

2. Figure 1 and 3, the thickness of the electrode should be marked in the SEM images.
Thank you. For the clarity of the Readers, we have marked the ZMO film thickness with respect to the Si substrate in both Fig. 1a and Fig. 3a.

3. Figure 3b, the author claimed that "the crystal size does not play the major role in affecting the Raman spectra of annealed ZMO thin films", however, the resulted ZMO thin films indeed have different crystal sized under different pressure. In addition, the author claimed that "the Raman shift might be attributed to slight changes in the relative contents of metallic elements in the overall manganite structure", are there any evidences to support this conclusion?

Thank you for this comment. Concerning the first remark, it is true that the crystal size of the ZMO thin film is affected by the deposition pressure and it is decreasing in the films as the O_2 pressure increases. However, it is quite clear that the crystal size is not the main cause for the changes observed in the Raman spectra. Indeed, as reported in Ref. 89 (now Ref. 91 in the revised manuscript) for the crystallite size effect on the Raman spectrum of spinel Mn_3O_4 (which is isostructural to ZMO), a decrease of the grain size results in a red-shift and broadening of the main A_{1g} peak. In our spectra, the trend is opposite: we observe an overall blue-shift of the peaks with increasing O_2 deposition pressure (i.e., decreasing crystal size), which is not accompanied by a significant broadening (see Fig. 3c and Fig. S4c). In our opinion, the changes observed in



the Raman spectra in terms of blue-shift, width, and relative intensity ratios can be attributed to a combination of multiple effects induced by the O₂ deposition pressure, e.g., morphology, slight stoichiometric changes, and micro-strains, rather than to the crystal size only.

Focusing on your second remark, we have emphasized that a very similar trend in the Raman spectra of Zn_xMn_{3-x}O₄ samples was reported in Ref. 44 (now Ref. 46 in the revised manuscript), in which the *x* value was intentionally varied during the solid-state synthesis. Therefore, the exact stoichiometry of our films (affected by the deposition conditions and retained after annealing) could play an important role in impacting on the Raman spectra. So far we have observed slight, but consistent, changes in the Zn and Mn atomic contents by EDXS and we are undertaking a more detailed chemical analysis, also accounting for chemical-state effects (e.g., XPS), to deepen these aspects in a future publication.

4. There are too many structure characterizations, instead the electrochemical measurements are insufficient.

Thank you for this comment. We added a combined electrochemical-Raman analysis to provide further insight into the material transformations during the electrochemical polarization, in particular upon the sequential application of selected potentials. In analogy with the approach reported in Ref. 94 (now Ref. 81 in the revised manuscript), our electrochemical data are complemented by SEM and Raman spectroscopy analyses on aged samples, in order to pinpoint the structural/phase modifications of the material induced by the electrochemical tests.

5. The author stated that "CV measurements in this work indicated that a complex redox behaviour in aqueous electrolyte containing both Zn²⁺ and Mn²⁺, which may involve multiple simultaneous processes such as Zn²⁺ insertion/extraction, H⁺ insertion/extraction, ZHS precipitation/dissolution, and MnO_x deposition". However, the complex redox mechanisms have been revealed in previous works, there are no new viewpoints in this work.

It is not the aim of the present work to disclose new electrochemical processes, but rather to place the observed voltammetric behaviour of the novel materials synthesized and investigated in the framework of the current understanding of the aqueous electrochemistry of manganese-based oxides, in particular in the presence of Zn²⁺. It is worth noting that some of the authors of the present manuscript have recently published a comprehensive and systematic research in this field (see Ref. 81 in the revised manuscript), that provides the electrochemical background to the present study.



Reviewer #5: In this manuscript, the authors reported the PLD deposition of nanostructured $Zn_xMn_{3-x}O_4$ thin films and optical and electrochemical performance of the films. The topic of the manuscript is very interesting and the authors give the potential applications of the films in aqueous ZIB. I think the manuscript can be accepted after minor revision.

- 1) The part of conclusion for the text should be concise.

Thank you, we have revised the Conclusions.

- 2) The samples annealed at 600 °C and higher show the porous structure, especially observed in cross-sectional view. Unfortunately, the electrochemical performances of them were not investigated.

The film porosity is predominantly controlled by the O_2 deposition pressure, while the annealing temperature affects the grain size and the overall crystalline quality (see, e.g., Fig. S5). The cross-sectional SEM images of Fig. 3a refer to ZMO films grown on Si substrates in vacuum and at 10, 50, and 100 Pa of O_2 (thus exhibiting an increasing degree of porosity), and air-annealed at 600 °C for 3h. In fact, we have not tested the electrochemical performance of the particular set of these specific samples annealed at 600 °C (and higher temperature), because the aim of these specific annealing tests was a more general investigation of the crystallization process. As far as electrochemical studies of PLD-grown and crystallized samples are concerned, we have selected air-annealing at 500 °C for 2h because these conditions, on the one hand, ensure high crystallinity, and, on the other hand, would not result in softening of the conductive FTO-coated glass employed as the current collector. The impact of this temperature difference on film morphology is negligible in the context of this study because this is determined by the O_2 deposition pressure (compare the SEM top-view images of Fig. S3 for samples annealed at 600 °C and of Fig. S8c for samples annealed at 500 °C). Therefore, the electrochemical results reported in Section 3.4 (Figs. 7–10 in the revised manuscript) were also acquired on porous samples grown at 50 and 100 Pa of O_2 .

- 3) The manuscript shows the electrochemical performance of the films in half batteries. For readers, we really want to know how its performance in aqueous Zn-ion batteries.

Thank you for this comment. We agree that electrochemical tests in full-cell configuration (i.e., with a Zn metal anode) would be highly interesting for a real application of ZMO material in AZIBs. However, this work is primarily aimed at showing how the pure ZMO material can be synthesized in a controlled way in the form of thin films that can be characterized electrochemically. The investigation in full AZIBs of the behaviour of ZMO films with the optimal morphology disclosed in this work will be the topic of a future dedicated work.

- 4) The electrochemical stability for the film may be supplied.

The electrochemical analyses on our ZMO thin films were carried out according to Ref. 94 (now Ref. 81 in the revised manuscript). The potential range is intentionally larger than the one typically



POLITECNICO
MILANO 1863

used in operating AZIBs, in order to span multiple Mn oxidation states (from Mn^{2+} to Mn^{4+}) and to provide a more complete picture about the redox response of Mn-based materials.

1
2
3
4
5
6
7
8
9
10
11
12
13
14
15
16
17
18
19
20
21
22
23
24
25
26
27
28
29
30
31
32
33
34
35
36
37
38
39
40
41
42
43
44
45
46
47
48
49
50
51
52
53
54
55
56
57
58
59
60
61
62
63
64
65

Nanostructured $Zn_xMn_{3-x}O_4$ thin films by pulsed laser deposition: a spectroscopic and electrochemical study towards the application in aqueous Zn-ion batteries

Andrea Macrelli^{a,*}, Marco Olivieri^a, Alessio Lamperti^b, Valeria Russo^{a,c}, Benedetto Bozzini^d,
Marco Menegazzo^e, Gianlorenzo Bussetti^e, Carlo S. Casari^{a,c}, Andrea Li Bassi^{a,c}

^a Micro and Nanostructured Materials Lab (NanoLab), Department of Energy, Politecnico di Milano, Via G. Ponzio 34/3, 20133 Milano, Italy;

^b Institute for Microelectronics and Microsystems (IMM), Consiglio Nazionale delle Ricerche (CNR), Unit of Agrate Brianza, Via C. Olivetti 2, 20864 Agrate Brianza (MB), Italy;

^c Center for Nano Science and Technology (CNST), Istituto Italiano di Tecnologia (IIT), Via G. Pascoli 70/3, 20133 Milano, Italy;

^d Battery Materials Engineering Laboratory (BMEL), Department of Energy, Politecnico di Milano, Via G. La Masa 34, 20156 Milano, Italy;

^e Solid Liquid Interface Nano-Microscopy and Spectroscopy (SoLINano- Σ) lab, Department of Physics, Politecnico di Milano, Piazza Leonardo da Vinci 32, 20133 Milano, Italy.

* Corresponding author, andrea.macrelli@polimi.it

Abstract

1
2
3 Aqueous Zn-ion batteries (AZIBs) represent a safe and sustainable technology among the post-
4
5 lithium systems, though the poor understanding of the material behaviour at the cathode prevents
6
7 the full development of efficient AZIBs. ZnMn_2O_4 (ZMO) has been considered one of the cathode
8
9 candidates owing to its analogy to the well-established LiMn_2O_4 cathode for lithium-ion batteries,
10
11 however its electrochemical mechanism in the presence of aqueous Zn^{2+} Zn ions in aqueous
12
13 environment is unclear and still debated. In this work, we synthesised nanostructured ZMO thin
14
15 films by Pulsed Laser Deposition (PLD) and we evaluated, through extensive characterization by
16
17 microscopic, spectroscopic, and diffraction techniques, how the deposition and annealing conditions
18
19 affect the film properties. The self-supported nature and the high degree of control down to the
20
21 nanoscale make a thin film an ideal model system to study the electrochemistry of the material in
22
23 aqueous solution and to emphasize the impact of the film properties on its electrochemical response.
24
25 We highlighted the crucial role of the oxygen pressure in the modulation of the film porosity and
26
27 the combined effect of deposition pressure and annealing temperature to produce a film with
28
29 tailored properties in terms of morphology, crystallinity, and Zn stoichiometry. The self-supported
30
31 nature and the high degree of control down to the nanoscale make a thin film an ideal model system
32
33 to study the electrochemistry of the material in aqueous solution and to emphasize the impact of the
34
35 film properties on its electrochemical response. A complex redox mechanism involving multiple
36
37 concurrent reactions and the formation of zinc hydroxide sulphate hydrate (ZHS) was reported, as
38
39 well as the influence of the film porosity on the voltametric behaviour of the film at higher scan
40
41 rate. Our results confirm the intricate electrochemical mechanism of the ZMO material, which does
42
43 not merely involve the Zn^{2+} insertion/extraction but also the crucial participation of Mn^{2+} from the
44
45 electrolyte, and pave the way for the nanoscale design of engineered ZMO-based electrodes.
46
47
48
49
50
51
52
53
54
55
56
57
58
59
60
61
62
63
64
65

Keywords

Pulsed laser deposition, zinc-ion batteries, nanostructured cathode materials, ZnMn₂O₄ thin films.

1. Introduction

Rechargeable aqueous zinc-ion batteries (AZIBs) operating with a slightly acidic aqueous electrolyte and exploiting divalent Zn²⁺ Zn ions as charge carriers are a promising class of post-lithium next-generation batteries [1–3]. This type of secondary battery represents the evolution of primary alkaline zinc-ion batteries [4] and may be competitive against traditional lithium-ion batteries (LIBs) [5,6]. Indeed, zinc metal – notwithstanding shape-change and passivation issues that still have to be definitely sorted out [7–10] – can be effectively implemented as the anode and safely coupled with an aqueous medium, while lithium metal exhibits worse instability issues, combined with pyrophoricity [11]. Zinc metal is highly desirable due to its high theoretical gravimetric and volumetric specific capacities (820 mAh g⁻¹ and 5850 mAh cm⁻³, respectively), a redox potential of –0.76 V vs. SHE, and it can be produced and recycled using established processes [5]. Concerning the electrolyte, an aqueous medium is intrinsically safer and exhibits superior ionic conductivity compared to the flammable organic liquids traditionally employed in the state-of-the-art LIBs [1,5]. ~~The energy density provided by ZIBs is lower compared to LIBs, therefore they may represent a safe and cost-effective alternative to LIBs for stationary applications [10].~~

Nevertheless, the bottleneck to the development of efficient rechargeable AZIBs is the cathode. A few material candidates are available to reversibly sustain several electrochemical cycles involving a divalent cation, which is also responsible for the sluggish cathodic kinetics and early capacity fade [5,12–14]. In addition, the electrochemical mechanism is rather complex and encompasses multiple steps that may result in irreversible phase changes [1]. Among the proposed materials, manganese oxides [15–21], vanadium oxides [21,22], vanadium phosphates [1,23], metal vanadates [1,23],

1 Prussian blue analogues (PBAs) [24], and some organic redox-active compounds [25,26] have been
2 considered. Manganese oxides are particularly interesting, thanks to the abundant and low-toxicity
3 nature of Mn, which is available in various oxidation states (from +2 to +7) leading to several oxide
4 phases and structures [1]. In previous works, MnO [27,28], Mn₃O₄ [29–32], Mn₂O₃ [33–35],
5 amorphous MnO_x [36,37], and MnO₂ polymorphs (α [38,39], β [18,40], γ [16,19], δ [41,42], ϵ [43],
6 λ [44], and todorokite [45]) were tested as potential cathode materials for AZIBs. Another
7 alternative is zinc manganite, indicated by the general formula Zn_xMn_{3-x}O₄ [46–48], whose main
8 representative is ZnMn₂O₄ (ZMO), also known as hetaerolite. Zinc manganites are a family of
9 normal spinel oxides in which the cooperative Jahn-Teller distorted Mn³⁺ cations lead to a
10 tetragonal distortion of the overall crystal (which belongs to the *I*₄₁/*amd* space group) [47–49]. The
11 ideal spinel framework of ZMO, bearing a theoretical specific capacity of 224 mAh g⁻¹ [50], is
12 reported to be unsuitable for the reversible insertion/extraction of ~~zinc~~ Zn ions [51,52]; however,
13 proper nanostructuring, doping, introduction of stoichiometric defects, compositing with other
14 materials, and exploitation of reaction mechanisms different from mere Zn²⁺ insertion/extraction
15 may make this material an interesting candidate for AZIBs [53]. For example, N. Zhang *et al.*
16 fabricated non-stoichiometric ZnMn₂O₄, in which the presence of abundant Mn vacancies promoted
17 the Zn²⁺-ion insertion, thanks to a lower electrostatic repulsion between the host cations and the
18 divalent charge carriers [51]. ~~A nanostructured Mn-deficient ZMO cathode was also employed by~~
19 ~~Islam *et al.* to build an oriented nanoarchitecture [52].~~ In a similar approach, H. Zhang *et al.*
20 introduced oxygen defects to tailor the electronic conductivity, the ion diffusion kinetics, and the
21 energy barrier for ion mobility [54], while Lee *et al.* prepared Zn-rich manganite microspheres, with
22 nominal stoichiometry Zn_{1.67}Mn_{1.33}O₄ [55]. Interestingly, Wu *et al.* used a low-temperature
23 synthesis to prevent the structural water from being removed from the lattice, which had a
24 beneficial effect on the Zn²⁺ insertion and interfacial resistance [56]. Nanostructuring and
25 compositing with various types of conductive carbon nanostructures are other effective approaches
26 to improve the electrochemical performances and the structural stability of ZMO. ~~hollow ZMO~~

1
2
3
4
5
6
7
8
9
10
11
12
13
14
15
16
17
18
19
20
21
22
23
24
25
26
27
28
29
30
31
32
33
34
35
36
37
38
39
40
41
42
43
44
45
46
47
48
49
50
51
52
53
54
55
56
57
58
59
60
61
62
63
64
65

~~[56,57], graphene-ZMO nanocomposites [58,59], and carbon-supported ZMO nanostructures [60-63] showed improved capacity and durability, compared to bulk spinel ZMO. In addition, elemental doping can provide enhanced electrochemical activity and superior structural stability. [57-65], as well as elemental doping.~~ For example, Baby *et al.* reported the improved performances of cobalt Co-substituted ZMO (ZnMnCoO_4 , ZMCO) [50], Tao *et al.* highlighted the positive effect of Ni and Co co-substitution to suppress the Jahn-Teller distortion [66], Cai *et al.* investigated the impact of Al^{3+} substitution in Zn^{2+} sites [67], and Shao *et al.* controlled the formation of oxygen defects in the ZMO lattice by double-doping with K and Fe [68]. Finally, synergistic electrochemical effects and better stability could be achieved by compositing ZMO with Mn_2O_3 [69-71] or Ti-MXenes [72]. In general, ZMO can be regarded as the Zn-analogue of LiMn_2O_4 and suffers from the same drawbacks as manganese oxides cathodes, i.e., poor electronic conductivity, structural instability, poor rate performance, irreversible phase transformations, and Mn dissolution during cycles [1,5,64]. In addition, the electrochemical mechanism of ZMO-based materials in the presence of a Zn^{2+} - and Mn^{2+} -containing electrolyte is still unclear, and several mechanisms have been reported to occur and/or to coexist, such as: Zn^{2+} ions insertion/extraction [51,64], H^+ insertion/extraction [54,62], $\text{Zn}^{2+}/\text{H}^+$ co-insertion accompanied by the formation of zinc hydroxide sulphate hydrate (ZHS) [56,65,73,74], and reversible deposition/dissolution of MnO_x from the electrolyte [75].

Herein, we report on the synthesis of ZMO thin films by Pulsed Laser Deposition (PLD), a technique that, to the best of our knowledge, has never been employed to grow ZMO-based materials. A thin film can be used as a model system to study the electrochemical behaviour of the pure material; indeed, a film offers unique advantages for materials-science investigations, including: improved diffusion kinetics for ions and electrons, possibility to investigate novel materials and structures, and self-supported nature, deriving from the absence of polymeric binders and conductive additives [76]. In addition, beyond fundamental studies, thin films electrodes can be

1 directly implemented in real-life thin-film microbatteries [77,78]. PLD is a highly versatile physical
2 technique that allows the deposition of practically any material and the growth of nanostructured
3 thin films whose properties can be easily tuned in terms of morphology, porosity, stoichiometry,
4 structure, crystallinity, and phase by controlling a few deposition parameters [79,80]. In this work,
5 ZMO thin films fabricated by PLD are fully characterized in terms of compositional, structural, and
6 optical properties, and then employed in half-cells to assess their electrochemical behaviour and
7 material modifications. Based on the approach previously developed in [81], electrochemical
8 measurements on ZMO thin films in aqueous electrolyte are complemented by SEM and Raman
9 studies.

2. Experimental

2.1. Synthesis of thin films

10 ZMO thin films were synthesized by PLD in a stainless-steel vacuum chamber, equipped with a
11 primary scroll pump and a turbomolecular pump, connected in series, able to evacuate the chamber
12 down to a base pressure of $1-4 \times 10^{-3}$ Pa. Ablation was performed at room temperature using a
13 frequency-doubled Nd:YAG laser source, in particular the 532 nm second harmonic, with 5–7 ns
14 laser pulses and a repetition rate of 10 Hz. The laser pulses struck the target at an incidence angle of
15 45° and with an elliptical spot whose size was fixed at $\sim 6 \text{ mm}^2$ by properly focusing the laser
16 pulses. The resulting laser fluence on the target was varied in the range $2-6 \text{ J cm}^{-2}$ by adjusting the
17 pulse energy. The target was a $\text{Mn}_2\text{O}_3:\text{ZnO}$ (1:1 mol%) vacuum hot-pressed pellet (99.99%,
18 Testbourne B.V.), mounted on a support able to rotate and translate during deposition to ensure a
19 uniform ablation. The chamber was also equipped with a quartz crystal microbalance (QCM) to
20 estimate the deposited mass and consequently the film density. Depositions were carried out both in
21 vacuum and in O_2 gas (Sapio, 5.0 purity), whose pressure was tuned by mass flow controllers at 1,
22
23
24
25
26
27
28
29
30
31
32
33
34
35
36
37
38
39
40
41
42
43
44
45
46
47
48
49
50
51
52
53
54
55
56
57
58
59
60
61
62
63
64
65

1
2
3
4
5
6
7
8
9
10
11
12
13
14
15
16
17
18
19
20
21
22
23
24
25
26
27
28
29
30
31
32
33
34
35
36
37
38
39
40
41
42
43
44
45
46
47
48
49
50
51
52
53
54
55
56
57
58
59
60
61
62
63
64
65

10, 30, 50, 70, 100, and 150 Pa. The substrate was placed on a rotating holder at constant distance from the target of 5 cm. Silicon <100> (Siegert Wafer), soda-lime glass slides (Marienfeld), and F-doped SnO₂ (FTO)-coated soda-lime glass slides (Sigma-Aldrich) were used as the substrates.

Glass-based substrates were cleaned with isopropyl alcohol in ultrasonic bath before the insertion into the PLD chamber and dried with compressed air. The deposition time was selected according to the deposition rate and depending on the expected film thickness. Some samples were annealed in air using a Lenton Muffle furnace (ECF type) at different temperatures (400–800 °C).

2.2. Characterization

A field emission scanning electron microscope (FE-SEM, Zeiss SUPRA 40) was used to acquire top view and cross-sectional morphological images of thin films deposited on Si and FTO-coated glass. The film composition was evaluated by energy-dispersive X-ray spectroscopy (EDXS) using a Peltier-cooled silicon drift detector (SDD) within the SEM microscope (Oxford Instruments) and elaborated using the AZtec EDS software. Raman spectroscopy was used to gain information about the structure and the crystallinity of the films. A Renishaw InVia micro-Raman spectrometer equipped with a diode-pumped solid-state laser emitting 532 nm excitation radiation was used. The laser was focused on the sample using a 50× objective and the laser power was selected so as to avoid any photo-induced damage to the sample (typical values were 0.7–1.75 mW). For the quasi-*in situ* Raman characterization after the electrochemical measurements, a Confotec NR500 spectrometer by Sol instruments was used, equipped with a solid-state laser ($\lambda=532$ nm, laser power on sample ~0.6 mW) and a 40× objective. X-ray diffraction (XRD) was employed to investigate the crystalline structure of the films. A HRD3000 diffractometer (Ital Structures, Riva del Garda, Italy) operating with monochromated Cu K α radiation ($\lambda=0.1541$ nm) and equipped with a curved position-sensitive multichannel gas-filled detector (2θ range 0–120°, resolution 0.029°, Inel CPS-120) was used. The XRD measurements were carried out in grazing incidence configuration (GIXRD) with an incidence angle of $\omega=2^\circ$. The optical properties of films deposited on soda-lime

1 and FTO-coated glass were probed by direct transmittance in the range 190–1100 nm using a
2 Shimadzu UV-1800 spectrophotometer, and by transmittance and reflectance in the range 250–2000
3
4 nm using a PerkinElmer Lambda 1050 spectrophotometer equipped with a 150 mm-integrating
5
6 sphere.
7

8 9 10 *2.3. Electrochemical characterization*

11
12 The electrochemical behaviour of as-deposited and annealed ZMO films on conductive FTO-coated
13
14 glass slides was investigated in a three-electrode configuration and using a home-made
15
16 electrochemical cell. Briefly, the sample was placed on top of a stainless-steel support and
17
18 electrically insulated by a polymeric gel. Electrical contacts were made by attaching a Cu wire to
19
20 the exposed FTO layer with Cu tape. A PTFE case equipped with a VITON O-ring was directly
21
22 pressed on the sample and fixed by screws to the support, then it was filled with the liquid
23
24 electrolyte (total volume ~1 mL). The area of the film exposed to the electrolyte was ~0.4 cm². Two
25
26 platinum wires were inserted into the cell, one turning around the whole cell and operating as the
27
28 counter electrode, and one acting as a quasi-reference (Pt-QRef) electrode. The potential shift of the
29
30 Pt-QRef electrode with respect to the Ag/AgCl (KCl 3.5 M) reference electrode was experimentally
31
32 determined in a two-electrode cell to be +0.445 V, with stability within a few mV in the
33
34 investigated electrolytes. All potentials reported have been referenced to the Ag/AgCl scale. ZMO
35
36 samples were tested in aqueous electrolytes containing 2 M ZnSO₄ (ZS), 0.1 M MnSO₄ (MS), or 2
37
38 M ZnSO₄ + 0.1 M MnSO₄ (ZMS), prepared in deionized water from zinc sulphate heptahydrate
39
40 (ZnSO₄ · 7H₂O, ≥ 99.0%) and manganese sulphate monohydrate (MnSO₄ · H₂O, ≥ 98%), both
41
42 purchased from Sigma-Aldrich. Cyclic voltammetry (CV) and other electrochemical measurements
43
44 were was performed using a PalmSens4 potentiostat/galvanostat/impedance analyser.
45
46
47
48
49
50
51
52
53
54
55
56
57
58
59
60
61
62
63
64
65

3. Results and discussion

3.1. Optimization of PLD parameters

PLD allows one to easily adjust the deposition parameters, especially the chamber pressure, the type of gas, the laser fluence, and the target-substrate distance, in order to fabricate a thin film with tuneable and optimizable properties and performances. ZMO thin films were grown in vacuum and at different O₂ pressures (1–150 Pa); the gas atmosphere affects the dynamics of plasma formation, cluster nucleation, and deposition [80], thus it mainly affects the resulting film morphology. SEM cross-sectional images of as-deposited ZMO films on Si as a function of the O₂ deposition pressure (laser fluence $\sim 3.7 \text{ J cm}^{-2}$, deposition time = 15 min) are reported in Fig. 1a. Increasing the O₂ pressure from vacuum to 150 Pa, the film morphology changes from a compact columnar structure to a highly porous tree-like structure, along with a progressive increase of film porosity and surface roughness. At high oxygen pressures (100 and 150 Pa), the dense columnar structure is replaced by porous nanotrees. The increase of film porosity is accompanied by a sharp decrease in density (below $\sim 1 \text{ g cm}^{-3}$ for samples deposited at or above 50 Pa, as estimated from QCM measurements coupled with SEM images; for comparison, the density of bulk crystalline ZMO is 5.254 g cm^{-3} [82]) and by a corresponding increase in surface area and film thickness at fixed deposition time. The morphology evolution as a function of the background gas pressure described above is typical of PLD-grown oxides and nitrides thin films [80,83–87]. The laser fluence (i.e., the laser energy per unit area striking the target) has a less evident effect on film morphology. In addition to an expected increase of the deposition rate at constant O₂ pressure, higher fluences lead to more compact films and, especially at high O₂ pressures ($\geq 50 \text{ Pa}$), cause the detachment of the growing film from the substrate, the film breakup, and the presence of a larger number of defects (Fig. S1). As a result, a reasonable fluence of $\sim 3.7 \text{ J cm}^{-2}$, corresponding to energies of $\sim 225 \text{ mJ pulse}^{-1}$, was selected for subsequent depositions as a compromise between deposition rate and film quality. Typical deposition rates at this fluence range from some tens of nm min^{-1} in vacuum/low O₂ pressure up to

1 hundreds of nm min^{-1} above 50 Pa. O_2 background atmosphere also affects the film stoichiometry,
2 which can be modified with respect to the nominal composition of the target by depositing in a
3 reactive gas. As depicted in Fig. 1b, where EDX elemental analysis is reported, our as-deposited
4 films are enriched with oxygen as the O_2 deposition pressure increases up to ~ 30 Pa, with the O
5 atomic content in the films rising from 48% (vacuum) to $>60\%$ (30 Pa). This increase is
6
7 accompanied by a decrease in the Mn atomic content (from 38% to 27%), while the Zn atomic
8
9 content shows much less variability (between 11% and 14%) in the whole O_2 pressure range.
10
11
12
13
14
15
16

17 [Figure 1 about here]

18
19
20 Structural information about ZMO films was gained by Raman spectroscopy. Raman spectra of all
21 as-deposited films at any O_2 pressure and laser fluence show a weak and broad band centred around
22
23 600 cm^{-1} and extending in the range $450\text{--}750\text{ cm}^{-1}$, indicating an amorphous nature of the film (Fig.
24
25
26
27
28
29
30
31
32
33
34
35
36
37
38
39
40
41
42
43
44
45
46
47
48
49
50
51
52
53
54
55
56
57
58
59
60
61
62
63
64
65

[Figure 2 about here]

3.2. Thin films annealing

In order to promote the film crystallization, as-deposited ZMO films were subjected to thermal
treatments in air in the temperature range $400\text{--}800\text{ }^\circ\text{C}$. Film crystallization to the expected spinel
phase [46,49,88,89] was achieved at any temperature above $450\text{ }^\circ\text{C}$, as confirmed by the Raman
spectrum of the annealed film of Fig. 2a, where sharp peaks are observed. Three main peaks are
found at $325, 385, \text{ and } 679\text{ cm}^{-1}$ (the latter mode can be assigned to A_{1g} symmetry [49]), while
additional shoulders and weak features are observed also at $302, 373, 475, 587, \text{ and } 652\text{ cm}^{-1}$ (Fig.
S2), all well matching with the reported Raman bands of ZnMn_2O_4 [46,49]. No signals from
secondary phases were detected. In Fig. 2b, the EDX elemental analysis of ZMO films deposited at
different O_2 pressures and annealed in air at $600\text{ }^\circ\text{C}$ for 3h are reported. Although EDX suffers from
low accuracy in the quantification of light elements, which entails uncertainties in the absolute

1 values especially in the absence of calibration samples, the overall trends of the atomic contents
2 with respect to O₂ pressure are still relevant. After the thermal treatment, the atomic content of Zn
3 and Mn increases compared to as-deposited films, while the O atomic content decreases (at least for
4 samples deposited at ≥10 Pa O₂). None of the elements, however, matches the atomic percentages
5 of stoichiometric ZnMn₂O₄, indicated by grey dashed lines in Fig. 2b. All the films contain a lower
6 amount of oxygen (52–55%) with respect to the theoretical value of ~57%, and a higher amount of
7 Mn, which may indicate the presence of Mn ions with a lower oxidation state (i.e., Mn²⁺), and the
8 possible localized formation of spinel hausmannite Mn₃O₄, isostructural to ZnMn₂O₄ [49,90,91].
9
10
11
12
13
14
15
16
17
18
19

20 *[Figure 3 about here]*
21
22

23 SEM images of ZMO films after annealing are reported in Fig. 3a (cross-sections) and in Fig. S3
24 (top-views). The morphology is completely different from that of as-deposited films (Fig. 1a).
25 Films are polycrystalline, with morphological grains ranging from hundreds of nm to ~50 nm as the
26 O₂ deposition pressure increases. In addition, the columnar and compact structure of films deposited
27 in vacuum and 10 Pa is replaced by large faceted crystalline grains and by some voids and cavities
28 (Fig. 3a and Fig. S3a-c), qualitatively indicating a higher degree of porosity compared to as-
29 deposited films, also for low O₂ deposition pressures. For films deposited at 50 and 100 Pa, small
30 crystalline grains (50-100 nm) assemble into vertical structures resembling the original nanotrees.
31 The Raman spectra of annealed films deposited in vacuum and at 1, 10, 50, and 100 Pa of O₂ are
32 reported in Fig. 3b and were analysed using Lorentzian fittings. The three main Raman bands of
33 spinel ZMO (here labelled as peak I, II, and III, respectively) exhibit a blueshift as the deposition
34 pressure increases (Fig. 3c and Fig. S4a-b), which is more relevant for the high-frequency A_{1g} mode
35 (peak III) [49]. Indeed, peak III shifts from 673.8 cm⁻¹ to 680.3 cm⁻¹ as the O₂ deposition pressure
36 is increased from vacuum to 150 Pa. In addition, the intensity ratio between peak I and peak III is
37 reversed with increasing O₂ pressure: indeed, the A_{1g} peak (peak III) is the most intense in the
38 Raman spectra of crystalline samples deposited in vacuum and at 1 Pa, whereas peak I becomes
39
40
41
42
43
44
45
46
47
48
49
50
51
52
53
54
55
56
57
58
59
60
61
62
63
64
65

1 dominant at or above 10 Pa (Fig. 3c). Such variations in peak position and relative intensity may be
2 ascribed to the effect of crystallite size only [92], however similar trends are reported also by
3
4 Nádherný *et al.* [46] and correlated to the amount of Zn in the manganite structure, i.e., to the
5 stoichiometric x value in $Zn_xMn_{3-x}O_4$. Since the atomic contents of Mn and Zn in the films after
6
7 crystallization are not constant (Fig. 2b) and no secondary phases are detected by Raman
8
9 spectroscopy and SEM imaging, the modifications observed in the Raman spectra of Fig. 3b might
10
11 be attributed to slight changes in the relative contents of metallic elements in the overall manganite
12
13 structure. The differences observed in peak position and relative intensity ratios with increasing O_2
14
15 deposition pressure are not associated with a clear trend in peak width (Fig. S4c). Compared to the
16
17 Raman spectra of spinel Mn_3O_4 reported in [92], which correlates the progressive redshift and
18
19 broadening of the main A_{1g} peak with decreasing crystallite size from >100 nm to 7 nm, our spectra
20
21 exhibit a general blueshift and no specific peak broadening or narrowing as the O_2 pressure
22
23 increases. This may indicate that the crystal size does not play the major role in affecting the Raman
24
25 spectra of annealed ZMO thin films. In addition, annealing in air of selected samples at different
26
27 temperatures (500, 600, 700, and 800 °C) demonstrated that the Raman spectra are not affected by
28
29 the increase in temperature, even if the ZMO crystalline grains get bigger as the annealing
30
31 temperature increases (Fig. S5 and Fig. S6a). In this case, a gradual decrease of peaks width
32
33 confirms the improvement of crystalline quality with increasing annealing temperature (Fig. S6b).
34
35 Film crystallization is further confirmed by GIXRD measurements. The X-ray diffraction patterns
36
37 of ZMO films produced in vacuum and at 1, 10, 50, and 100 Pa of O_2 are reported in Fig. 4, along
38
39 with the powder reference pattern of tetragonal spinel hetaerolite $ZnMn_2O_4$ (Card No: 6990,
40
41 WWW-MINCRYST [93,94]). Good agreement with the reference pattern is observed for ZMO
42
43 films produced at 50 and 100 Pa, which exhibit the most intense (211) reflection at $2\theta \sim 36.40^\circ$ and
44
45 consistent intensity ratios. The X-ray data at 10 Pa are coherent as well, even though the (103)
46
47 reflection is absent and some discrepancies affect the relative intensity ratios, especially the (112)
48
49 vs. (200) and the (321) vs. (224). In contrast, the main reflection in the GIXRD pattern of the ZMO
50
51
52
53
54
55
56
57
58
59
60
61
62
63
64
65

1 film produced at 1 Pa is the (103) at $2\theta \sim 32.67^\circ$, and the (200), (220) and (400) reflections are weak
2 or totally suppressed. Finally, the X-ray diffraction pattern of the ZMO sample produced in vacuum
3 exhibits one sharp and narrow peak at $2\theta \sim 17.87^\circ$, corresponding to the (101) reflection, while most
4 of other reflections are suppressed, except for the (312), (224), and (400). The XRD results reveal a
5 different preferential crystalline orientation within ZMO films produced in vacuum and at 1 Pa O₂
6 and suggest that the O₂ deposition pressure affects not only the short-range order of the material (as
7 confirmed by the modifications in the Raman spectra, Fig. 3b-c), but also the long-range crystalline
8 texture.

9
10
11
12
13
14
15
16
17
18
19
20
21
22
23
24
25
26
27
28
29
30
31
32
33
34
35
36
37
38
39
40
41
42
43
44
45
46
47
48
49
50
51
52
53
54
55
56
57
58
59
60
61
62
63
64
65

[Figure 4 about here]

Quantitative analysis was carried out using the Williamson-Hall (WH) method [95,96], which allows the estimation of the average size of crystal domains and of the lattice micro-strain through the broadening of the XRD peaks (Fig. S7a-e). As expected, the domain size is maximum in the ZMO film produced in vacuum ($\tau \sim 63$ nm) and it decreases down to $\tau \sim 57$ nm and $\tau \sim 27$ nm for films deposited at 1 and 10 Pa, respectively; it remains almost constant in the film produced at 50 Pa ($\tau \sim 29$ nm), but it raises to $\tau \sim 38$ nm at 100 Pa (Fig. S7f). The lattice micro-strain is found to be positive in all the films, i.e., indicating the presence of a tensile stress state, and it is maximum in the film deposited at 1 Pa (Fig. S7f). Raman spectroscopy and GIXRD results clearly indicate that the O₂ deposition pressure is a key parameter affecting the structural ordering of the ZMO thin films at both the short/medium range and the long range. In particular, GIXRD measurements highlighted the evolution of the preferential crystal orientation, the variation of the crystal size, and the occurrence of lattice micro-strains, while the modifications of the Raman spectra may be correlated to the Zn stoichiometry according to [46]. However, additional effects may contribute to the overall shift and broadening of the ZMO Raman peaks, e.g., the residual stress state, the presence of traces of secondary phases, the oxygen deficiency, and the crystal size, therefore the trends observed in Fig. 3b-c and Fig. S4 may result from multiple and interrelated causes.

3.3. Optical properties of annealed films

ZMO thin films were deposited on glass and FTO-coated glass slides, with the purpose of carrying out optical measurements. The deposition time, at any value of O₂ pressure and constant fluence of 3.7 J cm⁻², was adjusted to achieve a film thickness in the range 500–600 nm, depending on the deposition rate previously evaluated on samples deposited on Si in similar conditions. Before annealing, ZMO thin films exhibit a dark reddish colour, which turns orange/yellow after thermal treatment in air (Fig. S8a). Since the thermal stability of the glass support is limited to ~550 °C, annealing of ZMO films on bare glass and FTO-coated glass was performed at 500 °C for 2h. This temperature allows good film crystallization, as evaluated by Raman spectroscopy and SEM analysis (Fig. S8b-c). In Fig. 5, UV-Vis transmittance, reflectance, and absorption curves in the wavelength range 300–2000 nm for ZMO samples deposited on soda-lime glass at 1, 10, 50, and 100 Pa of O₂, and crystallized in air at 500 °C for 2h, are reported. Transmittance and reflectance data of Fig. 5a-b were collected in a spectrophotometer equipped with the integrating sphere and account for both direct and diffuse contributions. Absorption data are estimated by the relation:

$$A(\lambda, \%) \cong 100 - T(\lambda, \%) - R(\lambda, \%)$$

Transmittance and absorption curves (Fig. 5a and Fig. 5c) exhibit a small blueshift as the deposition pressure increases. In addition, the number of interference fringes in the transmittance curves decreases with increasing O₂ pressure as well. Similarly, the increase of surface roughness leads to less defined fringes as the O₂ pressure increases. Absorption curves of Fig. 5c feature extended sub-bandgap optical absorption in the range 600–750 nm, which may indicate the presence of defect states in the mid-gap region of the material [89]. In Fig. 5d, absorption curves are reported as a function of photon energy, in the range 0.5–4.5 eV, for comparison.

[Figure 5 about here]

1
2 Similar results are obtained by measuring the direct transmittance of ZMO films deposited on FTO-
3 coated glass at the same deposition conditions in terms of laser fluence and O₂ pressure as on the
4 bare glass slides (Fig. S9), with average thickness ~500–600 nm. The slight blueshift of the
5 transmittance curves observed in Fig. 5a as the O₂ pressure increases is still present, even if some
6 deviations are observed, e.g., for the film deposited at 50 Pa. Such variations may be ascribed to the
7 effect of the substrate on film morphology or, more likely, to the contribution of the diffuse
8 transmittance, which is lost during measurements of direct transmittance and could be relevant for
9 porous samples.
10
11
12
13
14
15
16
17
18
19
20
21
22

23 3.4. Electrochemical properties of annealed films

24
25
26 The schematic illustration for the preparation of crystalline ZMO thin films on an FTO-coated glass
27 substrate for electrochemical characterization is reported in Fig. 6. All the films were grown by
28 PLD in O₂ atmosphere with tuneable morphology and average thickness in the range 500–600 nm,
29 and then they were thermally annealed in air at 500 °C for 2h to achieve the proper spinel phase
30 without damaging the glass substrate.
31
32
33
34
35
36
37
38

39 [Figure 6 about here]

40
41
42 The CV profiles of the ZMO thin film grown at 50 Pa of O₂ on FTO-coated glass substrate and
43 crystallized in air at 500 °C for 2h (thickness ~500–600 nm) are reported in Fig. 6 Fig. 7. CV was
44 performed in ZMS electrolyte at a scan rate of 1 mV s⁻¹. We have selected this electrolyte because
45 it is the standard for AZIB studies: it is worth noting that differences in composition among MS,
46 ZS, and ZMS electrolytes have a specific impact on the structural evolution upon cycling of MnO_x-
47 based electrodes [81]. CV cycling was carried out in a potential range spanning Mn reactivity
48 between reduction to Mn²⁺ and oxidation to Mn⁴⁺. The complex voltammetric patterns,
49 corresponding to combined Mn-redox and phase-transformation/film-formation, can be interpreted
50
51
52
53
54
55
56
57
58
59
60
61
62
63
64
65

1 in the methodological framework set in [81]. Cycling was started from 0.1 V with an anodic-going
2 scan, that exhibits a weak anodic peak at ~0.8 V and a current onset at ~0.9 V. These processes, in
3 principle, can correspond to phase formation by oxidation of Mn^{2+} present in the electrolyte and
4 oxidation of Mn^{3+} present in ZMO, converting to a Mn^{4+} -containing phase. The first cycle is
5 markedly different from the following ones, indicating an activation/transformation process of the
6 film, which is frequently reported for Mn- and ZMO-based electrode materials [59,63]. In the
7 anodic branch, starting from the second cycle, the two features observed in the first anodic-going
8 scan are notably activated by the reduction processes observed in the cathodic-going scan –
9 discussed below – and develop into a couple of oxidation peaks. These peaks are initially centred at
10 0.75 V and 0.86 V and exhibit a progressive shape change and the tendency to shift towards higher
11 potential values, as the number of cycles increases. These modifications of the anodic CV features
12 can be ascribed to a progressive phase transformation, as detailed below. As far as the cathodic
13 branch is concerned, a couple of reduction peaks can be observed, that exhibits a notable change
14 between the first and the subsequent cycles. Similarly to the anodic counterpart, prolonged cycling
15 leads to progressive peak shift in the anodic direction in the ranges 0.34–0.4 V and 0.49–0.55 V,
16 respectively. Our CV curves agree with those reported in previous works and corresponding to
17 various ZMO-based nanostructures in the same electrolyte solution [60,69,75]. The assignment of
18 the redox peaks to a specific electrochemical process is not unique since multiple concurrent
19 processes may occur at the electrode-electrolyte interface, yielding very similar current responses,
20 and the scientific literature is not unanimous. During the anodic scan, the oxidation peaks could be
21 ascribed to both the extraction of Zn^{2+} cations from the host lattice, accompanied by the stepwise
22 oxidation of Mn^{3+} to Mn^{4+} , and to the electrodeposition of MnO_x interphases from Mn^{2+} species
23 present in the electrolyte, either because of its formulation or originating from the cathodic
24 dissolution of the film material. During the cathodic scan, these processes are reversed. Overall,
25 cycling seems to lead to a stable voltammetric pattern, featuring a couple of reversible redox
26 processes involving a solid electrode/electrolyte interface.

[Figure 7 about here]

1
2
3 In order to gain better insight into the nature of these electrochemical material transformations, we
4
5 resorted to *ex situ* structural and morphological characterization. After having completed the CV
6
7 cycling experiments of Fig. 6 Fig. 7, the aged ZMO sample was extracted from the cell,
8
9 immediately rinsed in deionized water, and gently dried to remove any trace of soluble sulphates. In
10
11
12 Fig. 7a Fig. 8a, a SEM cross-sectional image of the aged film at the end of the sixth cycle is
13
14 depicted, revealing a profound modification with respect to the morphology of the pristine film (not
15
16 shown, but reasonably comparable with the cross-section of Fig.3a). Specifically, a clear multi-
17
18 layered structure develops from the initial columnar and granular morphology: starting from the
19
20 bottom part of the image, the first layer resembles the structure of the original film, even if its
21
22 thickness is reduced (to ~300 nm) and the morphology is slightly changed (Fig. 7b Fig. 8b),
23
24 denoting some degree of electrochemical activity. The second layer (thickness ~800–900 nm)
25
26 consists of a porous, thick deposit, which can be identified by Raman spectroscopy (Fig. 7e Fig. 8c)
27
28 as MnO_x [97], originating either from the electrodeposition of Mn²⁺ in the electrolyte, or from the
29
30 transformation of the ZMO film. Finally, the third layer is constituted by thin, water-insoluble
31
32 flakes. This peculiar flake-like morphology (Fig. 7a Fig. 8a and Fig. S10a) suggests the
33
34 precipitation of zinc hydroxide sulphate hydrate (ZHS) Zn₄(OH)₆(SO₄)·nH₂O phase, commonly
35
36 reported in previous works as a by-product formed during the discharge of AZIBs in near-neutral
37
38 aqueous electrolytes containing Zn sulphate [60,62,75,98]. The formation of ZHS is conventionally
39
40 associated with proton insertion into the active film during the cathodic scan, leading to an increase
41
42 of the pH of the electrolyte surrounding the film, and to the precipitation of this basic compound
43
44 that acts as a buffer [98]. The presence of ZHS is confirmed by both Raman spectroscopy, i.e., the
45
46 peaks at 969 and 1015 cm⁻¹ [98] (Fig. 7e Fig. 8c), and EDXS, which reveals the occurrence of
47
48 sulphur in addition to Zn, Mn, and O (Fig. S10b).
49
50
51
52
53
54
55
56
57
58

[Figure 8 about here]

1 To highlight the effect of the film morphology on the electrochemical response of the material,
2 additional CV measurements in ZMS electrolyte were carried out at a higher scan rate of 25 mV s^{-1}
3
4 – de-emphasizing diffusion-controlled processes with respect to phase-formation ones – on ZMO
5
6 films grown at 1, 50, and 100 Pa of O_2 , corresponding to increasing porosity. The CV profiles are
7
8 reported in ~~Fig. 8~~ Fig. 9, displaying the first eight cycles for each sample. It can be noticed that the
9
10 shape of the CV curves differs significantly across the samples. Moreover, for a given sample, the
11
12 CV responses at 1 and 25 mV s^{-1} are different (e.g., compare ~~Fig. 6~~ Fig. 7 and ~~Fig. 8b~~ Fig. 9b).
13
14
15 Firstly, the redox peaks become more defined as the film porosity increases, i.e., moving from 1 to
16
17 100 Pa. This is an indication of a diffusion-based process, which is facilitated both at lower scan
18
19 rate and in samples exhibiting shorter diffusion paths. Secondly, all the curves show a progressive
20
21 separation of the peaks towards higher potentials (in absolute value) as the cycles proceed. This
22
23 effect, that was less evident at 1 mV s^{-1} , owing to the lower currents involved, is due to the
24
25 formation of a resistive layer during the electrochemical cycling, leading to increased polarization.
26
27 This phenomenon is progressively less evident as the porosity increases, especially in the case of
28
29 the most porous film (~~Fig. 8c~~ Fig. 9c), the electrochemical response of which features sharper redox
30
31 peaks and stabler cycle shapes compared to those of the less porous ones (~~Fig. 8a-b~~ Fig. 9a-b).
32
33
34
35
36
37
38
39

40 [Figure 9 about here]

41
42 After the CV test, the sample grown at 100 Pa of O_2 – which showed sharper and stabler redox
43
44 peaks in the CV of Fig. 9c – was subjected to a series of constant potential measurements in ZMS
45
46 electrolyte to promote the redox reactions and to evaluate the current response over time. At the
47
48 same time, quasi-*in situ* Raman measurements were carried out to probe the sample structural
49
50 evolution. The Raman results and the current vs. time profiles at selected potential values are
51
52 summarized in Fig. 10 and Fig. S11, respectively. After the CV (curve b) the main ZMO features
53
54 are still visible, however a broad band arises next to the A_{1g} peak and extends between 550 and 650
55
56 cm^{-1} . In addition, a broad peak starts to be visible at $\sim 490 \text{ cm}^{-1}$. Both features indicate the
57
58
59
60
61
62
63
64
65

1 formation of MnO_x during the CV cycles [64,97]. Cathodic polarization at 0.45 V for 1100 s
2 partially restores the film to its initial conditions (curve c), reducing the intensity of the MnO_x
3 bands: this behaviour is compatible with the incomplete dissolution of the MnO_x layer, which can
4 also be accompanied by Zn^{2+} insertion in the MnO_x formed during the anodic branches of the CV
5 run either from ZMO de-insertion or from oxidative electrodeposition of Mn^{2+} present in solution.
6 Correspondingly, the cathodic current asymptotically approaches zero after 1100 s (Fig. S11a). The
7 following anodic polarization at 1.05 V for 1800 s leads to a significant decrease in the intensity of
8 ZMO Raman peaks, in conjunction with the uprise of the MnO_x band (curve d), which can be
9 explained with both Zn^{2+} de-insertion from ZMO and electrodeposition from the electrolyte.
10 Moreover, the resultant anodic current profile does not approach zero, but tends asymptotically to a
11 current value of $\sim 260 \mu\text{A}$ (Fig. S11b), suggesting an ongoing redox process. Finally, the Raman
12 peaks of ZMO become clearly visible again after the second cathodic polarization at 0.45 V for
13 1500 s, even if the MnO_x features are still intense (curve e). The corresponding cathodic current
14 profile approaches zero at the end of the measurement (Fig. S11c), indicating that the MnO_x phase
15 cannot be totally and reversibly reduced at 0.45 V. In addition, as reported in the inset of Fig. 10,
16 the peaks at 960 and 1008 cm^{-1} appear after the second cathodic polarization, revealing the
17 precipitation of the ZHS phase [98]. Interestingly, ZHS was not present immediately after the CV at
18 25 mV s^{-1} (as it was in the case of CVs at 1 mV s^{-1} , see Fig. 8) since its formation evidently
19 requires longer reaction times. The typical flake-like morphology of ZHS was also highlighted by
20 SEM (Fig. S11e-g). Interestingly, in the absence of electroactive Mn^{2+} in the electrolyte – i.e., using
21 the ZS electrolyte – the Raman spectrum does not appreciably change upon anodic polarization at
22 1.05 V (compare curves e and f) and the current vs. time profile differs significantly from that
23 observed when the same process is run in the ZMS electrolyte (compare Fig. S11b and Fig. S11d),
24 exhibiting no asymptotic current value and a rapid decrease to zero (the measurement was stopped
25 after 500 s). Notably, the high-frequency Raman peaks do not disappear, indicating no ZHS
26 dissolution at this potential value. This last test in the ZS electrolyte confirms that the main redox

1 process in the potential ranges investigated in this work involves the electrodeposition of MnO_x
2 species from Mn^{2+} dissolved in the electrolyte, possibly accompanied by the reversible
3
4 insertion/extraction of Zn^{2+} in these electrodeposited layers.
5
6

7
8 [Figure 10 about here]
9

10
11 Lastly, in order to better distinguish between phase transformation and formation processes, CV
12 measurements at 25 mV s^{-1} were performed also on bare FTO-coated glass substrates in the MS,
13 ZS, and ZMS electrolytes, as reported in ~~Fig. S11~~ Fig. S12. No electrochemical activity is
14
15 obviously reported in ZS electrolyte, due to the absence of redox-active species in the selected
16 potential range. On the other hand, redox peaks are observed in both MS and ZMS electrolytes,
17
18 which could be ascribed to the electrodeposition/dissolution of MnO_x on the surface from the Mn^{2+}
19
20 eations in the electrolyte. The noticeable difference in CV shape and intensity denotes the role of
21
22 Zn^{2+} eations in the electrochemical reactions, which may insert/de-insert into/from the
23
24 electrodeposited MnO_x layer only in ZMS electrolyte. Our results are closely similar to those
25
26 reported by Soundharrajan *et al.*, which unravelled the dominant role of Mn^{2+} eations in the
27
28 electrolyte on the electrochemical mechanism of ZnMn_2O_4 -based materials [75], and to those of
29
30 [81], which highlights the impact on the electrochemical response of MnO_x resulting from the
31
32 presence of Zn^{2+} in the electrolyte.
33
34
35
36
37
38
39
40
41
42
43
44
45

46 4. Conclusions

47
48 In this work, we successfully synthesized ZMO thin films via PLD on different substrates. Using
49
50 complementary characterization techniques, including SEM, EDXS, Raman spectroscopy, XRD,
51
52 UV-Vis optical spectroscopy, we highlighted the effect of deposition (O_2 pressure, laser fluence)
53
54 and annealing (temperature, duration) parameters on the variation of film morphology, composition,
55
56 and crystallinity, which strongly affect the vibrational, structural, optical, and electrochemical
57
58
59
60
61
62
63
64
65

1 properties of the material. The O₂ deposition pressure results to be the most significant synthesis
2 parameter: by increasing the O₂ pressure from vacuum to 150 Pa, the ZMO film becomes more
3 porous and less dense and, after crystallization upon thermal treatment in air, the effect of
4 deposition pressure is still observable in the Raman features, the XRD crystal orientation, the
5 stoichiometry, and the optical absorption of the film. Since bulk ZMO was previously reported to
6 exhibit poor electrochemical activity in the presence of Zn²⁺ [51], a rationally designed ZMO
7 material in terms of nano-porosity (and hence density and surface area), crystal size and orientation,
8 phase purity, and Zn vs. Mn stoichiometry is supposed to demonstrate superior electrochemical
9 properties, resulting in improved performances when implemented in a real device. The CV tests
10 carried out on the crystallized films showed an electrochemical response consistent with current
11 knowledge of the electrochemistry of MnO_x-based materials, and emphasized a major impact of the
12 film synthesis conditions. In conjunction with *ex situ* characterization measurements on aged
13 samples and following the approach developed in [81], such CV measurements complemented by
14 microscopic and spectroscopic analyses highlight a complex redox behaviour in aqueous electrolyte
15 containing both Zn²⁺ and Mn²⁺, which may involve multiple simultaneous processes such as Zn²⁺
16 insertion/extraction, H⁺ insertion/extraction, ZHS precipitation/dissolution, and MnO_x deposition.
17 ~~Our results are strongly focused on the synthesis of ZMO thin films and on the comprehension of~~
18 ~~how the PLD and annealing experimental parameters affect the material properties. Indeed, since~~
19 ~~bulk ZMO was previously reported to exhibit poor electrochemical activity in the presence of Zn²⁺~~
20 ~~ions [49], a rationally designed ZMO material in terms of nano-porosity (and hence density and~~
21 ~~surface area), crystal size and orientation, phase purity, and Zn vs. Mn stoichiometry is supposed to~~
22 ~~demonstrate superior electrochemical properties, resulting in improved performances when it is~~
23 ~~implemented in a real device. For example, the porosity at the nanoscale enlarges the contact area~~
24 ~~between the active material and the electrolyte, promoting the charge transfer, while a non-~~
25 ~~stoichiometric manganite phase alleviates the electrostatic repulsion and provides vacancies for ion~~
26 ~~insertion and diffusion. Our approach based on PLD allows the control of every crucial property~~

1 separately, and the assessment of the electrochemical behaviour in ideal experimental conditions
2 (i.e., without additives/binders and in half-cell configuration) enables us to focus on the response of
3 the ZMO film alone. Further electrochemical studies, combined with *in situ* characterization and
4 analytical techniques capable of jointly yielding structural and chemical-state information, such as
5 XAFS, will be undertaken in the near future, to fully elucidate the electrochemical mechanisms of
6 the different ZMO films – in particular disentangling insertion and surface phase formation
7 processes – to optimize their structure in view of the achievement and stabilization of high-capacity
8 performance in real-life AZIBs.

9 CRediT authorship contribution statement

10 **Andrea Macrelli:** Conceptualization, Methodology, Validation, Formal Analysis, Investigation,
11 Visualization, Writing – Original Draft, Writing – Review & Editing. **Marco Olivieri:** Formal
12 Analysis, Investigation. **Alessio Lamperti:** Methodology, Investigation, Resources, Writing –
13 Review & Editing. **Valeria Russo:** Methodology, Supervision, Writing – Review & Editing.
14 **Benedetto Bozzini:** Conceptualization, Methodology, Formal Analysis, Resources, Writing –
15 Review & Editing, Supervision. **Marco Menegazzo:** Methodology, Resources. **Gianlorenzo**
16 **Bussetti:** Methodology, Resources. **Carlo S. Casari:** Conceptualization, Writing – Review &
17 Editing, Supervision. **Andrea Li Bassi:** Conceptualization, Writing – Review & Editing,
18 Supervision.

19 Declaration of competing interest

20 The authors declare that they have no known competing financial interests or personal relationships
21 that could have appeared to influence the work reported in this paper.

22 Data availability

23 Data will be made available from the corresponding author upon reasonable request.

Acknowledgments

The PhD scholarship of Andrea Macrelli and part of this research study pertain to the *Energy for Motion* project of the Department of Energy of Politecnico di Milano, funded by the Italian Ministry of University and Research (MIUR) through the *Department of Excellence* grant 2018 – 2022.

References

- 1
2
3 [1] X. Jia, C. Liu, Z.G. Neale, J. Yang, G. Cao, Active materials for aqueous zinc ion Batteries:
4
5 Synthesis, crystal structure, morphology, and electrochemistry, *Chem. Rev.* 120 (2020)
6
7 7795–7866. <https://doi.org/10.1021/acs.chemrev.9b00628>.
8
9
- 10
11 [2] T. Zhou, L. Zhu, L. Xie, Q. Han, X. Yang, L. Chen, G. Wang, X. Cao, Cathode materials for
12
13 aqueous zinc-ion batteries: A mini review, *J. Colloid Interface Sci.* 605 (2022) 828–850.
14
15 <https://doi.org/10.1016/j.jcis.2021.07.138>.
16
17
- 18
19 [3] L. Wang, J. Zheng, Recent advances in cathode materials of rechargeable aqueous zinc-ion
20
21 batteries, *Mater. Today Adv.* 7 (2020) 1000782.
22
23 <https://doi.org/10.1016/j.mtadv.2020.100078>.
24
25
- 26
27 [4] N. Wang, H. Wan, J. Duan, X. Wang, L. Tao, J. Zhang, H. Wang, A review of zinc-based
28
29 battery from alkaline to acid, *Mater. Today Adv.* 11 (2021) 100149.
30
31 <https://doi.org/10.1016/j.mtadv.2021.100149>.
32
33
- 34
35 [5] N. Borchers, S. Clark, B. Horstmann, K. Jayasayee, M. Juel, P. Stevens, Innovative zinc-
36
37 based batteries, *J. Power Sources* 484 (2021) 229309.
38
39 <https://doi.org/10.1016/j.jpowsour.2020.229309>.
40
41
- 42
43 [6] L.E. Blanc, D. Kundu, L.F. Nazar, Scientific challenges for the implementation of Zn-ion
44
45 batteries, *Joule* 4 (2020) 771–799. <https://doi.org/10.1016/j.joule.2020.03.002>.
46
47
- 48
49 [7] V.P.H. Huy, L.T. Hieu, J. Hur, Zn metal anodes for Zn-ion batteries in mild aqueous
50
51 electrolytes: Challenges and strategies, *Nanomaterials* 11 (2021) 2746.
52
53 <https://doi.org/10.3390/nano11102746>.
54
55
56
57
58
59
60
61
62
63
64
65

- 1
2
3
4
5
6
7
8
9
10
11
12
13
14
15
16
17
18
19
20
21
22
23
24
25
26
27
28
29
30
31
32
33
34
35
36
37
38
39
40
41
42
43
44
45
46
47
48
49
50
51
52
53
54
55
56
57
58
59
60
61
62
63
64
65
- [8] C. Li, X. Xie, S. Liang, J. Zhou, Issues and future perspective on zinc metal anode for rechargeable aqueous zinc-ion batteries, *Energy Environ. Mater.* 3 (2020) 146–159. <https://doi.org/10.1002/eem2.12067>.
- [9] Y. Geng, L. Pan, Z. Peng, Z. Sun, H. Lin, C. Mao, L. Wang, L. Dai, H. Liu, K. Pan, X. Wu, Q. Zhang, Z. He, Electrolyte additive engineering for aqueous Zn ion batteries, *Energy Storage Mater.* 51 (2022) 733–755. <https://doi.org/10.1016/j.ensm.2022.07.017>.
- [10] N. Guo, W. Huo, X. Dong, Z. Sun, Y. Lu, X. Wu, L. Dai, L. Wang, H. Lin, H. Liu, H. Liang, Z. He, Q. Zhang, A Review on 3D zinc anodes for zinc ion batteries, *Small Methods* 6 (2022) 2200597. <https://doi.org/10.1002/smt.202200597>.
- [11] T. Wang, C. Li, X. Xie, B. Lu, Z. He, S. Liang, J. Zhou, Anode materials for aqueous zinc ion batteries: Mechanisms, properties, and perspectives, *ACS Nano* 14 (2020) 16321–16347. <https://doi.org/10.1021/acsnano.0c07041>.
- [12] H. Li, L. Ma, C. Han, Z. Wang, Z. Liu, Z. Tang, C. Zhi, Advanced rechargeable zinc-based batteries: Recent progress and future perspectives, *Nano Energy* 62 (2019) 550–587. <https://doi.org/10.1016/j.nanoen.2019.05.059>.
- [13] B. Tang, L. Shan, S. Liang, J. Zhou, Issues and opportunities facing aqueous zinc-ion batteries, *Energy Environ. Sci.* 12 (2019) 3288–3304. <https://doi.org/10.1039/c9ee02526j>.
- [14] M. Song, H. Tan, D. Chao, H.J. Fan, Recent advances in Zn-ion batteries, *Adv. Funct. Mater.* 28 (2018) 1802564. <https://doi.org/10.1002/adfm.201802564>.
- [15] X. Guo, J. Zhou, C. Bai, X. Li, G. Fang, S. Liang, Zn/MnO₂ battery chemistry with dissolution-deposition mechanism, *Mater. Today Energy* 16 (2020) 100396. <https://doi.org/10.1016/j.mtener.2020.100396>.

- 1
2
3
4
5
6
7
8
9
10
11
12
13
14
15
16
17
18
19
20
21
22
23
24
25
26
27
28
29
30
31
32
33
34
35
36
37
38
39
40
41
42
43
44
45
46
47
48
49
50
51
52
53
54
55
56
57
58
59
60
61
62
63
64
65
- [16] B. Lee, C.S. Yoon, H.R. Lee, K.Y. Chung, B.W. Cho, S.H. Oh, Electrochemically-induced reversible transition from the tunneled to layered polymorphs of manganese dioxide, *Sci. Rep.* 4 (2014) 6066. <https://doi.org/10.1038/srep06066>.
- [17] W. Sun, F. Wang, S. Hou, C. Yang, X. Fan, Z. Ma, T. Gao, F. Han, R. Hu, M. Zhu, C. Wang, Zn/MnO₂ battery chemistry with H⁺ and Zn²⁺ coinsertion, *J. Am. Chem. Soc.* 139 (2017) 9775–9778. <https://doi.org/10.1021/jacs.7b04471>.
- [18] L. Li, T.K.A. Hoang, J. Zhi, M. Han, S. Li, P. Chen, Functioning mechanism of the secondary aqueous Zn-β-MnO₂ battery, *ACS Appl. Mater. Interfaces* 12 (2020) 12834–12846. <https://doi.org/10.1021/acsami.9b22758>.
- [19] M.H. Alfaruqi, V. Mathew, J. Gim, S. Kim, J. Song, J.P. Baboo, S.H. Choi, J. Kim, Electrochemically induced structural transformation in a γ-MnO₂ cathode of a high capacity zinc-ion battery system, *Chem. Mater.* 27 (2015) 3609–3620. <https://doi.org/10.1021/cm504717p>.
- [20] M.H. Alfaruqi, S. Islam, D.Y. Putro, V. Mathew, S. Kim, J. Jo, S. Kim, Y.K. Sun, K. Kim, J. Kim, Structural transformation and electrochemical study of layered MnO₂ in rechargeable aqueous zinc-ion battery, *Electrochim. Acta* 276 (2018) 1–11. <https://doi.org/10.1016/j.electacta.2018.04.139>.
- [21] V. Mathew, B. Sambandam, S. Kim, S. Kim, S. Park, S. Lee, M.H. Alfaruqi, V. Soundharrajan, S. Islam, D.Y. Putro, J.Y. Hwang, Y.K. Sun, J. Kim, Manganese and vanadium oxide cathodes for aqueous rechargeable zinc-ion batteries: A focused view on performance, mechanism, and developments, *ACS Energy Lett.* 5 (2020) 2376–2400. <https://doi.org/10.1021/acsenergylett.0c00740>.

- 1
2
3
4
5
6
7
8
9
10
11
12
13
14
15
16
17
18
19
20
21
22
23
24
25
26
27
28
29
30
31
32
33
34
35
36
37
38
39
40
41
42
43
44
45
46
47
48
49
50
51
52
53
54
55
56
57
58
59
60
61
62
63
64
65
- [22] W. Zhang, C. Zuo, C. Tang, W. Tang, B. Lan, X. Fu, S. Dong, P. Luo, The current developments and perspectives of V_2O_5 as cathode for rechargeable aqueous zinc-ion batteries, *Energy Technol.* 9 (2021) 2000789. <https://doi.org/10.1002/ente.202000789>.
- [23] S. Liu, L. Kang, J.M. Kim, Y.T. Chun, J. Zhang, S.C. Jun, Recent advances in vanadium-based aqueous rechargeable zinc-ion batteries, *Adv. Energy Mater.* 10 (2020). <https://doi.org/10.1002/aenm.202000477>.
- [24] G. Zampardi, F. La Mantia, Prussian blue analogues as aqueous Zn-ion batteries electrodes: Current challenges and future perspectives, *Curr. Opin. Electrochemistry* 21 (2020) 84–92. <https://doi.org/10.1016/j.coelec.2020.01.014>.
- [25] H. Cui, T. Wang, Z. Huang, G. Liang, Z. Chen, A. Chen, D. Wang, Q. Yang, H. Hong, J. Fan, C. Zhi, High-voltage organic cathodes for zinc-ion batteries through electron cloud and solvation structure regulation, *Angew. Chem. Int. Ed.* 61 (2022) e202203453. <https://doi.org/10.1002/anie.202203453>.
- [26] S. Xu, M. Sun, Q. Wang, C. Wang, Recent progress in organic electrodes for zinc-ion batteries, *J. Semicond.* 41 (2020) 091704. <https://doi.org/10.1088/1674-4926/41/9/091704>.
- [27] J. Wang, J.G. Wang, H. Liu, Z. You, C. Wei, F. Kang, Electrochemical activation of commercial MnO microsized particles for high-performance aqueous zinc-ion batteries, *J. Power Sources* 438 (2019) 226951. <https://doi.org/10.1016/j.jpowsour.2019.226951>.
- [28] C. Zhu, G. Fang, S. Liang, Z. Chen, Z. Wang, J. Ma, H. Wang, B. Tang, X. Zheng, J. Zhou, Electrochemically induced cationic defect in MnO intercalation cathode for aqueous zinc-ion battery, *Energy Storage Mater.* 24 (2020) 394–401. <https://doi.org/10.1016/j.ensm.2019.07.030>.

- 1
2
3
4
5
6
7
8
9
10
11
12
13
14
15
16
17
18
19
20
21
22
23
24
25
26
27
28
29
30
31
32
33
34
35
36
37
38
39
40
41
42
43
44
45
46
47
48
49
50
51
52
53
54
55
56
57
58
59
60
61
62
63
64
65
- [29] M. Sun, D.S. Li, Y.F. Wang, W.L. Liu, M.M. Ren, F.G. Kong, S.J. Wang, Y.Z. Guo, Y.M. Liu, Mn_3O_4 @NC composite nanorods as a cathode for rechargeable aqueous Zn-ion batteries, *ChemElectroChem* 6 (2019) 2510–2516. <https://doi.org/10.1002/celec.201900376>.
- [30] J. Hao, J. Mou, J. Zhang, L. Dong, W. Liu, C. Xu, F. Kang, Electrochemically induced spinel-layered phase transition of Mn_3O_4 in high performance neutral aqueous rechargeable zinc battery, *Electrochim. Acta* 259 (2018) 170–178. <https://doi.org/10.1016/j.electacta.2017.10.166>.
- [31] H. Jiang, X. Ji, Counter-ion insertion of chloride in Mn_3O_4 as cathode for dual-ion batteries: A new mechanism of electrosynthesis for reversible anion storage, *Carbon Energy* 2 (2020) 437–442. <https://doi.org/10.1002/cey2.37>.
- [32] C. Zhu, G. Fang, J. Zhou, J. Guo, Z. Wang, C. Wang, J. Li, Y. Tang, S. Liang, Binder-free stainless steel@ Mn_3O_4 nanoflower composite: A high-activity aqueous zinc-ion battery cathode with high-capacity and long-cycle-life, *J. Mater. Chem. A* 6 (2018) 9677–9683. <https://doi.org/10.1039/c8ta01198b>.
- [33] D. Feng, T.N. Gao, L. Zhang, B. Guo, S. Song, Z.A. Qiao, S. Dai, Boosting high-rate zinc-storage performance by the rational design of Mn_2O_3 nanoporous architecture cathode, *Nano-Micro Lett.* 12 (2020) 14. <https://doi.org/10.1007/s40820-019-0351-4>.
- [34] Y. Ma, Y. Ma, T. Diemant, K. Cao, X. Liu, U. Kaiser, R.J. Behm, A. Varzi, S. Passerini, Unveiling the intricate intercalation mechanism in manganese sesquioxide as positive electrode in aqueous Zn-metal battery, *Adv. Energy Mater.* 11 (2021) 2100962. <https://doi.org/10.1002/aenm.202100962>.
- [35] B. Jiang, C. Xu, C. Wu, L. Dong, J. Li, F. Kang, Manganese sesquioxide as cathode material for multivalent zinc ion battery with high capacity and long cycle life, *Electrochim. Acta* 229 (2017) 422–428. <https://doi.org/10.1016/j.electacta.2017.01.163>.

- 1
2
3
4
5
6
7
8
9
10
11
12
13
14
15
16
17
18
19
20
21
22
23
24
25
26
27
28
29
30
31
32
33
34
35
36
37
38
39
40
41
42
43
44
45
46
47
48
49
50
51
52
53
54
55
56
57
58
59
60
61
62
63
64
65
- [36] Y. Cai, R. Chua, S. Huang, H. Ren, M. Srinivasan, Amorphous manganese dioxide with the enhanced pseudocapacitive performance for aqueous rechargeable zinc-ion battery, *Chem. Eng. J.* 396 (2020) 125221. <https://doi.org/10.1016/j.cej.2020.125221>.
- [37] Y. Wu, J. Fee, Z. Tobin, A. Shirazi-Amin, P. Kerns, S. Dissanayake, A. Mirich, S.L. Suib, Amorphous manganese oxides: An approach for reversible aqueous zinc-ion batteries, *ACS Appl. Energy Mater.* 3 (2020) 1627–1633. <https://doi.org/10.1021/acsaem.9b02119>.
- [38] M.H. Alfaruqi, J. Gim, S. Kim, J. Song, J. Jo, S. Kim, V. Mathew, J. Kim, Enhanced reversible divalent zinc storage in a structurally stable α -MnO₂ nanorod electrode, *J. Power Sources* 288 (2015) 320–327. <https://doi.org/10.1016/j.jpowsour.2015.04.140>.
- [39] B. Lee, H.R. Lee, H. Kim, K.Y. Chung, B.W. Cho, S.H. Oh, Elucidating the intercalation mechanism of zinc ions into α -MnO₂ for rechargeable zinc batteries, *Chem. Commun.* 51 (2015) 9265–9268. <https://doi.org/10.1039/c5cc02585k>.
- [40] S. Islam, M.H. Alfaruqi, V. Mathew, J. Song, S. Kim, S. Kim, J. Jo, J.P. Baboo, D.T. Pham, D.Y. Putro, Y.K. Sun, J. Kim, Facile synthesis and the exploration of the zinc storage mechanism of β -MnO₂ nanorods with exposed (101) planes as a novel cathode material for high performance eco-friendly zinc-ion batteries, *J. Mater. Chem. A* 5 (2017) 23299–23309. <https://doi.org/10.1039/c7ta07170a>.
- [41] M.H. Alfaruqi, J. Gim, S. Kim, J. Song, D.T. Pham, J. Jo, Z. Xiu, V. Mathew, J. Kim, A layered δ -MnO₂ nanoflake cathode with high zinc-storage capacities for eco-friendly battery applications, *Electrochem. Commun.* 60 (2015) 121–125. <https://doi.org/10.1016/j.elecom.2015.08.019>.
- [42] C. Guo, H. Liu, J. Li, Z. Hou, J. Liang, J. Zhou, Y. Zhu, Y. Qian, Ultrathin δ -MnO₂ nanosheets as cathode for aqueous rechargeable zinc ion battery, *Electrochim. Acta* 304 (2019) 370–377. <https://doi.org/10.1016/j.electacta.2019.03.008>.

- 1
2
3
4
5
6
7
8
9
10
11
12
13
14
15
16
17
18
19
20
21
22
23
24
25
26
27
28
29
30
31
32
33
34
35
36
37
38
39
40
41
42
43
44
45
46
47
48
49
50
51
52
53
54
55
56
57
58
59
60
61
62
63
64
65
- [43] D. Chao, W. Zhou, C. Ye, Q. Zhang, Y. Chen, L. Gu, K. Davey, S. Qiao, An electrolytic Zn–MnO₂ battery for high- voltage and scalable energy storage, *Angew. Chem. Int. Ed.* 58 (2019) 7823–7828. <https://doi.org/https://doi.org/10.1002/anie.201904174>.
- [44] C. Yuan, Y. Zhang, Y. Pan, X. Liu, G. Wang, D. Cao, Investigation of the intercalation of polyvalent cations (Mg²⁺, Zn²⁺) into λ-MnO₂ for rechargeable aqueous battery, *Electrochim. Acta* 116 (2014) 404–412. <https://doi.org/10.1016/j.electacta.2013.11.090>.
- [45] J. Lee, J.B. Ju, W. il Cho, B.W. Cho, S.H. Oh, Todorokite-type MnO₂ as a zinc-ion intercalating material, *Electrochim. Acta* 112 (2013) 138–143. <https://doi.org/10.1016/j.electacta.2013.08.136>.
- [46] L. Nádherný, M. Maryško, D. Sedmidubský, C. Martin, Structural and magnetic properties of Zn_xMn_{3-x}O₄ spinels, *J. Magn. Magn. Mater.* 413 (2016) 89–96. <https://doi.org/10.1016/j.jmmm.2016.04.029>.
- [47] M. Peiteado, S. Sturm, A.C. Caballero, D. Makovec, Mn_{3-x}Zn_xO₄ spinel phases in the Zn–Mn–O system, *Acta Mater.* 56 (2008) 4028–4035. <https://doi.org/10.1016/j.actamat.2008.04.024>.
- [48] S. Guillemet-Fritsch, C. Chanel, J. Sarrias, S. Bayonne, A. Rousset, X. Alcobe, M.L. Martinez Sarriòn, Structure, thermal stability and electrical properties of zinc manganites, *Solid State Ion.* 128 (2000) 233–242. [https://doi.org/https://doi.org/10.1016/S0167-2738\(99\)00340-9](https://doi.org/https://doi.org/10.1016/S0167-2738(99)00340-9).
- [49] L. Malavasi, P. Galinetto, M.C. Mozzati, C.B. Azzoni, G. Flor, Raman spectroscopy of AMn₂O₄ (A = Mn, Mg and Zn) spinels, *Phys. Chem. Chem. Phys.* 4 (2002) 3876–3880. <https://doi.org/10.1039/b203520k>.

- 1
2
3
4
5
6
7
8
9
10
11
12
13
14
15
16
17
18
19
20
21
22
23
24
25
26
27
28
29
30
31
32
33
34
35
36
37
38
39
40
41
42
43
44
45
46
47
48
49
50
51
52
53
54
55
56
57
58
59
60
61
62
63
64
65
- [50] A. Baby, B. Senthilkumar, P. Barpanda, Low-cost rapid template-free synthesis of nanoscale zinc spinels for energy storage and electrocatalytic applications, *ACS Appl. Energy Mater.* 2 (2019) 3211–3219. <https://doi.org/10.1021/acsaem.9b00054>.
- [51] N. Zhang, F. Cheng, Y. Liu, Q. Zhao, K. Lei, C. Chen, X. Liu, J. Chen, Cation-deficient spinel ZnMn_2O_4 cathode in $\text{Zn}(\text{CF}_3\text{SO}_3)_2$ electrolyte for rechargeable aqueous Zn-ion battery, *J. Am. Chem. Soc.* 138 (2016) 12894–12901. <https://doi.org/10.1021/jacs.6b05958>.
- [52] J.C. Knight, S. Therese, A. Manthiram, Chemical extraction of Zn from ZnMn_2O_4 -based spinels, *J. Mater. Chem. A* 3 (2015) 21077–21082. <https://doi.org/10.1039/c5ta06482a>.
- [53] K. Cai, S. hua Luo, J. Feng, J. Wang, Y. Zhan, Q. Wang, Y. Zhang, X. Liu, Recent advances on spinel zinc manganate cathode materials for zinc-ion batteries, *Chem. Rec.* 22 (2022) e202100169. <https://doi.org/10.1002/tcr.202100169>.
- [54] H. Zhang, J. Wang, Q. Liu, W. He, Z. Lai, X. Zhang, M. Yu, Y. Tong, X. Lu, Extracting oxygen anions from ZnMn_2O_4 : Robust cathode for flexible all-solid-state Zn-ion batteries, *Energy Storage Mater.* 21 (2019) 154–161. <https://doi.org/10.1016/j.ensm.2018.12.019>.
- [55] J.W. Lee, S.D. Seo, D.W. Kim, Comparative study on ternary spinel cathode Zn–Mn–O microspheres for aqueous rechargeable zinc-ion batteries, *J. Alloys Compd.* 800 (2019) 478–482. <https://doi.org/10.1016/j.jallcom.2019.06.051>.
- [56] T.H. Wu, W.Y. Liang, Reduced intercalation energy barrier by rich structural water in spinel ZnMn_2O_4 for high-rate zinc-ion batteries, *ACS Appl. Mater. Interfaces* 13 (2021) 23822–23832. <https://doi.org/10.1021/acsaami.1c05150>.
- [57] S. Islam, M.H. Alfaruqi, D.Y. Putro, S. Park, S. Kim, S. Lee, M.S. Ahmed, V. Mathew, Y.K. Sun, J.Y. Hwang, J. Kim, In situ oriented Mn deficient ZnMn_2O_4 @C nanoarchitecture for durable rechargeable aqueous zinc-ion batteries, *Adv. Sci.* 8 (2021) 2002636. <https://doi.org/10.1002/advs.202002636>.

- 1
2
3
4
5
6
7
8
9
10
11
12
13
14
15
16
17
18
19
20
21
22
23
24
25
26
27
28
29
30
31
32
33
34
35
36
37
38
39
40
41
42
43
44
45
46
47
48
49
50
51
52
53
54
55
56
57
58
59
60
61
62
63
64
65
- [58] S. Wang, S. Zhang, X. Chen, G. Yuan, B. Wang, J. Bai, H. Wang, G. Wang, Double-shell zinc manganate hollow microspheres embedded in carbon networks as cathode materials for high-performance aqueous zinc-ion batteries, *J. Colloid Interface Sci.* 580 (2020) 528–539. <https://doi.org/10.1016/j.jcis.2020.07.053>.
- [59] X. Wu, Y. Xiang, Q. Peng, X. Wu, Y. Li, F. Tang, R. Song, Z. Liu, Z. He, X. Wu, Green-low-cost rechargeable aqueous zinc-ion batteries using hollow porous spinel ZnMn_2O_4 as the cathode material, *J. Mater. Chem. A* 5 (2017) 17990–17997. <https://doi.org/10.1039/c7ta00100b>.
- [60] L. Chen, Z. Yang, H. Qin, X. Zeng, J. Meng, H. Chen, Graphene-wrapped hollow ZnMn_2O_4 microspheres for high-performance cathode materials of aqueous zinc ion batteries, *Electrochim. Acta* 317 (2019) 155–163. <https://doi.org/10.1016/j.electacta.2019.05.147>.
- [61] L. Chen, Z. Yang, H. Qin, X. Zeng, J. Meng, Advanced electrochemical performance of $\text{ZnMn}_2\text{O}_4/\text{N}$ -doped graphene hybrid as cathode material for zinc ion battery, *J. Power Sources* 425 (2019) 162–169. <https://doi.org/10.1016/j.jpowsour.2019.04.010>.
- [62] M.B. Sassin, M.E. Helms, J.F. Parker, C.N. Chervin, R.H. Deblock, J.S. Ko, D.R. Rolison, J.W. Long, Elucidating zinc-ion battery mechanisms in freestanding carbon electrode architectures decorated with nanocrystalline ZnMn_2O_4 , *Mater. Adv.* 2 (2021) 2730–2738. <https://doi.org/10.1039/d1ma00159k>.
- [63] Z. Yao, D. Cai, Z. Cui, Q. Wang, H. Zhan, Strongly coupled zinc manganate nanodots and graphene composite as an advanced cathode material for aqueous zinc ion batteries, *Ceram. Int.* 46 (2020) 11237–11245. <https://doi.org/10.1016/j.ceramint.2020.01.148>.
- [64] C. Yang, M. Han, H. Yan, F. Li, M. Shi, L. Zhao, In-situ probing phase evolution and electrochemical mechanism of ZnMn_2O_4 nanoparticles anchored on porous carbon

polyhedrons in high-performance aqueous Zn-ion batteries, *J. Power Sources* 452 (2020) 227826. <https://doi.org/10.1016/j.jpowsour.2020.227826>.

[65] S. Deng, Z. Tie, F. Yue, H. Cao, M. Yao, Z. Niu, Rational design of ZnMn₂O₄ quantum dots in a carbon framework for durable aqueous zinc-ion batteries, *Angew. Chem. Int. Ed.* 61 (2022) e202115877. <https://doi.org/10.1002/anie.202115877>.

[66] Y. Tao, Z. Li, L. Tang, X. Pu, T. Cao, D. Cheng, Q. Xu, H. Liu, Y.G. Wang, Y. Xia, Nickel and cobalt co-substituted spinel ZnMn₂O₄@N-rGO for increased capacity and stability as a cathode material for rechargeable aqueous zinc-ion battery, *Electrochim. Acta* 331 (2020) 135296. <https://doi.org/10.1016/j.electacta.2019.135296>.

[67] K. Cai, S. Luo, J. Cong, K. Li, S. Yan, P. Hou, Q. Wang, Y. Zhang, X. Liu, X. Lei, Synthesis and optimization of ZnMn₂O₄ cathode material for zinc-ion battery by citric acid sol-gel method, *J. Electrochem. Soc.* 169 (2022) 030531. <https://doi.org/10.1149/1945-7111/ac5baa>.

[68] T. Shao, Y. Zhang, T. Cao, Y. Yang, Z. Li, H. Liu, Y. Wang, X. Yongyao, Structural regulation of ZnMn₂O₄ cathode material by K, Fe-double doping to improve its rate and cycling stability for rechargeable aqueous zinc-based batteries, *Chem. Eng. J.* 431 (2022) 133735. <https://doi.org/10.1016/j.cej.2021.133735>.

[69] S. Yang, M. Zhang, X. Wu, X. Wu, F. Zeng, Y. Li, S. Duan, D. Fan, Y. Yang, X. Wu, The excellent electrochemical performances of ZnMn₂O₄/Mn₂O₃: The composite cathode material for potential aqueous zinc ion batteries, *J. Electroanal. Chem.* 832 (2019) 69–74. <https://doi.org/10.1016/j.jelechem.2018.10.051>.

[70] Y. Zeng, Y. Wang, Q. Jin, Z. Pei, D. Luan, X. Zhang, X.W. Lou, Rationally designed Mn₂O₃-ZnMn₂O₄ hollow heterostructures from metal-organic frameworks for stable Zn-ion

storage, *Angew. Chem. Int. Ed.* 60 (2021) 25793–25798.

<https://doi.org/10.1002/anie.202113487>.

- [71] S.C. Ma, M. Sun, S.X. Wang, D.S. Li, W.L. Liu, M.M. Ren, F.G. Kong, S.J. Wang, Y.M. Xia, Zinc manganate/manganic oxide bi-component nanorod as excellent cathode for zinc-ion battery, *Scr. Mater.* 194 (2021) 113707.
<https://doi.org/10.1016/j.scriptamat.2020.113707>.
- [72] M. Shi, B. Wang, Y. Shen, J. Jiang, W. Zhu, Y. Su, M. Narayanasamy, S. Angaiah, C. Yan, Q. Peng, 3D assembly of MXene-stabilized spinel ZnMn_2O_4 for highly durable aqueous zinc-ion batteries, *Chem. Eng. J.* 399 (2020) 125627.
<https://doi.org/10.1016/j.cej.2020.125627>.
- [73] W. Qiu, H. Xiao, H. Feng, Z. Lin, H. Gao, W. He, X. Lu, Defect modulation of ZnMn_2O_4 nanotube arrays as high-rate and durable cathode for flexible quasi-solid-state zinc ion battery, *Chem. Eng. J.* 422 (2021) 129890. <https://doi.org/10.1016/j.cej.2021.129890>.
- [74] T.H. Wu, C.C. Huang, S.L. Cheng, C.C. Lin, Expanded spinel $\text{Zn}_x\text{Mn}_2\text{O}_4$ induced by electrochemical activation of glucose-mediated manganese oxide for stable cycle performance in zinc-ion batteries, *J. Colloid Interface Sci.* 617 (2022) 274–283.
<https://doi.org/10.1016/j.jcis.2022.03.017>.
- [75] V. Soundharajan, B. Sambandam, S. Kim, S. Islam, J. Jo, S. Kim, V. Mathew, Y. kook Sun, J. Kim, The dominant role of Mn^{2+} additive on the electrochemical reaction in ZnMn_2O_4 cathode for aqueous zinc-ion batteries, *Energy Storage Mater.* 28 (2020) 407–417. <https://doi.org/10.1016/j.ensm.2019.12.021>.
- [76] C.M. Julien, A. Mauger, Pulsed laser deposited films for microbatteries, *Coatings* 9 (2019) 386. <https://doi.org/doi:10.3390/coatings9060386>.

- 1
2
3
4
5
6
7
8
9
10
11
12
13
14
15
16
17
18
19
20
21
22
23
24
25
26
27
28
29
30
31
32
33
34
35
36
37
38
39
40
41
42
43
44
45
46
47
48
49
50
51
52
53
54
55
56
57
58
59
60
61
62
63
64
65
- [77] M. Fenech, N. Sharma, Pulsed laser deposition-based thin film microbatteries, *Chem. Asian. J.* 15 (2020) 1829–1847. <https://doi.org/10.1002/asia.202000384>.
- [78] L. Indrizzi, N. Ohannessian, D. Pergolesi, T. Lippert, E. Gilardi, Pulsed laser deposition as a tool for the development of all solid-state microbatteries, *Helv. Chim. Acta.* 104 (2021) e2000203. <https://doi.org/10.1002/hlca.202000203>.
- [79] P.R. Willmott, J.R. Huber, Pulsed laser vaporization and deposition, *Rev. Mod. Phys.* 72 (2000) 315–328. <https://doi.org/https://doi.org/10.1103/RevModPhys.72.315>.
- [80] C.S. Casari, A. Li Bassi, Pulsed Laser Deposition of nanostructured oxides: From clusters to functional films, in: W.T. Arkin (Ed.), *Advances in Laser and Optics Research*, Vol. 7, Ch. 2, Nova Science Publishers, Inc., Hauppauge (NY), USA, 2011, pp. 65–100.
- [81] F. Rossi, E. Marini, M. Boniardi, A. Casaroli, A. Li Bassi, A. Macrelli, C. Mele, B. Bozzini, What happens to MnO₂ when it comes in contact with Zn²⁺? An electrochemical study in aid of Zn/MnO₂-based rechargeable batteries, *Energy Technol.* 10 (2022) 2200084. <https://doi.org/10.1002/ente.202200084>.
- [82] S. Åsbrink, A. Waśkowska, L. Gerward, J. Staun Olsen, E. Talik, High-pressure phase transition and properties of spinel ZnMn₂O₄, *Phys. Rev. B.* 60 (1999) 12651–12656. <https://doi.org/10.1103/PhysRevB.60.12651>.
- [83] R. Matarrese, I. Nova, A. Li Bassi, C.S. Casari, V. Russo, S. Palmas, Preparation and optimization of TiO₂ photoanodes fabricated by pulsed laser deposition for photoelectrochemical water splitting, *J. Solid State Electrochem.* 21 (2017) 3139–3154. <https://doi.org/10.1007/s10008-017-3639-7>.
- [84] P. Gondoni, P. Mazzolini, V. Russo, M. Diani, M. Amati, L. Gregoratti, V. De Renzi, G.C. Gazzadi, J. Martí-Rujas, A. Li Bassi, C.S. Casari, Tuning electrical properties of

1 hierarchically assembled Al-doped ZnO nanoforests by room temperature Pulsed Laser
2 Deposition, *Thin Solid Films* 594 (2015) 12–17. <https://doi.org/10.1016/j.tsf.2015.09.066>.

- 3
4
5 [85] A. Bailini, F. Di Fonzo, M. Fusi, C.S. Casari, A. Li Bassi, V. Russo, A. Baserga, C.E.
6 Bottani, Pulsed laser deposition of tungsten and tungsten oxide thin films with tailored
7 structure at the nano- and mesoscale, *Appl. Surf. Sci.* 253 (2007) 8130–8135.
8 <https://doi.org/10.1016/j.apsusc.2007.02.145>.
9
10
11
12
13
14
15 [86] B.R. Bricchi, L. Mascaretti, S. Garattoni, M. Mazza, M. Ghidelli, A. Naldoni, A. Li Bassi,
16 Nanoporous titanium (oxy)nitride films as broadband solar absorbers, *ACS Appl. Mater.*
17 *Interfaces* 14 (2022) 18453–18463. <https://doi.org/10.1021/acsami.2c01185>.
18
19
20
21
22
23 [87] F. Di Fonzo, C.S. Casari, V. Russo, M.F. Brunella, A. Li Bassi, C.E. Bottani, Hierarchically
24 organized nanostructured TiO₂ for photocatalysis applications, *Nanotechnology* 20 (2009)
25 015604. <https://doi.org/10.1088/0957-4484/20/1/015604>.
26
27
28
29
30
31 [88] H. Li, B. Song, W.J. Wang, X.L. Chen, Facile synthesis, thermal, magnetic, Raman
32 characterizations of spinel structure ZnMn₂O₄, *Mater. Chem. Phys.* 130 (2011) 39–44.
33 <https://doi.org/10.1016/j.matchemphys.2011.04.072>.
34
35
36
37
38
39 [89] K. Samanta, S. Dussan, R.S. Katiyar, P. Bhattacharya, Structural and optical properties of
40 nanocrystalline Zn_{1-x}Mn_xO, *Appl. Phys. Lett.* 90 (2007) 261903.
41 <https://doi.org/10.1063/1.2751593>.
42
43
44
45
46
47 [90] C.M. Julien, M. Massot, C. Poinignon, Lattice vibrations of manganese oxides: Part I.
48 Periodic structures, *Spectrochim. Acta A Mol. Biomol. Spectrosc.* 60 (2004) 689–700.
49 [https://doi.org/10.1016/S1386-1425\(03\)00279-8](https://doi.org/10.1016/S1386-1425(03)00279-8).
50
51
52
53
54
55 [91] M. Tortosa, F.J. Manjón, M. Mollar, B. Marí, ZnO-based spinels grown by
56 electrodeposition, *J. Phys. Chem. Solids.* 73 (2012) 1111–1115.
57 <https://doi.org/10.1016/j.jpcs.2012.04.002>.
58
59
60
61
62
63
64
65

- 1
2
3
4
5
6
7
8
9
10
11
12
13
14
15
16
17
18
19
20
21
22
23
24
25
26
27
28
29
30
31
32
33
34
35
36
37
38
39
40
41
42
43
44
45
46
47
48
49
50
51
52
53
54
55
56
57
58
59
60
61
62
63
64
65
- [92] J. Zuo, C. Xu, Y. Liu, Y. Qian, Crystallite size effects on the Raman spectra of Mn₃O₄, *NanoStructured Mater.* 10 (1998) 1331–1335. [https://doi.org/https://doi.org/10.1016/S0965-9773\(99\)00002-1](https://doi.org/https://doi.org/10.1016/S0965-9773(99)00002-1).
- [93] A.V. Chichagov, D.A. Varlamov, R.A. Dilanyan, T.N. Dokina, N.A. Drozhzhina, O.L. Samokhvalova, T.V. Ushakovskaya, MINCRYST: A crystallographic database for minerals, local and network (WWW) versions, *Crystallogr. Rep.* 46 (2001) 876–879. <https://doi.org/https://doi.org/10.1134/1.1405882>.
- [94] WWW-MINCRYST. Crystallographic and crystallochemical database for minerals and their structural analogues. <http://database.iem.ac.ru/mincryst> (accessed July 29, 2022).
- [95] G.K. Williamson, W.H. Hall, X-ray line broadening from filed aluminium and wolfram, *Acta Metall.* 1 (1953) 22–31. [https://doi.org/https://doi.org/10.1016/0001-6160\(53\)90006-6](https://doi.org/https://doi.org/10.1016/0001-6160(53)90006-6).
- [96] D. Nath, F. Singh, R. Das, X-ray diffraction analysis by Williamson-Hall, Halder-Wagner and size-strain plot methods of CdSe nanoparticles - a comparative study, *Mater. Chem. Phys.* 239 (2020) 122021. <https://doi.org/10.1016/j.matchemphys.2019.122021>.
- [97] S. Bernardini, F. Bellatreccia, A. Casanova Municchia, G. Della Ventura, A. Sodo, Raman spectra of natural manganese oxides, *J. Raman Spectrosc.* 50 (2019) 873–888. <https://doi.org/10.1002/jrs.5583>.
- [98] J. Yang, J. Cao, Y. Peng, W. Yang, S. Barg, Z. Liu, I.A. Kinloch, M.A. Bissett, R.A.W. Dryfe, Unravelling the mechanism of rechargeable aqueous Zn–MnO₂ batteries: Implementation of charging process by electrodeposition of MnO₂, *ChemSusChem* 13 (2020) 4103–4110. <https://doi.org/10.1002/cssc.202001216>.

Figures and captions

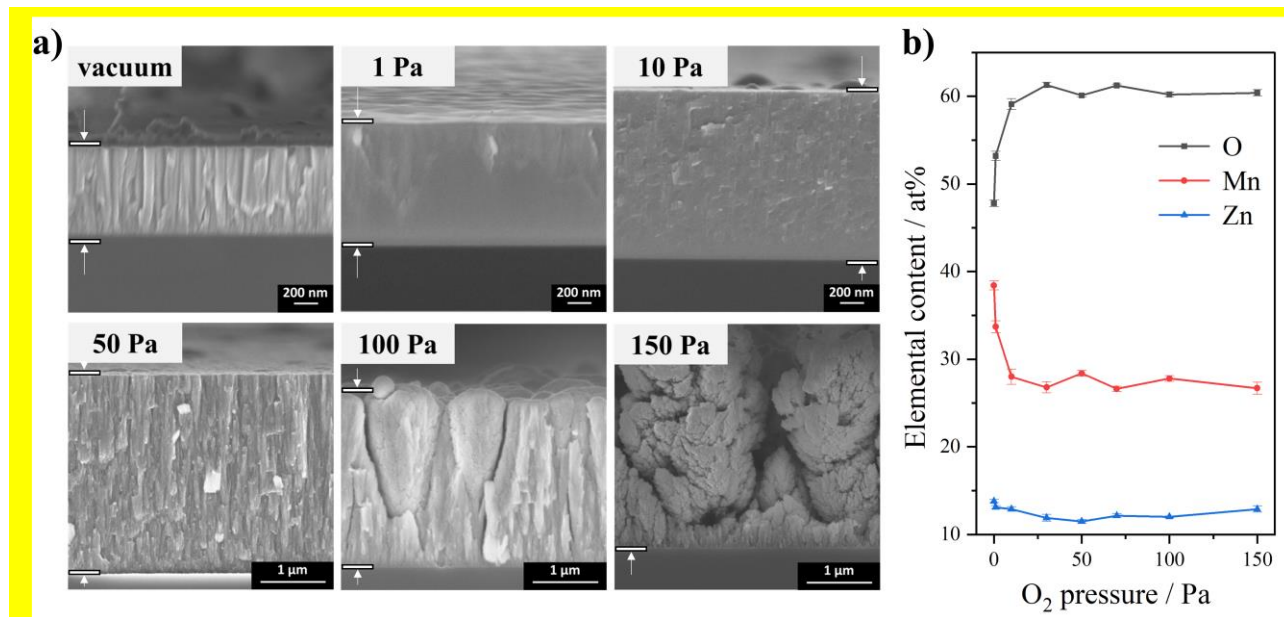


Fig. 1. (a) SEM cross-sectional images of the ZMO thin films deposited on Si at different O₂ pressure, at constant laser fluence of $\sim 3.7 \text{ J cm}^{-2}$ and 15 min deposition time. (b) EDX elemental analysis of as-deposited ZMO films.

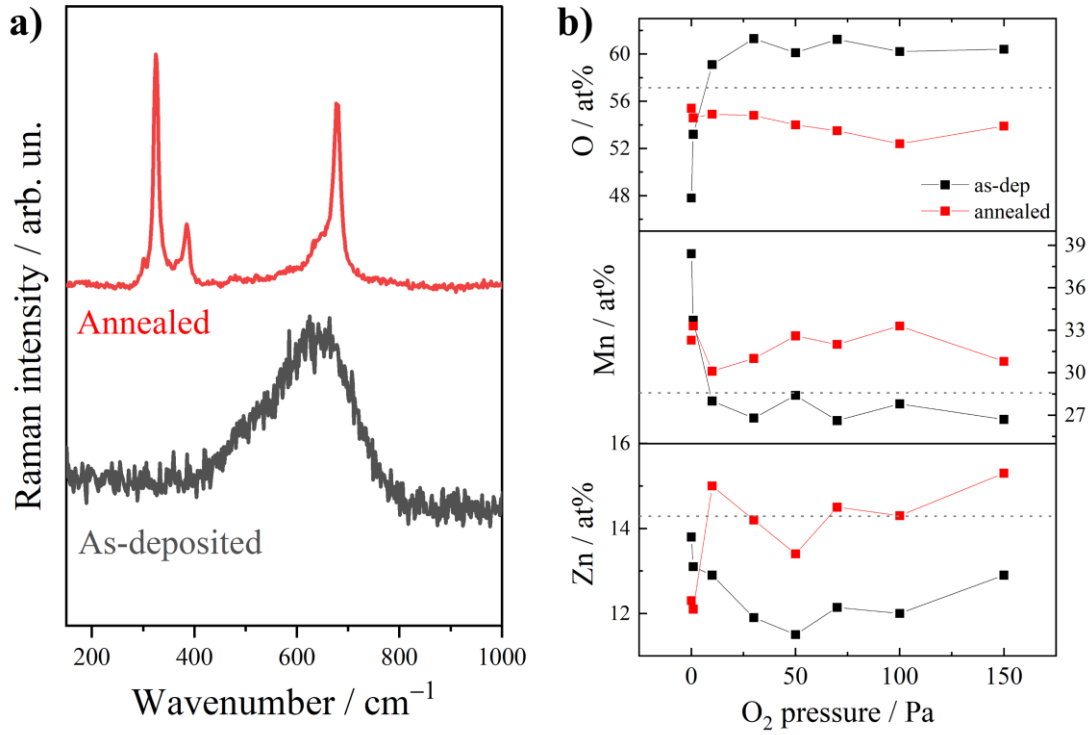


Fig. 2. (a) Comparison between the Raman spectra of the ZMO film deposited at 50 Pa of O₂ (~3.7 J cm⁻²) before and after air annealing at 600 °C, 3h. (b) EDX elemental analysis of air-annealed ZMO films (600 °C, 3h); for comparison, also the atomic content of as-deposited samples is reported. The grey dashed lines correspond to O, Mn, and Zn atomic percentages in ideally stoichiometric ZnMn₂O₄.

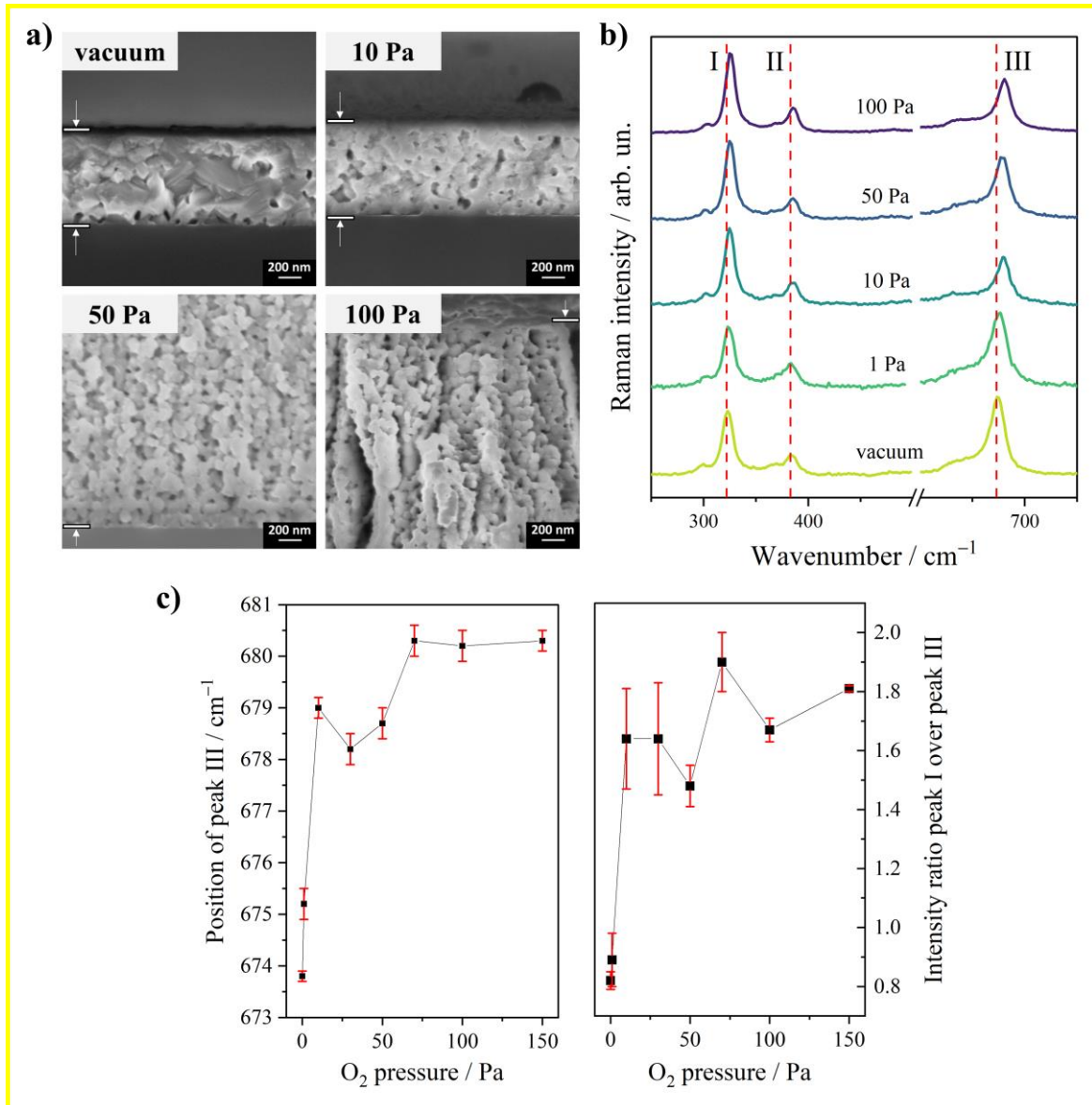


Fig. 3. (a) SEM cross-sectional images of the ZMO thin films air-annealed at 600 °C, 3h, and deposited on Si with constant laser fluence of $\sim 3.7 \text{ J cm}^{-2}$ and in vacuum, 10 Pa, 50 Pa, and 100 Pa of O₂. (b) Evolution of the Raman spectral features of crystallized samples as a function of the O₂ deposition pressure (the three main peaks are here labelled as I, II, and III). (c) Position of peak III (A_{1g} mode) and intensity ratio between peak I and peak III as a function of the O₂ deposition pressure.

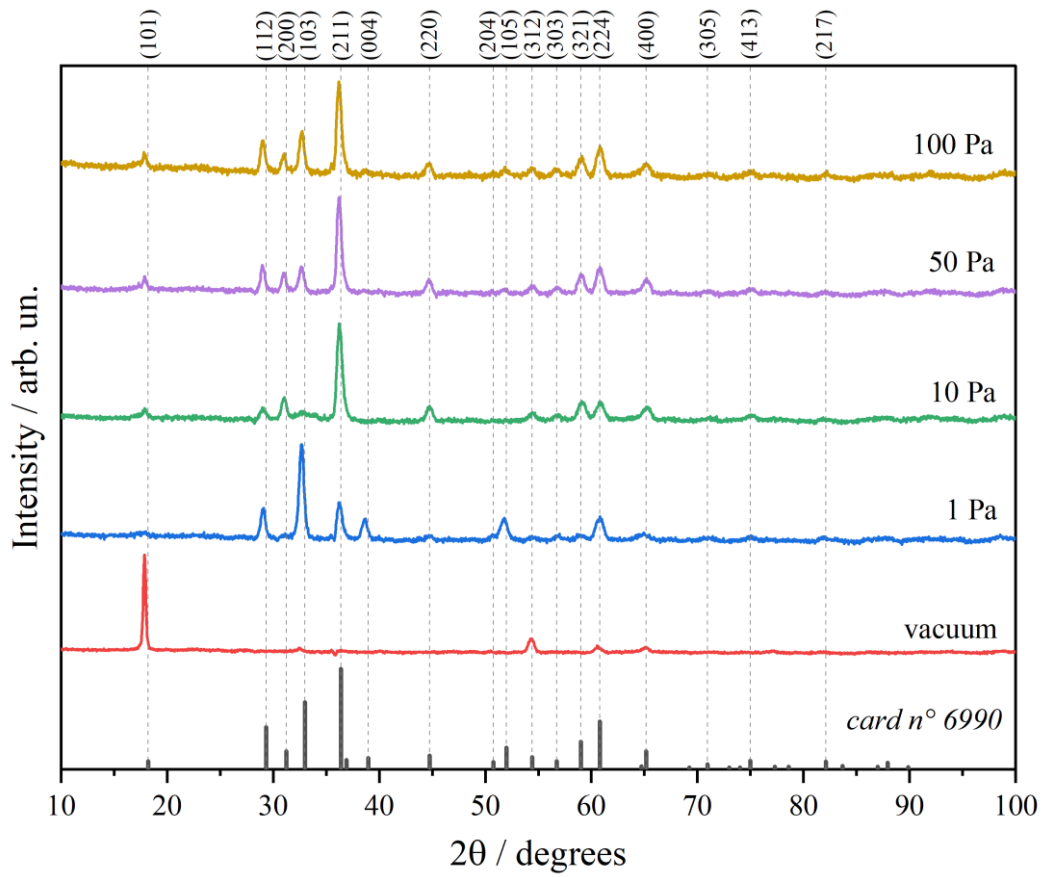


Fig. 4. GIXRD patterns of crystalline ZMO thin films, produced at different O₂ pressures and annealed in air at 600 °C, 3 h.

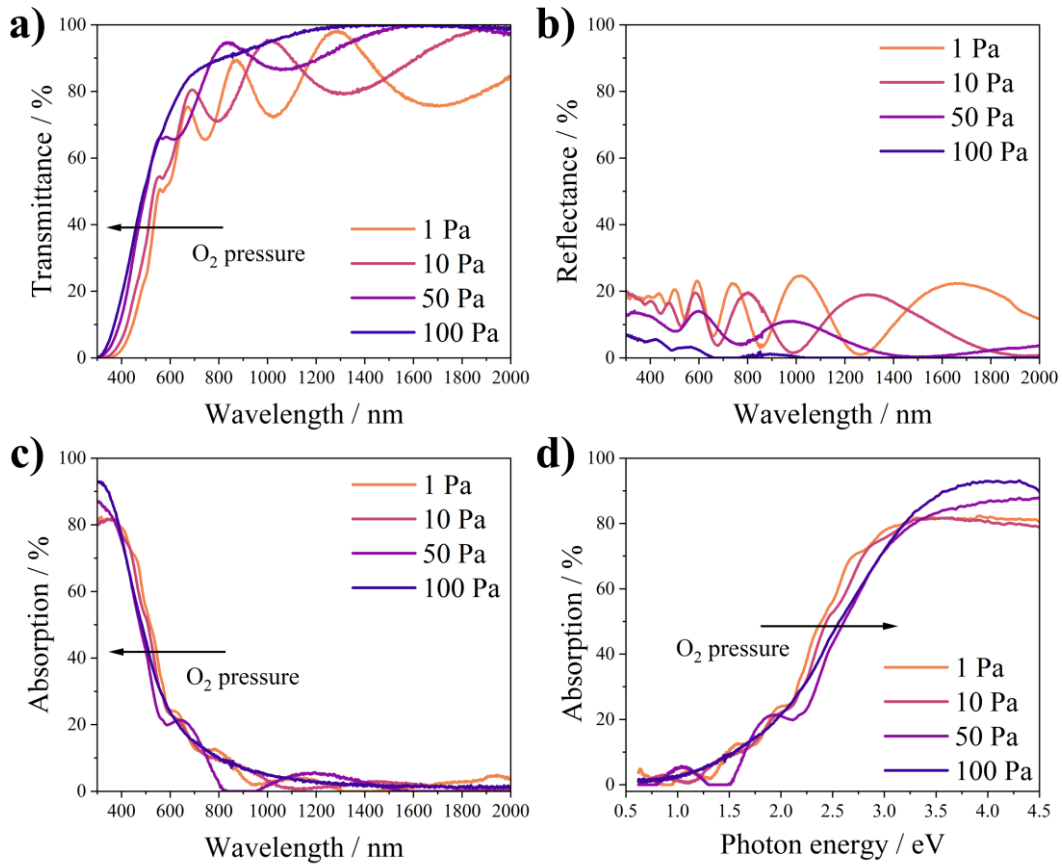


Fig. 5. UV-Vis (a) transmittance, (b) reflectance, and (c) absorption curves in the wavelength range 300–2000 nm of crystalline ZMO samples deposited at 1, 10, 50, and 100 Pa of O₂, and annealed in air at 500 °C for 2h. (d) UV-Vis absorption curves plotted as a function of photon energy in the range 0.5–4.5 eV.

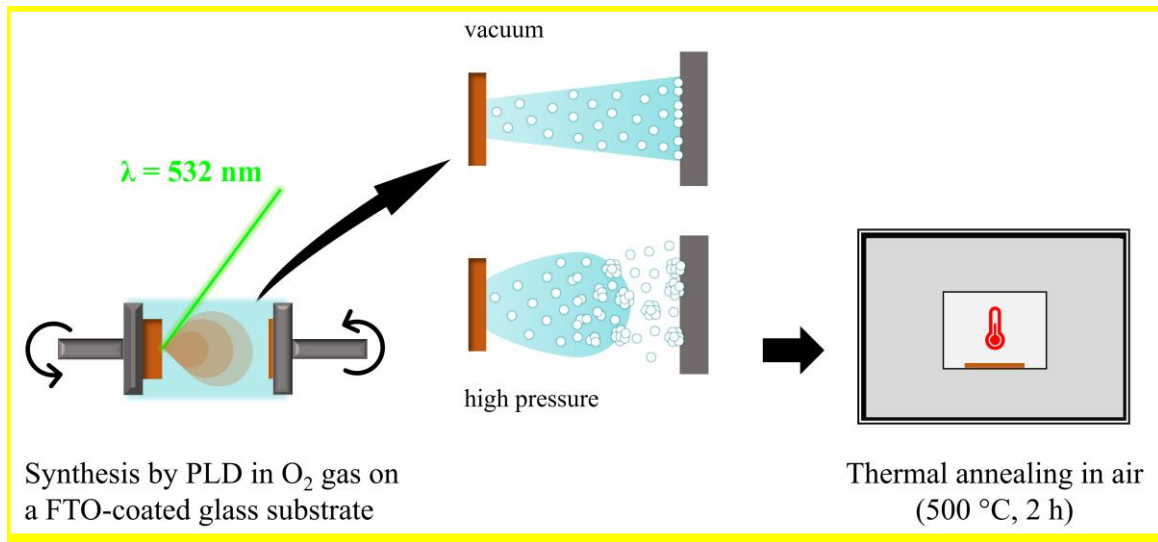


Fig. 6. Schematic illustration of the preparation of ZMO thin films for the purpose of the electrochemical characterization.

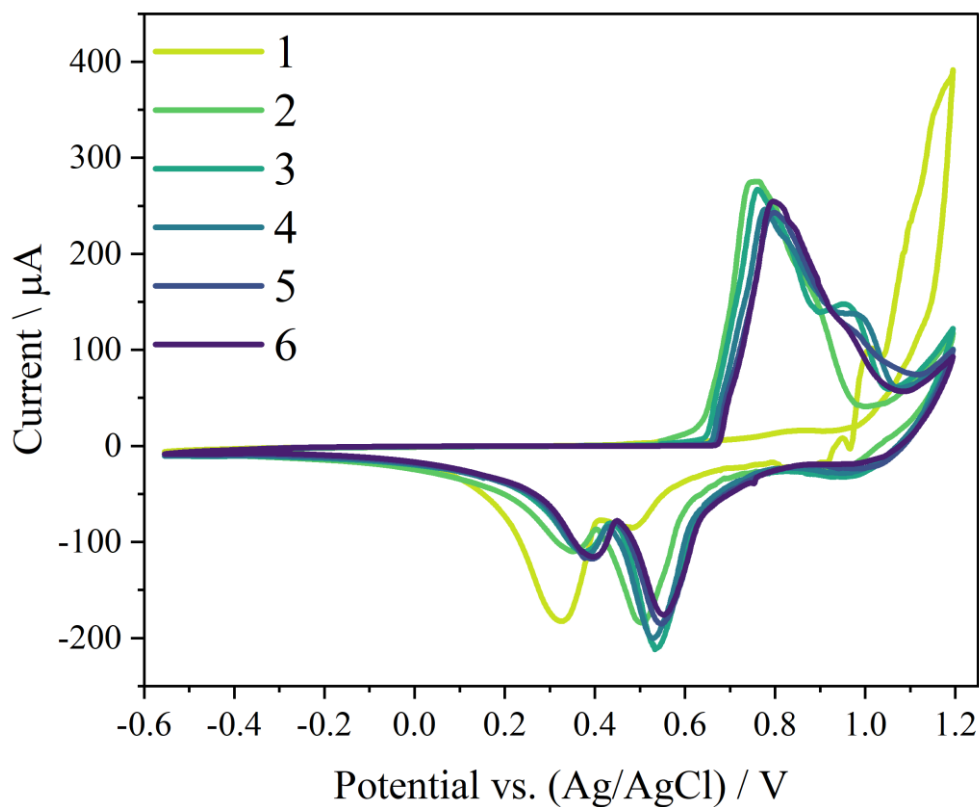


Fig. 6-7. CV curves at a scan rate of 1 mV s^{-1} of the ZMO thin film deposited at 50 Pa of O_2 and crystallized in air at $500 \text{ }^\circ\text{C}$, 2h.

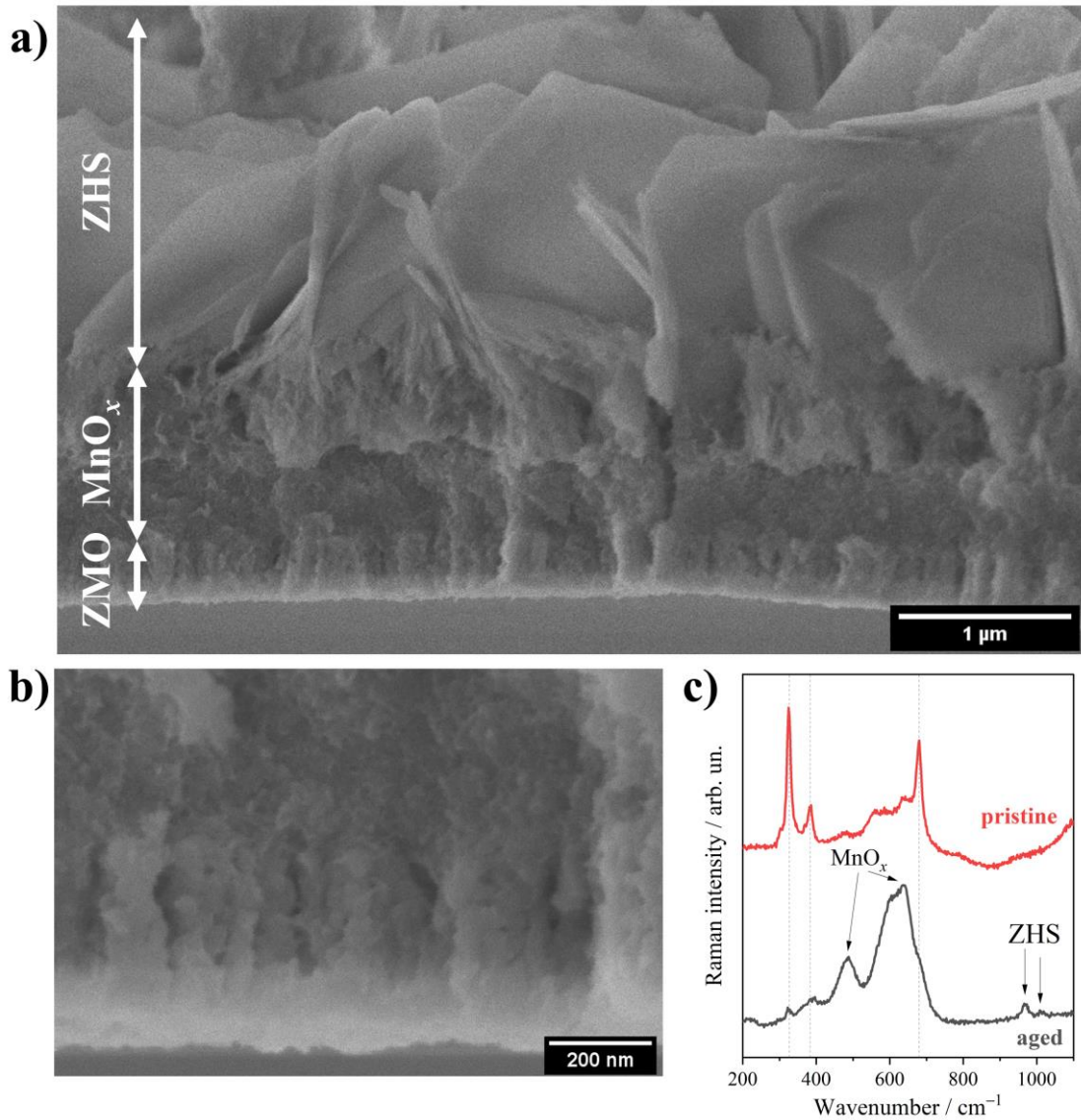


Fig. 78. SEM cross-sectional image of (a) the whole aged ZMO film and (b) the bottom layer after 6 CV cycles at 1 mV s^{-1} . (c) Raman spectra comparing the pristine (i.e., after annealing) and the aged film. The characteristic Raman features of MnO_x and ZHS phase are highlighted.

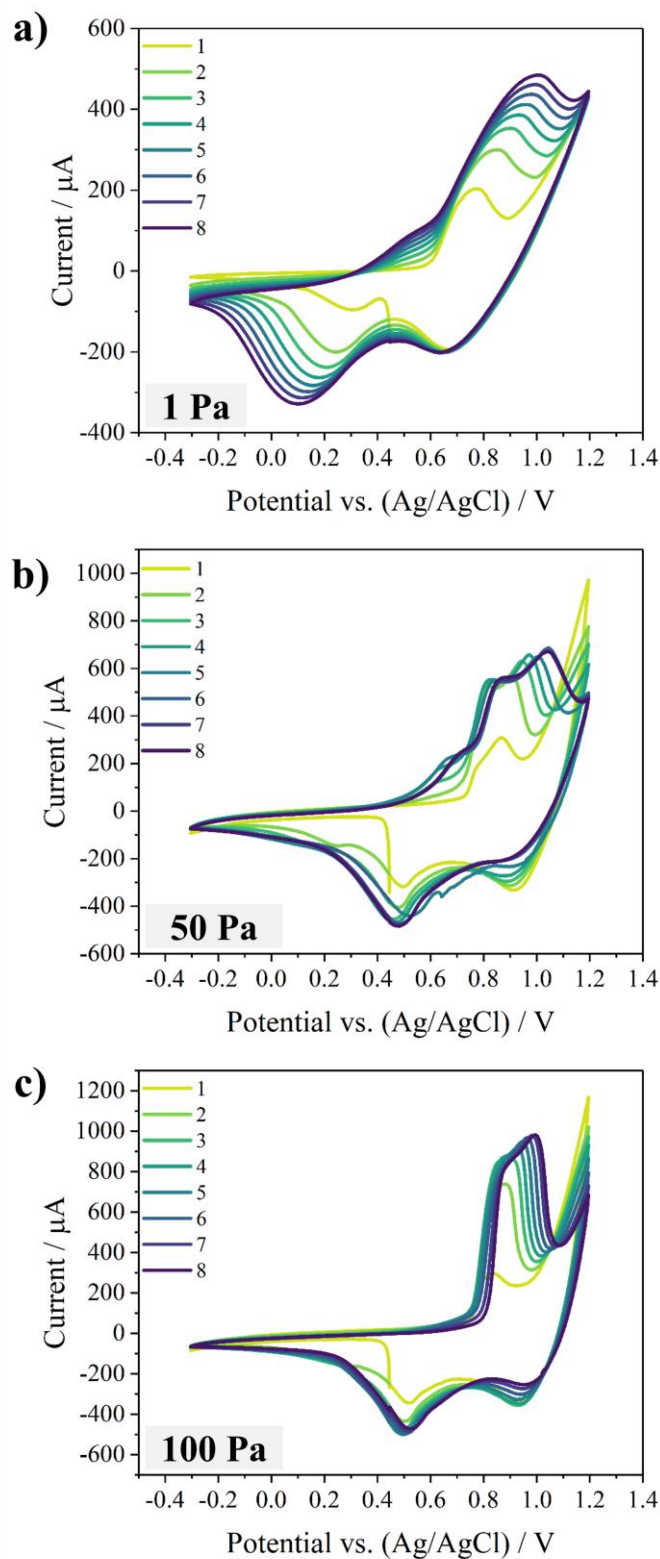


Fig. 9. CV curves at a scan rate of 25 mV s^{-1} of the ZMO films deposited at (a) 1, (b) 50, and (c) 100 Pa of O_2 , and crystallized in air at $500 \text{ }^\circ\text{C}$, 2h.

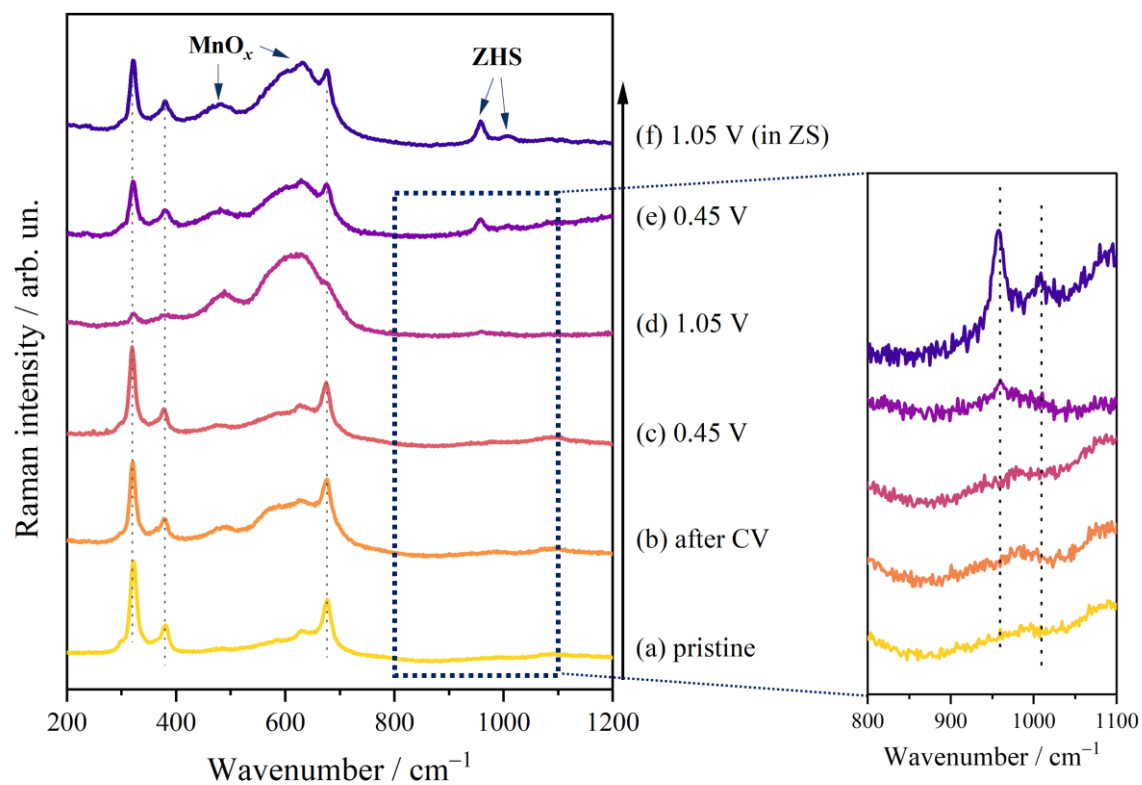


Fig. 10. Evolution of the quasi-*in situ* Raman spectra of a ZMO film (grown at 100 Pa of O_2 and annealed at 500 $^\circ\text{C}$, 2h) during sequential electrochemical measurements. In the inset, the spectral region between 800 and 1100 cm^{-1} is highlighted. Curves (a–e) were acquired after electrochemical polarization in ZMS electrolyte, while curve (f) was acquired after polarization in ZS electrolyte.

1
2
3
4
5
6
7
8
9
10
11
12
13
14
15
16
17
18
19
20
21
22
23
24
25
26
27
28
29
30
31
32
33
34
35
36
37
38
39
40
41
42
43
44
45
46
47
48
49
50
51
52
53
54
55
56
57
58
59
60
61
62
63
64
65

Nanostructured $Zn_xMn_{3-x}O_4$ thin films by pulsed laser deposition: a spectroscopic and electrochemical study towards the application in aqueous Zn-ion batteries

Andrea Macrelli^{a,*}, Marco Olivieri^a, Alessio Lamperti^b, Valeria Russo^{a,c}, Benedetto Bozzini^d,
Marco Menegazzo^e, Gianlorenzo Bussetti^e, Carlo S. Casari^{a,c}, Andrea Li Bassi^{a,c}

^a Micro and Nanostructured Materials Lab (NanoLab), Department of Energy, Politecnico di Milano, Via G. Ponzio 34/3, 20133 Milano, Italy;

^b Institute for Microelectronics and Microsystems (IMM), Consiglio Nazionale delle Ricerche (CNR), Unit of Agrate Brianza, Via C. Olivetti 2, 20864 Agrate Brianza (MB), Italy;

^c Center for Nano Science and Technology (CNST), Istituto Italiano di Tecnologia (IIT), Via G. Pascoli 70/3, 20133 Milano, Italy;

^d Battery Materials Engineering Laboratory (BMEL), Department of Energy, Politecnico di Milano, Via G. La Masa 34, 20156 Milano, Italy;

^e Solid Liquid Interface Nano-Microscopy and Spectroscopy (SoLINano- Σ) lab, Department of Physics, Politecnico di Milano, Piazza Leonardo da Vinci 32, 20133 Milano, Italy.

* Corresponding author, andrea.macrelli@polimi.it

Abstract

1
2
3 Aqueous Zn-ion batteries (AZIBs) represent a safe and sustainable technology among the post-
4
5 lithium systems, though the poor understanding of the material behaviour at the cathode prevents
6
7 the full development of efficient AZIBs. ZnMn_2O_4 (ZMO) has been considered one of the cathode
8
9 candidates owing to its analogy to the well-established LiMn_2O_4 cathode for lithium-ion batteries,
10
11 however its electrochemical mechanism in the presence of Zn ions in aqueous environment is
12
13 unclear and still debated. In this work, we synthesised nanostructured ZMO thin films by Pulsed
14
15 Laser Deposition (PLD) and we evaluated, through extensive characterization by microscopic,
16
17 spectroscopic, and diffraction techniques, how the deposition and annealing conditions affect the
18
19 film properties. The self-supported nature and the high degree of control down to the nanoscale
20
21 make a thin film an ideal model system to study the electrochemistry of the material in aqueous
22
23 solution and to emphasize the impact of the film properties on its electrochemical response. We
24
25 highlighted the crucial role of the oxygen pressure in the modulation of the film porosity and the
26
27 combined effect of deposition pressure and annealing temperature to produce a film with tailored
28
29 properties in terms of morphology, crystallinity, and Zn stoichiometry. A complex redox
30
31 mechanism involving multiple concurrent reactions and the formation of zinc hydroxide sulphate
32
33 hydrate (ZHS) was reported, as well as the influence of the film porosity on the voltametric
34
35 behaviour of the film at higher scan rate. Our results confirm the intricate electrochemical
36
37 mechanism of the ZMO material, which does not merely involve the Zn^{2+} insertion/extraction but
38
39 also the crucial participation of Mn^{2+} from the electrolyte, and pave the way for the nanoscale
40
41 design of engineered ZMO-based electrodes.
42
43
44
45
46
47
48
49
50
51
52
53
54

Keywords

55
56
57
58 Pulsed laser deposition, zinc-ion batteries, nanostructured cathode materials, ZnMn_2O_4 thin films.
59
60
61
62
63
64
65

1. Introduction

Rechargeable aqueous zinc-ion batteries (AZIBs) operating with a slightly acidic aqueous electrolyte and exploiting divalent Zn ions as charge carriers are a promising class of post-lithium next-generation batteries [1–3]. This type of secondary battery represents the evolution of primary alkaline zinc-ion batteries [4] and may be competitive against traditional lithium-ion batteries (LIBs) [5,6]. Indeed, zinc metal – notwithstanding shape-change and passivation issues that still have to be definitely sorted out [7–10] – can be effectively implemented as the anode and safely coupled with an aqueous medium, while lithium metal exhibits worse instability issues, combined with pyrophoricity [11]. Zinc metal is highly desirable due to its high theoretical gravimetric and volumetric specific capacities (820 mAh g⁻¹ and 5850 mAh cm⁻³, respectively), a redox potential of –0.76 V vs. SHE, and it can be produced and recycled using established processes [5]. Concerning the electrolyte, an aqueous medium is intrinsically safer and exhibits superior ionic conductivity compared to the flammable organic liquids traditionally employed in the state-of-the-art LIBs [1,5]. Nevertheless, the bottleneck to the development of efficient rechargeable AZIBs is the cathode. A few material candidates are available to reversibly sustain several electrochemical cycles involving a divalent cation, which is also responsible for the sluggish cathodic kinetics and early capacity fade [5,12–14]. In addition, the electrochemical mechanism is rather complex and encompasses multiple steps that may result in irreversible phase changes [1]. Among the proposed materials, manganese oxides [15–21], vanadium oxides [21,22], vanadium phosphates [1,23], metal vanadates [1,23], Prussian blue analogues (PBAs) [24], and some organic redox-active compounds [25,26] have been considered. Manganese oxides are particularly interesting, thanks to the abundant and low-toxicity nature of Mn, which is available in various oxidation states (from +2 to +7) leading to several oxide phases and structures [1]. In previous works, MnO [27,28], Mn₃O₄ [29–32], Mn₂O₃ [33–35], amorphous MnO_x [36,37], and MnO₂ polymorphs (α [38,39], β [18,40], γ [16,19], δ [41,42], ϵ [43], λ [44], and todorokite [45]) were tested as potential cathode materials for AZIBs. Another

1 alternative is zinc manganite, indicated by the general formula $Zn_xMn_{3-x}O_4$ [46–48], whose main
2 representative is $ZnMn_2O_4$ (ZMO), also known as hetaerolite. Zinc manganites are a family of
3
4 normal spinel oxides in which the cooperative Jahn-Teller distorted Mn^{3+} cations lead to a
5
6 tetragonal distortion of the overall crystal (which belongs to the I_{41}/amd space group) [47–49]. The
7
8 ideal spinel framework of ZMO, bearing a theoretical specific capacity of 224 mAh g^{-1} [50], is
9
10 reported to be unsuitable for the reversible insertion/extraction of Zn ions [51,52]; however, proper
11
12 nanostructuring, doping, introduction of stoichiometric defects, compositing with other materials,
13
14 and exploitation of reaction mechanisms different from mere Zn^{2+} insertion/extraction may make
15
16 this material an interesting candidate for AZIBs [53]. For example, N. Zhang *et al.* fabricated non-
17
18 stoichiometric $ZnMn_2O_4$, in which the presence of abundant Mn vacancies promoted the Zn^{2+}
19
20 insertion, thanks to a lower electrostatic repulsion between the host cations and the divalent charge
21
22 carriers [51]. In a similar approach, H. Zhang *et al.* introduced oxygen defects to tailor the
23
24 electronic conductivity, the ion diffusion kinetics, and the energy barrier for ion mobility [54],
25
26 while Lee *et al.* prepared Zn-rich manganite microspheres, with nominal stoichiometry
27
28 $Zn_{1.67}Mn_{1.33}O_4$ [55]. Interestingly, Wu *et al.* used a low-temperature synthesis to prevent the
29
30 structural water from being removed from the lattice, which had a beneficial effect on the Zn^{2+}
31
32 insertion and interfacial resistance [56]. Nanostructuring and compositing with various types of
33
34 conductive carbon nanostructures are other effective approaches to improve the electrochemical
35
36 performances and the structural stability of ZMO [57–65], as well as elemental doping. For
37
38 example, Baby *et al.* reported the improved performances of Co-substituted ZMO ($ZnMnCoO_4$,
39
40 ZMCO) [50], Tao *et al.* highlighted the positive effect of Ni and Co co-substitution to suppress the
41
42 Jahn-Teller distortion [66], Cai *et al.* investigated the impact of Al^{3+} substitution in Zn^{2+} sites [67],
43
44 and Shao *et al.* controlled the formation of oxygen defects in the ZMO lattice by double-doping
45
46 with K and Fe [68]. Finally, synergistic electrochemical effects could be achieved by compositing
47
48 ZMO with Mn_2O_3 [69–71] or Ti-MXenes [72]. In general, ZMO can be regarded as the Zn-
49
50 analogue of $LiMn_2O_4$ and suffers from the same drawbacks as manganese oxides cathodes, i.e.,
51
52
53
54
55
56
57
58
59
60
61
62
63
64
65

1 poor electronic conductivity, structural instability, poor rate performance, irreversible phase
2 transformations, and Mn dissolution during cycles [1,5,64]. In addition, the electrochemical
3 mechanism of ZMO-based materials in the presence of a Zn^{2+} - and Mn^{2+} -containing electrolyte is
4 still unclear, and several mechanisms have been reported to occur and/or to coexist, such as: Zn^{2+}
5 insertion/extraction [51,64], H^+ insertion/extraction [54,62], Zn^{2+}/H^+ co-insertion accompanied by
6 the formation of zinc hydroxide sulphate hydrate (ZHS) [56,65,73,74], and reversible
7 deposition/dissolution of MnO_x from the electrolyte [75].
8

9
10
11
12
13
14
15
16
17 Herein, we report on the synthesis of ZMO thin films by Pulsed Laser Deposition (PLD), a
18 technique that, to the best of our knowledge, has never been employed to grow ZMO-based
19 materials. A thin film can be used as a model system to study the electrochemical behaviour of the
20 pure material; indeed, a film offers unique advantages for materials-science investigations,
21 including: improved diffusion kinetics for ions and electrons, possibility to investigate novel
22 materials and structures, and self-supported nature, deriving from the absence of polymeric binders
23 and conductive additives [76]. In addition, beyond fundamental studies, thin films electrodes can be
24 directly implemented in real-life thin-film microbatteries [77,78]. PLD is a highly versatile physical
25 technique that allows the deposition of practically any material and the growth of nanostructured
26 thin films whose properties can be easily tuned in terms of morphology, porosity, stoichiometry,
27 structure, crystallinity, and phase by controlling a few deposition parameters [79,80]. In this work,
28 ZMO thin films fabricated by PLD are fully characterized in terms of compositional, structural, and
29 optical properties, and then employed in half-cells to assess their electrochemical behaviour and
30 material modifications. Based on the approach previously developed in [81], electrochemical
31 measurements on ZMO thin films in aqueous electrolyte are complemented by SEM and Raman
32 studies.
33
34
35
36
37
38
39
40
41
42
43
44
45
46
47
48
49
50
51
52
53
54
55
56
57
58
59
60
61
62
63
64
65

2. Experimental

2.1. Synthesis of thin films

ZMO thin films were synthesized by PLD in a stainless-steel vacuum chamber, equipped with a primary scroll pump and a turbomolecular pump, connected in series, able to evacuate the chamber down to a base pressure of $1-4 \times 10^{-3}$ Pa. Ablation was performed at room temperature using a frequency-doubled Nd:YAG laser source, in particular the 532 nm second harmonic, with 5–7 ns laser pulses and a repetition rate of 10 Hz. The laser pulses struck the target at an incidence angle of 45° and with an elliptical spot whose size was fixed at $\sim 6 \text{ mm}^2$ by properly focusing the laser pulses. The resulting laser fluence on the target was varied in the range $2-6 \text{ J cm}^{-2}$ by adjusting the pulse energy. The target was a $\text{Mn}_2\text{O}_3:\text{ZnO}$ (1:1 mol%) vacuum hot-pressed pellet (99.99%, Testbourne B.V.), mounted on a support able to rotate and translate during deposition to ensure a uniform ablation. The chamber was also equipped with a quartz crystal microbalance (QCM) to estimate the deposited mass and consequently the film density. Depositions were carried out both in vacuum and in O_2 gas (Sapio, 5.0 purity), whose pressure was tuned by mass flow controllers at 1, 10, 30, 50, 70, 100, and 150 Pa. The substrate was placed on a rotating holder at constant distance from the target of 5 cm. Silicon $\langle 100 \rangle$ (Siegert Wafer), soda-lime glass slides (Marienfeld), and F-doped SnO_2 (FTO)-coated soda-lime glass slides (Sigma-Aldrich) were used as the substrates. Glass-based substrates were cleaned with isopropyl alcohol in ultrasonic bath before the insertion into the PLD chamber and dried with compressed air. The deposition time was selected according to the deposition rate and depending on the expected film thickness. Some samples were annealed in air using a Lenton Muffle furnace (ECF type) at different temperatures (400–800 °C).

2.2. Characterization

A field emission scanning electron microscope (FE-SEM, Zeiss SUPRA 40) was used to acquire top view and cross-sectional morphological images of thin films deposited on Si and FTO-coated glass. The film composition was evaluated by energy-dispersive X-ray spectroscopy (EDXS) using

1 a Peltier-cooled silicon drift detector (SDD) within the SEM microscope (Oxford Instruments) and
2 elaborated using the AZtec EDS software. Raman spectroscopy was used to gain information about
3 the structure and the crystallinity of the films. A Renishaw InVia micro-Raman spectrometer
4 equipped with a diode-pumped solid-state laser emitting 532 nm excitation radiation was used. The
5 laser was focused on the sample using a 50× objective and the laser power was selected so as to
6 avoid any photo-induced damage to the sample (typical values were 0.7–1.75 mW). For the quasi-*in*
7 *situ* Raman characterization after the electrochemical measurements, a Confotec NR500
8 spectrometer by Sol instruments was used, equipped with a solid-state laser ($\lambda=532$ nm, laser power
9 on sample ~ 0.6 mW) and a 40× objective. X-ray diffraction (XRD) was employed to investigate the
10 crystalline structure of the films. A HRD3000 diffractometer (Ital Structures, Riva del Garda, Italy)
11 operating with monochromated Cu K α radiation ($\lambda=0.1541$ nm) and equipped with a curved
12 position-sensitive multichannel gas-filled detector (2θ range 0–120°, resolution 0.029°, Inel CPS-
13 120) was used. The XRD measurements were carried out in grazing incidence configuration
14 (GIXRD) with an incidence angle of $\omega=2^\circ$. The optical properties of films deposited on soda-lime
15 and FTO-coated glass were probed by direct transmittance in the range 190–1100 nm using a
16 Shimadzu UV-1800 spectrophotometer, and by transmittance and reflectance in the range 250–2000
17 nm using a PerkinElmer Lambda 1050 spectrophotometer equipped with a 150 mm-integrating
18 sphere.

2.3. *Electrochemical characterization*

24 The electrochemical behaviour of as-deposited and annealed ZMO films on conductive FTO-coated
25 glass slides was investigated in a three-electrode configuration and using a home-made
26 electrochemical cell. Briefly, the sample was placed on top of a stainless-steel support and
27 electrically insulated by a polymeric gel. Electrical contacts were made by attaching a Cu wire to
28 the exposed FTO layer with Cu tape. A PTFE case equipped with a VITON O-ring was directly
29 pressed on the sample and fixed by screws to the support, then it was filled with the liquid

1 electrolyte (total volume ~1 mL). The area of the film exposed to the electrolyte was ~0.4 cm². Two
2 platinum wires were inserted into the cell, one turning around the whole cell and operating as the
3 counter electrode, and one acting as a quasi-reference (Pt-QRef) electrode. The potential shift of the
4 Pt-QRef electrode with respect to the Ag/AgCl (KCl 3.5 M) reference electrode was experimentally
5 determined in a two-electrode cell to be +0.445 V, with stability within a few mV in the
6 investigated electrolytes. All potentials reported have been referenced to the Ag/AgCl scale. ZMO
7 samples were tested in aqueous electrolytes containing 2 M ZnSO₄ (ZS), 0.1 M MnSO₄ (MS), or 2
8 M ZnSO₄ + 0.1 M MnSO₄ (ZMS), prepared in deionized water from zinc sulphate heptahydrate
9 (ZnSO₄ · 7H₂O, ≥ 99.0%) and manganese sulphate monohydrate (MnSO₄ · H₂O, ≥ 98%), both
10 purchased from Sigma-Aldrich. Cyclic voltammetry (CV) and other electrochemical measurements
11 were performed using a PalmSens4 potentiostat/galvanostat/impedance analyser.
12
13
14
15
16
17
18
19
20
21
22
23
24
25
26
27
28
29

30 **3. Results and discussion**

31 *3.1. Optimization of PLD parameters*

32
33
34
35
36
37
38
39
40
41
42
43
44
45
46
47
48
49
50
51
52
53
54
55
56
57
58
59
60
61
62
63
64
65
PLD allows one to easily adjust the deposition parameters, especially the chamber pressure, the type
of gas, the laser fluence, and the target-substrate distance, in order to fabricate a thin film with
tuneable and optimizable properties and performances. ZMO thin films were grown in vacuum and
at different O₂ pressures (1–150 Pa); the gas atmosphere affects the dynamics of plasma formation,
cluster nucleation, and deposition [80], thus it mainly affects the resulting film morphology. SEM
cross-sectional images of as-deposited ZMO films on Si as a function of the O₂ deposition pressure
(laser fluence ~3.7 J cm⁻², deposition time = 15 min) are reported in Fig. 1a. Increasing the O₂
pressure from vacuum to 150 Pa, the film morphology changes from a compact columnar structure
to a highly porous tree-like structure, along with a progressive increase of film porosity and surface
roughness. At high oxygen pressures (100 and 150 Pa), the dense columnar structure is replaced by
porous nanotrees. The increase of film porosity is accompanied by a sharp decrease in density

1 (below $\sim 1 \text{ g cm}^{-3}$ for samples deposited at or above 50 Pa, as estimated from QCM measurements
2 coupled with SEM images; for comparison, the density of bulk crystalline ZMO is 5.254 g cm^{-3}
3 [82]) and by a corresponding increase in surface area and film thickness at fixed deposition time.
4
5 The morphology evolution as a function of the background gas pressure described above is typical
6
7 of PLD-grown oxides and nitrides thin films [80,83–87]. The laser fluence (i.e., the laser energy per
8
9 unit area striking the target) has a less evident effect on film morphology. In addition to an expected
10
11 increase of the deposition rate at constant O_2 pressure, higher fluences lead to more compact films
12
13 and, especially at high O_2 pressures ($\geq 50 \text{ Pa}$), cause the detachment of the growing film from the
14
15 substrate, the film breakup, and the presence of a larger number of defects (Fig. S1). As a result, a
16
17 reasonable fluence of $\sim 3.7 \text{ J cm}^{-2}$, corresponding to energies of $\sim 225 \text{ mJ pulse}^{-1}$, was selected for
18
19 subsequent depositions as a compromise between deposition rate and film quality. Typical
20
21 deposition rates at this fluence range from some tens of nm min^{-1} in vacuum/low O_2 pressure up to
22
23 hundreds of nm min^{-1} above 50 Pa. O_2 background atmosphere also affects the film stoichiometry,
24
25 which can be modified with respect to the nominal composition of the target by depositing in a
26
27 reactive gas. As depicted in Fig. 1b, where EDX elemental analysis is reported, our as-deposited
28
29 films are enriched with oxygen as the O_2 deposition pressure increases up to $\sim 30 \text{ Pa}$, with the O
30
31 atomic content in the films rising from 48% (vacuum) to $>60\%$ (30 Pa). This increase is
32
33 accompanied by a decrease in the Mn atomic content (from 38% to 27%), while the Zn atomic
34
35 content shows much less variability (between 11% and 14%) in the whole O_2 pressure range.
36
37
38
39
40
41
42
43
44
45
46

47 *[Figure 1 about here]*
48
49

50 Structural information about ZMO films was gained by Raman spectroscopy. Raman spectra of all
51
52 as-deposited films at any O_2 pressure and laser fluence show a weak and broad band centred around
53
54 600 cm^{-1} and extending in the range $450\text{--}750 \text{ cm}^{-1}$, indicating an amorphous nature of the film (Fig.
55
56 2a, black spectrum).
57
58
59

60 *[Figure 2 about here]*
61
62
63
64
65

3.2. Thin films annealing

In order to promote the film crystallization, as-deposited ZMO films were subjected to thermal treatments in air in the temperature range 400–800 °C. Film crystallization to the expected spinel phase [46,49,88,89] was achieved at any temperature above 450 °C, as confirmed by the Raman spectrum of the annealed film of Fig. 2a, where sharp peaks are observed. Three main peaks are found at 325, 385, and 679 cm^{-1} (the latter mode can be assigned to A_{1g} symmetry [49]), while additional shoulders and weak features are observed also at 302, 373, 475, 587, and 652 cm^{-1} (Fig. S2), all well matching with the reported Raman bands of ZnMn_2O_4 [46,49]. No signals from secondary phases were detected. In Fig. 2b, the EDX elemental analysis of ZMO films deposited at different O_2 pressures and annealed in air at 600 °C for 3h are reported. Although EDX suffers from low accuracy in the quantification of light elements, which entails uncertainties in the absolute values especially in the absence of calibration samples, the overall trends of the atomic contents with respect to O_2 pressure are still relevant. After the thermal treatment, the atomic content of Zn and Mn increases compared to as-deposited films, while the O atomic content decreases (at least for samples deposited at ≥ 10 Pa O_2). None of the elements, however, matches the atomic percentages of stoichiometric ZnMn_2O_4 , indicated by grey dashed lines in Fig. 2b. All the films contain a lower amount of oxygen (52–55%) with respect to the theoretical value of ~57%, and a higher amount of Mn, which may indicate the presence of Mn ions with a lower oxidation state (i.e., Mn^{2+}), and the possible localized formation of spinel hausmannite Mn_3O_4 , isostructural to ZnMn_2O_4 [49,90,91].

[Figure 3 about here]

SEM images of ZMO films after annealing are reported in Fig. 3a (cross-sections) and in Fig. S3 (top-views). The morphology is completely different from that of as-deposited films (Fig. 1a). Films are polycrystalline, with morphological grains ranging from hundreds of nm to ~50 nm as the O_2 deposition pressure increases. In addition, the columnar and compact structure of films deposited in vacuum and 10 Pa is replaced by large faceted crystalline grains and by some voids and cavities

(Fig. 3a and Fig. S3a-c), qualitatively indicating a higher degree of porosity compared to as-deposited films, also for low O₂ deposition pressures. For films deposited at 50 and 100 Pa, small crystalline grains (50-100 nm) assemble into vertical structures resembling the original nanotrees. The Raman spectra of annealed films deposited in vacuum and at 1, 10, 50, and 100 Pa of O₂ are reported in Fig. 3b and were analysed using Lorentzian fittings. The three main Raman bands of spinel ZMO (here labelled as peak I, II, and III, respectively) exhibit a blueshift as the deposition pressure increases (Fig. 3c and Fig. S4a-b), which is more relevant for the high-frequency A_{1g} mode (peak III) [49]. Indeed, peak III shifts from 673.8 cm⁻¹ to 680.3 cm⁻¹ as the O₂ deposition pressure is increased from vacuum to 150 Pa. In addition, the intensity ratio between peak I and peak III is reversed with increasing O₂ pressure: indeed, the A_{1g} peak (peak III) is the most intense in the Raman spectra of crystalline samples deposited in vacuum and at 1 Pa, whereas peak I becomes dominant at or above 10 Pa (Fig. 3c). Such variations in peak position and relative intensity may be ascribed to the effect of crystallite size only [92], however similar trends are reported also by Nádherný *et al.* [46] and correlated to the amount of Zn in the manganite structure, i.e., to the stoichiometric *x* value in Zn_{*x*}Mn_{3-*x*}O₄. Since the atomic contents of Mn and Zn in the films after crystallization are not constant (Fig. 2b) and no secondary phases are detected by Raman spectroscopy and SEM imaging, the modifications observed in the Raman spectra of Fig. 3b might be attributed to slight changes in the relative contents of metallic elements in the overall manganite structure. The differences observed in peak position and relative intensity ratios with increasing O₂ deposition pressure are not associated with a clear trend in peak width (Fig. S4c). Compared to the Raman spectra of spinel Mn₃O₄ reported in [92], which correlates the progressive redshift and broadening of the main A_{1g} peak with decreasing crystallite size from >100 nm to 7 nm, our spectra exhibit a general blueshift and no specific peak broadening or narrowing as the O₂ pressure increases. This may indicate that the crystal size does not play the major role in affecting the Raman spectra of annealed ZMO thin films. In addition, annealing in air of selected samples at different temperatures (500, 600, 700, and 800 °C) demonstrated that the Raman spectra are not affected by

1 the increase in temperature, even if the ZMO crystalline grains get bigger as the annealing
2 temperature increases (Fig. S5 and Fig. S6a). In this case, a gradual decrease of peaks width
3
4 confirms the improvement of crystalline quality with increasing annealing temperature (Fig. S6b).
5
6 Film crystallization is further confirmed by GIXRD measurements. The X-ray diffraction patterns
7
8 of ZMO films produced in vacuum and at 1, 10, 50, and 100 Pa of O₂ are reported in Fig. 4, along
9
10 with the powder reference pattern of tetragonal spinel hetaerolite ZnMn₂O₄ (Card No: 6990,
11
12 WWW-MINCRYST [93,94]). Good agreement with the reference pattern is observed for ZMO
13
14 films produced at 50 and 100 Pa, which exhibit the most intense (211) reflection at 2θ~36.40° and
15
16 consistent intensity ratios. The X-ray data at 10 Pa are coherent as well, even though the (103)
17
18 reflection is absent and some discrepancies affect the relative intensity ratios, especially the (112)
19
20 vs. (200) and the (321) vs. (224). In contrast, the main reflection in the GIXRD pattern of the ZMO
21
22 film produced at 1 Pa is the (103) at 2θ~32.67°, and the (200), (220) and (400) reflections are weak
23
24 or totally suppressed. Finally, the X-ray diffraction pattern of the ZMO sample produced in vacuum
25
26 exhibits one sharp and narrow peak at 2θ~17.87°, corresponding to the (101) reflection, while most
27
28 of other reflections are suppressed, except for the (312), (224), and (400). The XRD results reveal a
29
30 different preferential crystalline orientation within ZMO films produced in vacuum and at 1 Pa O₂
31
32 and suggest that the O₂ deposition pressure affects not only the short-range order of the material (as
33
34 confirmed by the modifications in the Raman spectra, Fig. 3b-c), but also the long-range crystalline
35
36 texture.
37
38
39
40
41
42
43
44

45
46
47 *[Figure 4 about here]*
48
49

50 Quantitative analysis was carried out using the Williamson-Hall (WH) method [95,96], which
51
52 allows the estimation of the average size of crystal domains and of the lattice micro-strain through
53
54 the broadening of the XRD peaks (Fig. S7a-e). As expected, the domain size is maximum in the
55
56 ZMO film produced in vacuum (τ~63 nm) and it decreases down to τ~57 nm and τ~27 nm for films
57
58 deposited at 1 and 10 Pa, respectively; it remains almost constant in the film produced at 50 Pa
59
60
61
62
63
64
65

1
2
3
4
5
6
7
8
9
10
11
12
13
14
15
16
17
18
19
20
21
22
23
24
25
26
27
28
29
30
31
32
33
34
35
36
37
38
39
40
41
42
43
44
45
46
47
48
49
50
51
52
53
54
55
56
57
58
59
60
61
62
63
64
65
($\tau \sim 29$ nm), but it raises to $\tau \sim 38$ nm at 100 Pa (Fig. S7f). The lattice micro-strain is found to be positive in all the films, i.e., indicating the presence of a tensile stress state, and it is maximum in the film deposited at 1 Pa (Fig. S7f). Raman spectroscopy and GIXRD results clearly indicate that the O₂ deposition pressure is a key parameter affecting the structural ordering of the ZMO thin films at both the short/medium range and the long range. In particular, GIXRD measurements highlighted the evolution of the preferential crystal orientation, the variation of the crystal size, and the occurrence of lattice micro-strains, while the modifications of the Raman spectra may be correlated to the Zn stoichiometry according to [46]. However, additional effects may contribute to the overall shift and broadening of the ZMO Raman peaks, e.g., the residual stress state, the presence of traces of secondary phases, the oxygen deficiency, and the crystal size, therefore the trends observed in Fig. 3b-c and Fig. S4 may result from multiple and interrelated causes.

3.3. *Optical properties of annealed films*

ZMO thin films were deposited on glass and FTO-coated glass slides, with the purpose of carrying out optical measurements. The deposition time, at any value of O₂ pressure and constant fluence of 3.7 J cm⁻², was adjusted to achieve a film thickness in the range 500–600 nm, depending on the deposition rate previously evaluated on samples deposited on Si in similar conditions. Before annealing, ZMO thin films exhibit a dark reddish colour, which turns orange/yellow after thermal treatment in air (Fig. S8a). Since the thermal stability of the glass support is limited to ~ 550 °C, annealing of ZMO films on bare glass and FTO-coated glass was performed at 500 °C for 2h. This temperature allows good film crystallization, as evaluated by Raman spectroscopy and SEM analysis (Fig. S8b-c). In Fig. 5, UV-Vis transmittance, reflectance, and absorption curves in the wavelength range 300–2000 nm for ZMO samples deposited on soda-lime glass at 1, 10, 50, and 100 Pa of O₂, and crystallized in air at 500 °C for 2h, are reported. Transmittance and reflectance

1 data of Fig. 5a-b were collected in a spectrophotometer equipped with the integrating sphere and
2 account for both direct and diffuse contributions. Absorption data are estimated by the relation:
3

$$4 \quad A(\lambda, \%) \cong 100 - T(\lambda, \%) - R(\lambda, \%)$$

5
6
7
8 Transmittance and absorption curves (Fig. 5a and Fig. 5c) exhibit a small blueshift as the deposition
9 pressure increases. In addition, the number of interference fringes in the transmittance curves
10 decreases with increasing O₂ pressure as well. Similarly, the increase of surface roughness leads to
11 less defined fringes as the O₂ pressure increases. Absorption curves of Fig. 5c feature extended sub-
12 bandgap optical absorption in the range 600–750 nm, which may indicate the presence of defect
13 states in the mid-gap region of the material [89]. In Fig. 5d, absorption curves are reported as a
14 function of photon energy, in the range 0.5–4.5 eV, for comparison.
15
16
17
18
19
20
21
22
23
24
25

26 *[Figure 5 about here]*

27
28
29 Similar results are obtained by measuring the direct transmittance of ZMO films deposited on FTO-
30 coated glass at the same deposition conditions in terms of laser fluence and O₂ pressure as on the
31 bare glass slides (Fig. S9), with average thickness ~500–600 nm. The slight blueshift of the
32 transmittance curves observed in Fig. 5a as the O₂ pressure increases is still present, even if some
33 deviations are observed, e.g., for the film deposited at 50 Pa. Such variations may be ascribed to the
34 effect of the substrate on film morphology or, more likely, to the contribution of the diffuse
35 transmittance, which is lost during measurements of direct transmittance and could be relevant for
36 porous samples.
37
38
39
40
41
42
43
44
45
46
47
48
49
50
51
52

53 *3.4. Electrochemical properties of annealed films*

54
55
56 The schematic illustration for the preparation of crystalline ZMO thin films on an FTO-coated glass
57 substrate for electrochemical characterization is reported in Fig. 6. All the films were grown by
58 PLD in O₂ atmosphere with tuneable morphology and average thickness in the range 500–600 nm,
59
60
61
62
63
64
65

1 and then they were thermally annealed in air at 500 °C for 2h to achieve the proper spinel phase
2 without damaging the glass substrate.
3

4
5 [Figure 6 about here]
6

7
8 The CV profiles of the ZMO thin film grown at 50 Pa of O₂ are reported in Fig. 7. CV was
9 performed in ZMS electrolyte at a scan rate of 1 mV s⁻¹. We have selected this electrolyte because
10 it is the standard for AZIB studies: it is worth noting that differences in composition among MS,
11 ZS, and ZMS electrolytes have a specific impact on the structural evolution upon cycling of MnO_x-
12 based electrodes [81]. CV cycling was carried out in a potential range spanning Mn reactivity
13 between reduction to Mn²⁺ and oxidation to Mn⁴⁺. The complex voltammetric patterns,
14 corresponding to combined Mn-redox and phase-transformation/film-formation, can be interpreted
15 in the methodological framework set in [81]. Cycling was started from 0.1 V with an anodic-going
16 scan, that exhibits a weak anodic peak at ~0.8 V and a current onset at ~0.9 V. These processes, in
17 principle, can correspond to phase formation by oxidation of Mn²⁺ present in the electrolyte and
18 oxidation of Mn³⁺ present in ZMO, converting to a Mn⁴⁺-containing phase. The first cycle is
19 markedly different from the following ones, indicating an activation/transformation process of the
20 film, which is frequently reported for Mn- and ZMO-based electrode materials [59,63]. In the
21 anodic branch, starting from the second cycle, the two features observed in the first anodic-going
22 scan are notably activated by the reduction processes observed in the cathodic-going scan –
23 discussed below – and develop into a couple of oxidation peaks. These peaks are initially centred at
24 0.75 V and 0.86 V and exhibit a progressive shape change and the tendency to shift towards higher
25 potential values, as the number of cycles increases. These modifications of the anodic CV features
26 can be ascribed to a progressive phase transformation, as detailed below. As far as the cathodic
27 branch is concerned, a couple of reduction peaks can be observed, that exhibits a notable change
28 between the first and the subsequent cycles. Similarly to the anodic counterpart, prolonged cycling
29 leads to progressive peak shift in the anodic direction in the ranges 0.34–0.4 V and 0.49–0.55 V,
30
31
32
33
34
35
36
37
38
39
40
41
42
43
44
45
46
47
48
49
50
51
52
53
54
55
56
57
58
59
60
61
62
63
64
65

1 respectively. Our CV curves agree with those reported in previous works and corresponding to
2 various ZMO-based nanostructures in the same electrolyte solution [60,69,75]. The assignment of
3 the redox peaks to a specific electrochemical process is not unique since multiple concurrent
4 processes may occur at the electrode-electrolyte interface, yielding very similar current responses,
5 and the scientific literature is not unanimous. During the anodic scan, the oxidation peaks could be
6 ascribed to both the extraction of Zn^{2+} from the host lattice, accompanied by the stepwise oxidation
7 of Mn^{3+} to Mn^{4+} , and to the electrodeposition of MnO_x interphases from Mn^{2+} species present in the
8 electrolyte, either because of its formulation or originating from the cathodic dissolution of the film
9 material. During the cathodic scan, these processes are reversed. Overall, cycling seems to lead to a
10 stable voltammetric pattern, featuring a couple of reversible redox processes involving a solid
11 electrode/electrolyte interface.
12
13
14
15
16
17
18
19
20
21
22
23
24
25
26

27 [Figure 7 about here]
28
29

30 In order to gain better insight into the nature of these electrochemical material transformations, we
31 resorted to *ex situ* structural and morphological characterization. After having completed the CV
32 cycling experiments of Fig. 7, the aged ZMO sample was extracted from the cell, immediately
33 rinsed in deionized water, and gently dried to remove any trace of soluble sulphates. In Fig. 8a, a
34 SEM cross-sectional image of the aged film at the end of the sixth cycle is depicted, revealing a
35 profound modification with respect to the morphology of the pristine film (not shown, but
36 reasonably comparable with the cross-section of Fig.3a). Specifically, a clear multi-layered
37 structure develops from the initial columnar and granular morphology: starting from the bottom part
38 of the image, the first layer resembles the structure of the original film, even if its thickness is
39 reduced (to ~300 nm) and the morphology is slightly changed (Fig. 8b), denoting some degree of
40 electrochemical activity. The second layer (thickness ~800–900 nm) consists of a porous, thick
41 deposit, which can be identified by Raman spectroscopy (Fig. 8c) as MnO_x [97], originating either
42 from the electrodeposition of Mn^{2+} in the electrolyte, or from the transformation of the ZMO film.
43
44
45
46
47
48
49
50
51
52
53
54
55
56
57
58
59
60
61
62
63
64
65

1
2
3
4
5
6
7
8
9
10
11
12
13
14
15
16
17
18
19
20
21
22
23
24
25
26
27
28
29
30
31
32
33
34
35
36
37
38
39
40
41
42
43
44
45
46
47
48
49
50
51
52
53
54
55
56
57
58
59
60
61
62
63
64
65

Finally, the third layer is constituted by thin, water-insoluble flakes. This peculiar flake-like morphology (Fig. 8a and Fig. S10a) suggests the precipitation of zinc hydroxide sulphate hydrate (ZHS) $Zn_4(OH)_6(SO_4) \cdot nH_2O$ phase, commonly reported in previous works as a by-product formed during the discharge of AZIBs in near-neutral aqueous electrolytes containing Zn sulphate [60,62,75,98]. The formation of ZHS is conventionally associated with proton insertion into the active film during the cathodic scan, leading to an increase of the pH of the electrolyte surrounding the film, and to the precipitation of this basic compound that acts as a buffer [98]. The presence of ZHS is confirmed by both Raman spectroscopy, i.e., the peaks at 969 and 1015 cm^{-1} [98] (Fig. 8c), and EDXS, which reveals the occurrence of sulphur in addition to Zn, Mn, and O (Fig. S10b).

[Figure 8 about here]

To highlight the effect of the film morphology on the electrochemical response of the material, additional CV measurements in ZMS electrolyte were carried out at a higher scan rate of 25 $mV s^{-1}$ – de-emphasizing diffusion-controlled processes with respect to phase-formation ones – on ZMO films grown at 1, 50, and 100 Pa of O_2 , corresponding to increasing porosity. The CV profiles are reported in Fig. 9, displaying the first eight cycles for each sample. It can be noticed that the shape of the CV curves differs significantly across the samples. Moreover, for a given sample, the CV responses at 1 and 25 $mV s^{-1}$ are different (e.g., compare Fig. 7 and Fig. 9b). Firstly, the redox peaks become more defined as the film porosity increases, i.e., moving from 1 to 100 Pa. This is an indication of a diffusion-based process, which is facilitated both at lower scan rate and in samples exhibiting shorter diffusion paths. Secondly, all the curves show a progressive separation of the peaks towards higher potentials (in absolute value) as the cycles proceed. This effect, that was less evident at 1 $mV s^{-1}$, owing to the lower currents involved, is due to the formation of a resistive layer during the electrochemical cycling, leading to increased polarization. This phenomenon is progressively less evident as the porosity increases, especially in the case of the most porous film

(Fig. 9c), the electrochemical response of which features sharper redox peaks and stabler cycle shapes compared to those of the less porous ones (Fig. 9a-b).

[Figure 9 about here]

After the CV test, the sample grown at 100 Pa of O₂ – which showed sharper and stabler redox peaks in the CV of Fig. 9c – was subjected to a series of constant potential measurements in ZMS electrolyte to promote the redox reactions and to evaluate the current response over time. At the same time, quasi-*in situ* Raman measurements were carried out to probe the sample structural evolution. The Raman results and the current vs. time profiles at selected potential values are summarized in Fig. 10 and Fig. S11, respectively. After the CV (curve b) the main ZMO features are still visible, however a broad band arises next to the A_{1g} peak and extends between 550 and 650 cm⁻¹. In addition, a broad peak starts to be visible at ~490 cm⁻¹. Both features indicate the formation of MnO_x during the CV cycles [64,97]. Cathodic polarization at 0.45 V for 1100 s partially restores the film to its initial conditions (curve c), reducing the intensity of the MnO_x bands: this behaviour is compatible with the incomplete dissolution of the MnO_x layer, which can also be accompanied by Zn²⁺ insertion in the MnO_x formed during the anodic branches of the CV run either from ZMO de-insertion or from oxidative electrodeposition of Mn²⁺ present in solution. Correspondingly, the cathodic current asymptotically approaches zero after 1100 s (Fig. S11a). The following anodic polarization at 1.05 V for 1800 s leads to a significant decrease in the intensity of ZMO Raman peaks, in conjunction with the uprise of the MnO_x band (curve d), which can be explained with both Zn²⁺ de-insertion from ZMO and electrodeposition from the electrolyte. Moreover, the resultant anodic current profile does not approach zero, but tends asymptotically to a current value of ~260 μA (Fig. S11b), suggesting an ongoing redox process. Finally, the Raman peaks of ZMO become clearly visible again after the second cathodic polarization at 0.45 V for 1500 s, even if the MnO_x features are still intense (curve e). The corresponding cathodic current profile approaches zero at the end of the measurement (Fig. S11c), indicating that the MnO_x phase

1 cannot be totally and reversibly reduced at 0.45 V. In addition, as reported in the inset of Fig. 10,
2 the peaks at 960 and 1008 cm^{-1} appear after the second cathodic polarization, revealing the
3 precipitation of the ZHS phase [98]. Interestingly, ZHS was not present immediately after the CV at
4 25 mV s^{-1} (as it was in the case of CVs at 1 mV s^{-1} , see Fig. 8) since its formation evidently
5 requires longer reaction times. The typical flake-like morphology of ZHS was also highlighted by
6 SEM (Fig. S11e-g). Interestingly, in the absence of electroactive Mn^{2+} in the electrolyte – i.e., using
7 the ZS electrolyte – the Raman spectrum does not appreciably change upon anodic polarization at
8 1.05 V (compare curves e and f) and the current vs. time profile differs significantly from that
9 observed when the same process is run in the ZMS electrolyte (compare Fig. S11b and Fig. S11d),
10 exhibiting no asymptotic current value and a rapid decrease to zero (the measurement was stopped
11 after 500 s). Notably, the high-frequency Raman peaks do not disappear, indicating no ZHS
12 dissolution at this potential value. This last test in the ZS electrolyte confirms that the main redox
13 process in the potential ranges investigated in this work involves the electrodeposition of MnO_x
14 species from Mn^{2+} dissolved in the electrolyte, possibly accompanied by the reversible
15 insertion/extraction of Zn^{2+} in these electrodeposited layers.
16
17
18
19
20
21
22
23
24
25
26
27
28
29
30
31
32
33
34
35
36

37 [Figure 10 about here]
38
39

40 Lastly, in order to better distinguish between phase transformation and formation processes, CV
41 measurements at 25 mV s^{-1} were performed also on bare FTO-coated glass substrates in the MS,
42 ZS, and ZMS electrolytes, as reported in Fig. S12. No electrochemical activity is obviously reported
43 in ZS electrolyte, due to the absence of redox-active species in the selected potential range. On the
44 other hand, redox peaks are observed in both MS and ZMS electrolytes, which could be ascribed to
45 the electrodeposition/dissolution of MnO_x on the surface from the Mn^{2+} in the electrolyte. The
46 noticeable difference in CV shape and intensity denotes the role of Zn^{2+} in the electrochemical
47 reactions, which may insert/de-insert into/from the electrodeposited MnO_x layer only in ZMS
48 electrolyte. Our results are closely similar to those reported by Soundharrajan *et al.*, which
49
50
51
52
53
54
55
56
57
58
59
60
61
62
63
64
65

1 unravelled the dominant role of Mn^{2+} in the electrolyte on the electrochemical mechanism of
2 $ZnMn_2O_4$ -based materials [75], and to those of [81], which highlights the impact on the
3
4 electrochemical response of MnO_x resulting from the presence of Zn^{2+} in the electrolyte.
5
6
7
8
9

10 4. Conclusions

11
12 In this work, we successfully synthesized ZMO thin films via PLD on different substrates. Using
13
14 complementary characterization techniques, including SEM, EDXS, Raman spectroscopy, XRD,
15
16 UV-Vis optical spectroscopy, we highlighted the effect of deposition (O_2 pressure, laser fluence)
17
18 and annealing (temperature, duration) parameters on the variation of film morphology, composition,
19
20 and crystallinity, which strongly affect the vibrational, structural, optical, and electrochemical
21
22 properties of the material. The O_2 deposition pressure results to be the most significant synthesis
23
24 parameter: by increasing the O_2 pressure from vacuum to 150 Pa, the ZMO film becomes more
25
26 porous and less dense and, after crystallization upon thermal treatment in air, the effect of
27
28 deposition pressure is still observable in the Raman features, the XRD crystal orientation, the
29
30 stoichiometry, and the optical absorption of the film. Since bulk ZMO was previously reported to
31
32 exhibit poor electrochemical activity in the presence of Zn^{2+} [51], a rationally designed ZMO
33
34 material in terms of nano-porosity (and hence density and surface area), crystal size and orientation,
35
36 phase purity, and Zn vs. Mn stoichiometry is supposed to demonstrate superior electrochemical
37
38 properties, resulting in improved performances when implemented in a real device. The CV tests
39
40 carried out on the crystallized films showed an electrochemical response consistent with current
41
42 knowledge of the electrochemistry of MnO_x -based materials, and emphasized a major impact of the
43
44 film synthesis conditions. In conjunction with *ex situ* characterization measurements on aged
45
46 samples and following the approach developed in [81], such CV measurements complemented by
47
48 microscopic and spectroscopic analyses highlight a complex redox behaviour in aqueous electrolyte
49
50 containing both Zn^{2+} and Mn^{2+} , which may involve multiple simultaneous processes such as Zn^{2+}
51
52
53
54
55
56
57
58
59
60
61
62
63
64
65

insertion/extraction, H⁺ insertion/extraction, ZHS precipitation/dissolution, and MnO_x deposition.

Further electrochemical studies, combined with *in situ* characterization and analytical techniques capable of jointly yielding structural and chemical-state information, such as XAFS, will be undertaken in the near future, to fully elucidate the electrochemical mechanisms of the different ZMO films – in particular disentangling insertion and surface phase formation processes – to optimize their structure in view of the achievement and stabilization of high-capacity performance in real-life AZIBs.

CRedit authorship contribution statement

Andrea Macrelli: Conceptualization, Methodology, Validation, Formal Analysis, Investigation, Visualization, Writing – Original Draft, Writing – Review & Editing. **Marco Olivieri:** Formal Analysis, Investigation. **Alessio Lamperti:** Methodology, Investigation, Resources, Writing – Review & Editing. **Valeria Russo:** Methodology, Supervision, Writing – Review & Editing. **Benedetto Bozzini:** Conceptualization, Methodology, Formal Analysis, Resources, Writing – Review & Editing, Supervision. **Marco Menegazzo:** Methodology, Resources. **Gianlorenzo Bussetti:** Methodology, Resources. **Carlo S. Casari:** Conceptualization, Writing – Review & Editing, Supervision. **Andrea Li Bassi:** Conceptualization, Writing – Review & Editing, Supervision.

Declaration of competing interest

The authors declare that they have no known competing financial interests or personal relationships that could have appeared to influence the work reported in this paper.

Data availability

Data will be made available from the corresponding author upon reasonable request.

Acknowledgments

The PhD scholarship of Andrea Macrelli and part of this research study pertain to the *Energy for Motion* project of the Department of Energy of Politecnico di Milano, funded by the Italian Ministry of University and Research (MIUR) through the *Department of Excellence* grant 2018 – 2022.

References

- 1
2
3 [1] X. Jia, C. Liu, Z.G. Neale, J. Yang, G. Cao, Active materials for aqueous zinc ion Batteries:
4
5 Synthesis, crystal structure, morphology, and electrochemistry, *Chem. Rev.* 120 (2020)
6
7 7795–7866. <https://doi.org/10.1021/acs.chemrev.9b00628>.
8
9
- 10 [2] T. Zhou, L. Zhu, L. Xie, Q. Han, X. Yang, L. Chen, G. Wang, X. Cao, Cathode materials for
11
12 aqueous zinc-ion batteries: A mini review, *J. Colloid Interface Sci.* 605 (2022) 828–850.
13
14 <https://doi.org/10.1016/j.jcis.2021.07.138>.
15
16
- 17 [3] L. Wang, J. Zheng, Recent advances in cathode materials of rechargeable aqueous zinc-ion
18
19 batteries, *Mater. Today Adv.* 7 (2020) 1000782.
20
21 <https://doi.org/10.1016/j.mtadv.2020.100078>.
22
23
- 24 [4] N. Wang, H. Wan, J. Duan, X. Wang, L. Tao, J. Zhang, H. Wang, A review of zinc-based
25
26 battery from alkaline to acid, *Mater. Today Adv.* 11 (2021) 100149.
27
28 <https://doi.org/10.1016/j.mtadv.2021.100149>.
29
30
- 31 [5] N. Borchers, S. Clark, B. Horstmann, K. Jayasayee, M. Juel, P. Stevens, Innovative zinc-
32
33 based batteries, *J. Power Sources* 484 (2021) 229309.
34
35 <https://doi.org/10.1016/j.jpowsour.2020.229309>.
36
37
- 38 [6] L.E. Blanc, D. Kundu, L.F. Nazar, Scientific challenges for the implementation of Zn-ion
39
40 batteries, *Joule* 4 (2020) 771–799. <https://doi.org/10.1016/j.joule.2020.03.002>.
41
42
- 43 [7] V.P.H. Huy, L.T. Hieu, J. Hur, Zn metal anodes for Zn-ion batteries in mild aqueous
44
45 electrolytes: Challenges and strategies, *Nanomaterials* 11 (2021) 2746.
46
47 <https://doi.org/10.3390/nano11102746>.
48
49
50
51
52
53
54
55
56
57
58
59
60
61
62
63
64
65

- 1
2
3
4
5
6
7
8
9
10
11
12
13
14
15
16
17
18
19
20
21
22
23
24
25
26
27
28
29
30
31
32
33
34
35
36
37
38
39
40
41
42
43
44
45
46
47
48
49
50
51
52
53
54
55
56
57
58
59
60
61
62
63
64
65
- [8] C. Li, X. Xie, S. Liang, J. Zhou, Issues and future perspective on zinc metal anode for rechargeable aqueous zinc-ion batteries, *Energy Environ. Mater.* 3 (2020) 146–159. <https://doi.org/10.1002/eem2.12067>.
- [9] Y. Geng, L. Pan, Z. Peng, Z. Sun, H. Lin, C. Mao, L. Wang, L. Dai, H. Liu, K. Pan, X. Wu, Q. Zhang, Z. He, Electrolyte additive engineering for aqueous Zn ion batteries, *Energy Storage Mater.* 51 (2022) 733–755. <https://doi.org/10.1016/j.ensm.2022.07.017>.
- [10] N. Guo, W. Huo, X. Dong, Z. Sun, Y. Lu, X. Wu, L. Dai, L. Wang, H. Lin, H. Liu, H. Liang, Z. He, Q. Zhang, A Review on 3D zinc anodes for zinc ion batteries, *Small Methods* 6 (2022) 2200597. <https://doi.org/10.1002/smt.202200597>.
- [11] T. Wang, C. Li, X. Xie, B. Lu, Z. He, S. Liang, J. Zhou, Anode materials for aqueous zinc ion batteries: Mechanisms, properties, and perspectives, *ACS Nano* 14 (2020) 16321–16347. <https://doi.org/10.1021/acsnano.0c07041>.
- [12] H. Li, L. Ma, C. Han, Z. Wang, Z. Liu, Z. Tang, C. Zhi, Advanced rechargeable zinc-based batteries: Recent progress and future perspectives, *Nano Energy* 62 (2019) 550–587. <https://doi.org/10.1016/j.nanoen.2019.05.059>.
- [13] B. Tang, L. Shan, S. Liang, J. Zhou, Issues and opportunities facing aqueous zinc-ion batteries, *Energy Environ. Sci.* 12 (2019) 3288–3304. <https://doi.org/10.1039/c9ee02526j>.
- [14] M. Song, H. Tan, D. Chao, H.J. Fan, Recent advances in Zn-ion batteries, *Adv. Funct. Mater.* 28 (2018) 1802564. <https://doi.org/10.1002/adfm.201802564>.
- [15] X. Guo, J. Zhou, C. Bai, X. Li, G. Fang, S. Liang, Zn/MnO₂ battery chemistry with dissolution-deposition mechanism, *Mater. Today Energy* 16 (2020) 100396. <https://doi.org/10.1016/j.mtener.2020.100396>.

- 1
2
3
4
5
6
7
8
9
10
11
12
13
14
15
16
17
18
19
20
21
22
23
24
25
26
27
28
29
30
31
32
33
34
35
36
37
38
39
40
41
42
43
44
45
46
47
48
49
50
51
52
53
54
55
56
57
58
59
60
61
62
63
64
65
- [16] B. Lee, C.S. Yoon, H.R. Lee, K.Y. Chung, B.W. Cho, S.H. Oh, Electrochemically-induced reversible transition from the tunneled to layered polymorphs of manganese dioxide, *Sci. Rep.* 4 (2014) 6066. <https://doi.org/10.1038/srep06066>.
- [17] W. Sun, F. Wang, S. Hou, C. Yang, X. Fan, Z. Ma, T. Gao, F. Han, R. Hu, M. Zhu, C. Wang, Zn/MnO₂ battery chemistry with H⁺ and Zn²⁺ coininsertion, *J. Am. Chem. Soc.* 139 (2017) 9775–9778. <https://doi.org/10.1021/jacs.7b04471>.
- [18] L. Li, T.K.A. Hoang, J. Zhi, M. Han, S. Li, P. Chen, Functioning mechanism of the secondary aqueous Zn-β-MnO₂ battery, *ACS Appl. Mater. Interfaces* 12 (2020) 12834–12846. <https://doi.org/10.1021/acsami.9b22758>.
- [19] M.H. Alfaruqi, V. Mathew, J. Gim, S. Kim, J. Song, J.P. Baboo, S.H. Choi, J. Kim, Electrochemically induced structural transformation in a γ-MnO₂ cathode of a high capacity zinc-ion battery system, *Chem. Mater.* 27 (2015) 3609–3620. <https://doi.org/10.1021/cm504717p>.
- [20] M.H. Alfaruqi, S. Islam, D.Y. Putro, V. Mathew, S. Kim, J. Jo, S. Kim, Y.K. Sun, K. Kim, J. Kim, Structural transformation and electrochemical study of layered MnO₂ in rechargeable aqueous zinc-ion battery, *Electrochim. Acta* 276 (2018) 1–11. <https://doi.org/10.1016/j.electacta.2018.04.139>.
- [21] V. Mathew, B. Sambandam, S. Kim, S. Kim, S. Park, S. Lee, M.H. Alfaruqi, V. Soundharrajan, S. Islam, D.Y. Putro, J.Y. Hwang, Y.K. Sun, J. Kim, Manganese and vanadium oxide cathodes for aqueous rechargeable zinc-ion batteries: A focused view on performance, mechanism, and developments, *ACS Energy Lett.* 5 (2020) 2376–2400. <https://doi.org/10.1021/acsenergylett.0c00740>.

- 1
2
3
4
5
6
7
8
9
10
11
12
13
14
15
16
17
18
19
20
21
22
23
24
25
26
27
28
29
30
31
32
33
34
35
36
37
38
39
40
41
42
43
44
45
46
47
48
49
50
51
52
53
54
55
56
57
58
59
60
61
62
63
64
65
- [22] W. Zhang, C. Zuo, C. Tang, W. Tang, B. Lan, X. Fu, S. Dong, P. Luo, The current developments and perspectives of V_2O_5 as cathode for rechargeable aqueous zinc-ion batteries, *Energy Technol.* 9 (2021) 2000789. <https://doi.org/10.1002/ente.202000789>.
- [23] S. Liu, L. Kang, J.M. Kim, Y.T. Chun, J. Zhang, S.C. Jun, Recent advances in vanadium-based aqueous rechargeable zinc-ion batteries, *Adv. Energy Mater.* 10 (2020). <https://doi.org/10.1002/aenm.202000477>.
- [24] G. Zampardi, F. La Mantia, Prussian blue analogues as aqueous Zn-ion batteries electrodes: Current challenges and future perspectives, *Curr. Opin. Electrochemistry* 21 (2020) 84–92. <https://doi.org/10.1016/j.coelec.2020.01.014>.
- [25] H. Cui, T. Wang, Z. Huang, G. Liang, Z. Chen, A. Chen, D. Wang, Q. Yang, H. Hong, J. Fan, C. Zhi, High-voltage organic cathodes for zinc-ion batteries through electron cloud and solvation structure regulation, *Angew. Chem. Int. Ed.* 61 (2022) e202203453. <https://doi.org/10.1002/anie.202203453>.
- [26] S. Xu, M. Sun, Q. Wang, C. Wang, Recent progress in organic electrodes for zinc-ion batteries, *J. Semicond.* 41 (2020) 091704. <https://doi.org/10.1088/1674-4926/41/9/091704>.
- [27] J. Wang, J.G. Wang, H. Liu, Z. You, C. Wei, F. Kang, Electrochemical activation of commercial MnO microsized particles for high-performance aqueous zinc-ion batteries, *J. Power Sources* 438 (2019) 226951. <https://doi.org/10.1016/j.jpowsour.2019.226951>.
- [28] C. Zhu, G. Fang, S. Liang, Z. Chen, Z. Wang, J. Ma, H. Wang, B. Tang, X. Zheng, J. Zhou, Electrochemically induced cationic defect in MnO intercalation cathode for aqueous zinc-ion battery, *Energy Storage Mater.* 24 (2020) 394–401. <https://doi.org/10.1016/j.ensm.2019.07.030>.

- 1
2
3
4
5
6
7
8
9
10
11
12
13
14
15
16
17
18
19
20
21
22
23
24
25
26
27
28
29
30
31
32
33
34
35
36
37
38
39
40
41
42
43
44
45
46
47
48
49
50
51
52
53
54
55
56
57
58
59
60
61
62
63
64
65
- [29] M. Sun, D.S. Li, Y.F. Wang, W.L. Liu, M.M. Ren, F.G. Kong, S.J. Wang, Y.Z. Guo, Y.M. Liu, Mn₃O₄@NC composite nanorods as a cathode for rechargeable aqueous Zn-ion batteries, *ChemElectroChem* 6 (2019) 2510–2516. <https://doi.org/10.1002/celec.201900376>.
- [30] J. Hao, J. Mou, J. Zhang, L. Dong, W. Liu, C. Xu, F. Kang, Electrochemically induced spinel-layered phase transition of Mn₃O₄ in high performance neutral aqueous rechargeable zinc battery, *Electrochim. Acta* 259 (2018) 170–178. <https://doi.org/10.1016/j.electacta.2017.10.166>.
- [31] H. Jiang, X. Ji, Counter-ion insertion of chloride in Mn₃O₄ as cathode for dual-ion batteries: A new mechanism of electrosynthesis for reversible anion storage, *Carbon Energy* 2 (2020) 437–442. <https://doi.org/10.1002/cey2.37>.
- [32] C. Zhu, G. Fang, J. Zhou, J. Guo, Z. Wang, C. Wang, J. Li, Y. Tang, S. Liang, Binder-free stainless steel@Mn₃O₄ nanoflower composite: A high-activity aqueous zinc-ion battery cathode with high-capacity and long-cycle-life, *J. Mater. Chem. A* 6 (2018) 9677–9683. <https://doi.org/10.1039/c8ta01198b>.
- [33] D. Feng, T.N. Gao, L. Zhang, B. Guo, S. Song, Z.A. Qiao, S. Dai, Boosting high-rate zinc-storage performance by the rational design of Mn₂O₃ nanoporous architecture cathode, *Nano-Micro Lett.* 12 (2020) 14. <https://doi.org/10.1007/s40820-019-0351-4>.
- [34] Y. Ma, Y. Ma, T. Diemant, K. Cao, X. Liu, U. Kaiser, R.J. Behm, A. Varzi, S. Passerini, Unveiling the intricate intercalation mechanism in manganese sesquioxide as positive electrode in aqueous Zn-metal battery, *Adv. Energy Mater.* 11 (2021) 2100962. <https://doi.org/10.1002/aenm.202100962>.
- [35] B. Jiang, C. Xu, C. Wu, L. Dong, J. Li, F. Kang, Manganese sesquioxide as cathode material for multivalent zinc ion battery with high capacity and long cycle life, *Electrochim. Acta* 229 (2017) 422–428. <https://doi.org/10.1016/j.electacta.2017.01.163>.

- 1
2
3
4
5
6
7
8
9
10
11
12
13
14
15
16
17
18
19
20
21
22
23
24
25
26
27
28
29
30
31
32
33
34
35
36
37
38
39
40
41
42
43
44
45
46
47
48
49
50
51
52
53
54
55
56
57
58
59
60
61
62
63
64
65
- [36] Y. Cai, R. Chua, S. Huang, H. Ren, M. Srinivasan, Amorphous manganese dioxide with the enhanced pseudocapacitive performance for aqueous rechargeable zinc-ion battery, *Chem. Eng. J.* 396 (2020) 125221. <https://doi.org/10.1016/j.cej.2020.125221>.
- [37] Y. Wu, J. Fee, Z. Tobin, A. Shirazi-Amin, P. Kerns, S. Dissanayake, A. Mirich, S.L. Suib, Amorphous manganese oxides: An approach for reversible aqueous zinc-ion batteries, *ACS Appl. Energy Mater.* 3 (2020) 1627–1633. <https://doi.org/10.1021/acsaem.9b02119>.
- [38] M.H. Alfaruqi, J. Gim, S. Kim, J. Song, J. Jo, S. Kim, V. Mathew, J. Kim, Enhanced reversible divalent zinc storage in a structurally stable α -MnO₂ nanorod electrode, *J. Power Sources* 288 (2015) 320–327. <https://doi.org/10.1016/j.jpowsour.2015.04.140>.
- [39] B. Lee, H.R. Lee, H. Kim, K.Y. Chung, B.W. Cho, S.H. Oh, Elucidating the intercalation mechanism of zinc ions into α -MnO₂ for rechargeable zinc batteries, *Chem. Commun.* 51 (2015) 9265–9268. <https://doi.org/10.1039/c5cc02585k>.
- [40] S. Islam, M.H. Alfaruqi, V. Mathew, J. Song, S. Kim, S. Kim, J. Jo, J.P. Baboo, D.T. Pham, D.Y. Putro, Y.K. Sun, J. Kim, Facile synthesis and the exploration of the zinc storage mechanism of β -MnO₂ nanorods with exposed (101) planes as a novel cathode material for high performance eco-friendly zinc-ion batteries, *J. Mater. Chem. A* 5 (2017) 23299–23309. <https://doi.org/10.1039/c7ta07170a>.
- [41] M.H. Alfaruqi, J. Gim, S. Kim, J. Song, D.T. Pham, J. Jo, Z. Xiu, V. Mathew, J. Kim, A layered δ -MnO₂ nanoflake cathode with high zinc-storage capacities for eco-friendly battery applications, *Electrochem. Commun.* 60 (2015) 121–125. <https://doi.org/10.1016/j.elecom.2015.08.019>.
- [42] C. Guo, H. Liu, J. Li, Z. Hou, J. Liang, J. Zhou, Y. Zhu, Y. Qian, Ultrathin δ -MnO₂ nanosheets as cathode for aqueous rechargeable zinc ion battery, *Electrochim. Acta* 304 (2019) 370–377. <https://doi.org/10.1016/j.electacta.2019.03.008>.

- 1
2
3
4
5
6
7
8
9
10
11
12
13
14
15
16
17
18
19
20
21
22
23
24
25
26
27
28
29
30
31
32
33
34
35
36
37
38
39
40
41
42
43
44
45
46
47
48
49
50
51
52
53
54
55
56
57
58
59
60
61
62
63
64
65
- [43] D. Chao, W. Zhou, C. Ye, Q. Zhang, Y. Chen, L. Gu, K. Davey, S. Qiao, An electrolytic Zn–MnO₂ battery for high- voltage and scalable energy storage, *Angew. Chem. Int. Ed.* 58 (2019) 7823–7828. <https://doi.org/https://doi.org/10.1002/anie.201904174>.
- [44] C. Yuan, Y. Zhang, Y. Pan, X. Liu, G. Wang, D. Cao, Investigation of the intercalation of polyvalent cations (Mg²⁺, Zn²⁺) into λ-MnO₂ for rechargeable aqueous battery, *Electrochim. Acta* 116 (2014) 404–412. <https://doi.org/10.1016/j.electacta.2013.11.090>.
- [45] J. Lee, J.B. Ju, W. il Cho, B.W. Cho, S.H. Oh, Todorokite-type MnO₂ as a zinc-ion intercalating material, *Electrochim. Acta* 112 (2013) 138–143. <https://doi.org/10.1016/j.electacta.2013.08.136>.
- [46] L. Nádherný, M. Maryško, D. Sedmidubský, C. Martin, Structural and magnetic properties of Zn_xMn_{3-x}O₄ spinels, *J. Magn. Magn. Mater.* 413 (2016) 89–96. <https://doi.org/10.1016/j.jmmm.2016.04.029>.
- [47] M. Peiteado, S. Sturm, A.C. Caballero, D. Makovec, Mn_{3-x}Zn_xO₄ spinel phases in the Zn–Mn–O system, *Acta Mater.* 56 (2008) 4028–4035. <https://doi.org/10.1016/j.actamat.2008.04.024>.
- [48] S. Guillemet-Fritsch, C. Chanel, J. Sarrias, S. Bayonne, A. Rousset, X. Alcobe, M.L. Martinez Sarriòn, Structure, thermal stability and electrical properties of zinc manganites, *Solid State Ion.* 128 (2000) 233–242. [https://doi.org/https://doi.org/10.1016/S0167-2738\(99\)00340-9](https://doi.org/https://doi.org/10.1016/S0167-2738(99)00340-9).
- [49] L. Malavasi, P. Galinetto, M.C. Mozzati, C.B. Azzoni, G. Flor, Raman spectroscopy of AMn₂O₄ (A = Mn, Mg and Zn) spinels, *Phys. Chem. Chem. Phys.* 4 (2002) 3876–3880. <https://doi.org/10.1039/b203520k>.

- 1
2
3
4
5
6
7
8
9
10
11
12
13
14
15
16
17
18
19
20
21
22
23
24
25
26
27
28
29
30
31
32
33
34
35
36
37
38
39
40
41
42
43
44
45
46
47
48
49
50
51
52
53
54
55
56
57
58
59
60
61
62
63
64
65
- [50] A. Baby, B. Senthilkumar, P. Barpanda, Low-cost rapid template-free synthesis of nanoscale zinc spinels for energy storage and electrocatalytic applications, *ACS Appl. Energy Mater.* 2 (2019) 3211–3219. <https://doi.org/10.1021/acsaem.9b00054>.
- [51] N. Zhang, F. Cheng, Y. Liu, Q. Zhao, K. Lei, C. Chen, X. Liu, J. Chen, Cation-deficient spinel ZnMn_2O_4 cathode in $\text{Zn}(\text{CF}_3\text{SO}_3)_2$ electrolyte for rechargeable aqueous Zn-ion battery, *J. Am. Chem. Soc.* 138 (2016) 12894–12901. <https://doi.org/10.1021/jacs.6b05958>.
- [52] J.C. Knight, S. Therese, A. Manthiram, Chemical extraction of Zn from ZnMn_2O_4 -based spinels, *J. Mater. Chem. A* 3 (2015) 21077–21082. <https://doi.org/10.1039/c5ta06482a>.
- [53] K. Cai, S. hua Luo, J. Feng, J. Wang, Y. Zhan, Q. Wang, Y. Zhang, X. Liu, Recent advances on spinel zinc manganate cathode materials for zinc-ion batteries, *Chem. Rec.* 22 (2022) e202100169. <https://doi.org/10.1002/tcr.202100169>.
- [54] H. Zhang, J. Wang, Q. Liu, W. He, Z. Lai, X. Zhang, M. Yu, Y. Tong, X. Lu, Extracting oxygen anions from ZnMn_2O_4 : Robust cathode for flexible all-solid-state Zn-ion batteries, *Energy Storage Mater.* 21 (2019) 154–161. <https://doi.org/10.1016/j.ensm.2018.12.019>.
- [55] J.W. Lee, S.D. Seo, D.W. Kim, Comparative study on ternary spinel cathode Zn–Mn–O microspheres for aqueous rechargeable zinc-ion batteries, *J. Alloys Compd.* 800 (2019) 478–482. <https://doi.org/10.1016/j.jallcom.2019.06.051>.
- [56] T.H. Wu, W.Y. Liang, Reduced intercalation energy barrier by rich structural water in spinel ZnMn_2O_4 for high-rate zinc-ion batteries, *ACS Appl. Mater. Interfaces* 13 (2021) 23822–23832. <https://doi.org/10.1021/acsaami.1c05150>.
- [57] S. Islam, M.H. Alfaruqi, D.Y. Putro, S. Park, S. Kim, S. Lee, M.S. Ahmed, V. Mathew, Y.K. Sun, J.Y. Hwang, J. Kim, In situ oriented Mn deficient ZnMn_2O_4 @C nanoarchitecture for durable rechargeable aqueous zinc-ion batteries, *Adv. Sci.* 8 (2021) 2002636. <https://doi.org/10.1002/advs.202002636>.

- 1
2
3
4
5
6
7
8
9
10
11
12
13
14
15
16
17
18
19
20
21
22
23
24
25
26
27
28
29
30
31
32
33
34
35
36
37
38
39
40
41
42
43
44
45
46
47
48
49
50
51
52
53
54
55
56
57
58
59
60
61
62
63
64
65
- [58] S. Wang, S. Zhang, X. Chen, G. Yuan, B. Wang, J. Bai, H. Wang, G. Wang, Double-shell zinc manganate hollow microspheres embedded in carbon networks as cathode materials for high-performance aqueous zinc-ion batteries, *J. Colloid Interface Sci.* 580 (2020) 528–539. <https://doi.org/10.1016/j.jcis.2020.07.053>.
- [59] X. Wu, Y. Xiang, Q. Peng, X. Wu, Y. Li, F. Tang, R. Song, Z. Liu, Z. He, X. Wu, Green-low-cost rechargeable aqueous zinc-ion batteries using hollow porous spinel ZnMn_2O_4 as the cathode material, *J. Mater. Chem. A* 5 (2017) 17990–17997. <https://doi.org/10.1039/c7ta00100b>.
- [60] L. Chen, Z. Yang, H. Qin, X. Zeng, J. Meng, H. Chen, Graphene-wrapped hollow ZnMn_2O_4 microspheres for high-performance cathode materials of aqueous zinc ion batteries, *Electrochim. Acta* 317 (2019) 155–163. <https://doi.org/10.1016/j.electacta.2019.05.147>.
- [61] L. Chen, Z. Yang, H. Qin, X. Zeng, J. Meng, Advanced electrochemical performance of $\text{ZnMn}_2\text{O}_4/\text{N}$ -doped graphene hybrid as cathode material for zinc ion battery, *J. Power Sources* 425 (2019) 162–169. <https://doi.org/10.1016/j.jpowsour.2019.04.010>.
- [62] M.B. Sassin, M.E. Helms, J.F. Parker, C.N. Chervin, R.H. Deblock, J.S. Ko, D.R. Rolison, J.W. Long, Elucidating zinc-ion battery mechanisms in freestanding carbon electrode architectures decorated with nanocrystalline ZnMn_2O_4 , *Mater. Adv.* 2 (2021) 2730–2738. <https://doi.org/10.1039/d1ma00159k>.
- [63] Z. Yao, D. Cai, Z. Cui, Q. Wang, H. Zhan, Strongly coupled zinc manganate nanodots and graphene composite as an advanced cathode material for aqueous zinc ion batteries, *Ceram. Int.* 46 (2020) 11237–11245. <https://doi.org/10.1016/j.ceramint.2020.01.148>.
- [64] C. Yang, M. Han, H. Yan, F. Li, M. Shi, L. Zhao, In-situ probing phase evolution and electrochemical mechanism of ZnMn_2O_4 nanoparticles anchored on porous carbon

polyhedrons in high-performance aqueous Zn-ion batteries, *J. Power Sources* 452 (2020) 227826. <https://doi.org/10.1016/j.jpowsour.2020.227826>.

[65] S. Deng, Z. Tie, F. Yue, H. Cao, M. Yao, Z. Niu, Rational design of ZnMn₂O₄ quantum dots in a carbon framework for durable aqueous zinc-ion batteries, *Angew. Chem. Int. Ed.* 61 (2022) e202115877. <https://doi.org/10.1002/anie.202115877>.

[66] Y. Tao, Z. Li, L. Tang, X. Pu, T. Cao, D. Cheng, Q. Xu, H. Liu, Y.G. Wang, Y. Xia, Nickel and cobalt co-substituted spinel ZnMn₂O₄@N-rGO for increased capacity and stability as a cathode material for rechargeable aqueous zinc-ion battery, *Electrochim. Acta* 331 (2020) 135296. <https://doi.org/10.1016/j.electacta.2019.135296>.

[67] K. Cai, S. Luo, J. Cong, K. Li, S. Yan, P. Hou, Q. Wang, Y. Zhang, X. Liu, X. Lei, Synthesis and optimization of ZnMn₂O₄ cathode material for zinc-ion battery by citric acid sol-gel method, *J. Electrochem. Soc.* 169 (2022) 030531. <https://doi.org/10.1149/1945-7111/ac5baa>.

[68] T. Shao, Y. Zhang, T. Cao, Y. Yang, Z. Li, H. Liu, Y. Wang, X. Yongyao, Structural regulation of ZnMn₂O₄ cathode material by K, Fe-double doping to improve its rate and cycling stability for rechargeable aqueous zinc-based batteries, *Chem. Eng. J.* 431 (2022) 133735. <https://doi.org/10.1016/j.cej.2021.133735>.

[69] S. Yang, M. Zhang, X. Wu, X. Wu, F. Zeng, Y. Li, S. Duan, D. Fan, Y. Yang, X. Wu, The excellent electrochemical performances of ZnMn₂O₄/Mn₂O₃: The composite cathode material for potential aqueous zinc ion batteries, *J. Electroanal. Chem.* 832 (2019) 69–74. <https://doi.org/10.1016/j.jelechem.2018.10.051>.

[70] Y. Zeng, Y. Wang, Q. Jin, Z. Pei, D. Luan, X. Zhang, X.W. Lou, Rationally designed Mn₂O₃-ZnMn₂O₄ hollow heterostructures from metal-organic frameworks for stable Zn-ion

storage, *Angew. Chem. Int. Ed.* 60 (2021) 25793–25798.

<https://doi.org/10.1002/anie.202113487>.

- [71] S.C. Ma, M. Sun, S.X. Wang, D.S. Li, W.L. Liu, M.M. Ren, F.G. Kong, S.J. Wang, Y.M. Xia, Zinc manganate/manganic oxide bi-component nanorod as excellent cathode for zinc-ion battery, *Scr. Mater.* 194 (2021) 113707.
<https://doi.org/10.1016/j.scriptamat.2020.113707>.
- [72] M. Shi, B. Wang, Y. Shen, J. Jiang, W. Zhu, Y. Su, M. Narayanasamy, S. Angaiah, C. Yan, Q. Peng, 3D assembly of MXene-stabilized spinel ZnMn_2O_4 for highly durable aqueous zinc-ion batteries, *Chem. Eng. J.* 399 (2020) 125627.
<https://doi.org/10.1016/j.cej.2020.125627>.
- [73] W. Qiu, H. Xiao, H. Feng, Z. Lin, H. Gao, W. He, X. Lu, Defect modulation of ZnMn_2O_4 nanotube arrays as high-rate and durable cathode for flexible quasi-solid-state zinc ion battery, *Chem. Eng. J.* 422 (2021) 129890. <https://doi.org/10.1016/j.cej.2021.129890>.
- [74] T.H. Wu, C.C. Huang, S.L. Cheng, C.C. Lin, Expanded spinel $\text{Zn}_x\text{Mn}_2\text{O}_4$ induced by electrochemical activation of glucose-mediated manganese oxide for stable cycle performance in zinc-ion batteries, *J. Colloid Interface Sci.* 617 (2022) 274–283.
<https://doi.org/10.1016/j.jcis.2022.03.017>.
- [75] V. Soundharajan, B. Sambandam, S. Kim, S. Islam, J. Jo, S. Kim, V. Mathew, Y. kook Sun, J. Kim, The dominant role of Mn^{2+} additive on the electrochemical reaction in ZnMn_2O_4 cathode for aqueous zinc-ion batteries, *Energy Storage Mater.* 28 (2020) 407–417. <https://doi.org/10.1016/j.ensm.2019.12.021>.
- [76] C.M. Julien, A. Mauger, Pulsed laser deposited films for microbatteries, *Coatings* 9 (2019) 386. <https://doi.org/doi:10.3390/coatings9060386>.

- 1
2
3
4
5
6
7
8
9
10
11
12
13
14
15
16
17
18
19
20
21
22
23
24
25
26
27
28
29
30
31
32
33
34
35
36
37
38
39
40
41
42
43
44
45
46
47
48
49
50
51
52
53
54
55
56
57
58
59
60
61
62
63
64
65
- [77] M. Fenech, N. Sharma, Pulsed laser deposition-based thin film microbatteries, *Chem. Asian. J.* 15 (2020) 1829–1847. <https://doi.org/10.1002/asia.202000384>.
- [78] L. Indrizzi, N. Ohannessian, D. Pergolesi, T. Lippert, E. Gilardi, Pulsed laser deposition as a tool for the development of all solid-state microbatteries, *Helv. Chim. Acta.* 104 (2021) e2000203. <https://doi.org/10.1002/hlca.202000203>.
- [79] P.R. Willmott, J.R. Huber, Pulsed laser vaporization and deposition, *Rev. Mod. Phys.* 72 (2000) 315–328. <https://doi.org/https://doi.org/10.1103/RevModPhys.72.315>.
- [80] C.S. Casari, A. Li Bassi, Pulsed Laser Deposition of nanostructured oxides: From clusters to functional films, in: W.T. Arkin (Ed.), *Advances in Laser and Optics Research*, Vol. 7, Ch. 2, Nova Science Publishers, Inc., Hauppauge (NY), USA, 2011, pp. 65–100.
- [81] F. Rossi, E. Marini, M. Boniardi, A. Casaroli, A. Li Bassi, A. Macrelli, C. Mele, B. Bozzini, What happens to MnO₂ when it comes in contact with Zn²⁺? An electrochemical study in aid of Zn/MnO₂-based rechargeable batteries, *Energy Technol.* 10 (2022) 2200084. <https://doi.org/10.1002/ente.202200084>.
- [82] S. Åsbrink, A. Waśkowska, L. Gerward, J. Staun Olsen, E. Talik, High-pressure phase transition and properties of spinel ZnMn₂O₄, *Phys. Rev. B.* 60 (1999) 12651–12656. <https://doi.org/10.1103/PhysRevB.60.12651>.
- [83] R. Matarrese, I. Nova, A. Li Bassi, C.S. Casari, V. Russo, S. Palmas, Preparation and optimization of TiO₂ photoanodes fabricated by pulsed laser deposition for photoelectrochemical water splitting, *J. Solid State Electrochem.* 21 (2017) 3139–3154. <https://doi.org/10.1007/s10008-017-3639-7>.
- [84] P. Gondoni, P. Mazzolini, V. Russo, M. Diani, M. Amati, L. Gregoratti, V. De Renzi, G.C. Gazzadi, J. Martí-Rujas, A. Li Bassi, C.S. Casari, Tuning electrical properties of

1 hierarchically assembled Al-doped ZnO nanoforests by room temperature Pulsed Laser
2 Deposition, *Thin Solid Films* 594 (2015) 12–17. <https://doi.org/10.1016/j.tsf.2015.09.066>.

- 3
4
5 [85] A. Bailini, F. Di Fonzo, M. Fusi, C.S. Casari, A. Li Bassi, V. Russo, A. Baserga, C.E.
6 Bottani, Pulsed laser deposition of tungsten and tungsten oxide thin films with tailored
7 structure at the nano- and mesoscale, *Appl. Surf. Sci.* 253 (2007) 8130–8135.
8 <https://doi.org/10.1016/j.apsusc.2007.02.145>.
9
10
11
12
13
14
15 [86] B.R. Bricchi, L. Mascaretti, S. Garattoni, M. Mazza, M. Ghidelli, A. Naldoni, A. Li Bassi,
16 Nanoporous titanium (oxy)nitride films as broadband solar absorbers, *ACS Appl. Mater.*
17 *Interfaces* 14 (2022) 18453–18463. <https://doi.org/10.1021/acsami.2c01185>.
18
19
20
21
22
23 [87] F. Di Fonzo, C.S. Casari, V. Russo, M.F. Brunella, A. Li Bassi, C.E. Bottani, Hierarchically
24 organized nanostructured TiO₂ for photocatalysis applications, *Nanotechnology* 20 (2009)
25 015604. <https://doi.org/10.1088/0957-4484/20/1/015604>.
26
27
28
29
30
31 [88] H. Li, B. Song, W.J. Wang, X.L. Chen, Facile synthesis, thermal, magnetic, Raman
32 characterizations of spinel structure ZnMn₂O₄, *Mater. Chem. Phys.* 130 (2011) 39–44.
33 <https://doi.org/10.1016/j.matchemphys.2011.04.072>.
34
35
36
37
38
39 [89] K. Samanta, S. Dussan, R.S. Katiyar, P. Bhattacharya, Structural and optical properties of
40 nanocrystalline Zn_{1-x}Mn_xO, *Appl. Phys. Lett.* 90 (2007) 261903.
41 <https://doi.org/10.1063/1.2751593>.
42
43
44
45
46
47 [90] C.M. Julien, M. Massot, C. Poinsignon, Lattice vibrations of manganese oxides: Part I.
48 Periodic structures, *Spectrochim. Acta A Mol. Biomol. Spectrosc.* 60 (2004) 689–700.
49 [https://doi.org/10.1016/S1386-1425\(03\)00279-8](https://doi.org/10.1016/S1386-1425(03)00279-8).
50
51
52
53
54
55 [91] M. Tortosa, F.J. Manjón, M. Mollar, B. Marí, ZnO-based spinels grown by
56 electrodeposition, *J. Phys. Chem. Solids.* 73 (2012) 1111–1115.
57 <https://doi.org/10.1016/j.jpcs.2012.04.002>.
58
59
60
61
62
63
64
65

- 1
2
3
4
5
6
7
8
9
10
11
12
13
14
15
16
17
18
19
20
21
22
23
24
25
26
27
28
29
30
31
32
33
34
35
36
37
38
39
40
41
42
43
44
45
46
47
48
49
50
51
52
53
54
55
56
57
58
59
60
61
62
63
64
65
- [92] J. Zuo, C. Xu, Y. Liu, Y. Qian, Crystallite size effects on the Raman spectra of Mn₃O₄, *NanoStructured Mater.* 10 (1998) 1331–1335. [https://doi.org/https://doi.org/10.1016/S0965-9773\(99\)00002-1](https://doi.org/https://doi.org/10.1016/S0965-9773(99)00002-1).
- [93] A.V. Chichagov, D.A. Varlamov, R.A. Dilanyan, T.N. Dokina, N.A. Drozhzhina, O.L. Samokhvalova, T.V. Ushakovskaya, MINCRYST: A crystallographic database for minerals, local and network (WWW) versions, *Crystallogr. Rep.* 46 (2001) 876–879. <https://doi.org/https://doi.org/10.1134/1.1405882>.
- [94] WWW-MINCRYST. Crystallographic and crystallochemical database for minerals and their structural analogues. <http://database.iem.ac.ru/mincryst> (accessed July 29, 2022).
- [95] G.K. Williamson, W.H. Hall, X-ray line broadening from fcc aluminium and wolfram, *Acta Metall.* 1 (1953) 22–31. [https://doi.org/https://doi.org/10.1016/0001-6160\(53\)90006-6](https://doi.org/https://doi.org/10.1016/0001-6160(53)90006-6).
- [96] D. Nath, F. Singh, R. Das, X-ray diffraction analysis by Williamson-Hall, Halder-Wagner and size-strain plot methods of CdSe nanoparticles - a comparative study, *Mater. Chem. Phys.* 239 (2020) 122021. <https://doi.org/10.1016/j.matchemphys.2019.122021>.
- [97] S. Bernardini, F. Bellatreccia, A. Casanova Municchia, G. Della Ventura, A. Sodo, Raman spectra of natural manganese oxides, *J. Raman Spectrosc.* 50 (2019) 873–888. <https://doi.org/10.1002/jrs.5583>.
- [98] J. Yang, J. Cao, Y. Peng, W. Yang, S. Barg, Z. Liu, I.A. Kinloch, M.A. Bissett, R.A.W. Dryfe, Unravelling the mechanism of rechargeable aqueous Zn–MnO₂ batteries: Implementation of charging process by electrodeposition of MnO₂, *ChemSusChem* 13 (2020) 4103–4110. <https://doi.org/10.1002/cssc.202001216>.

Figures and captions

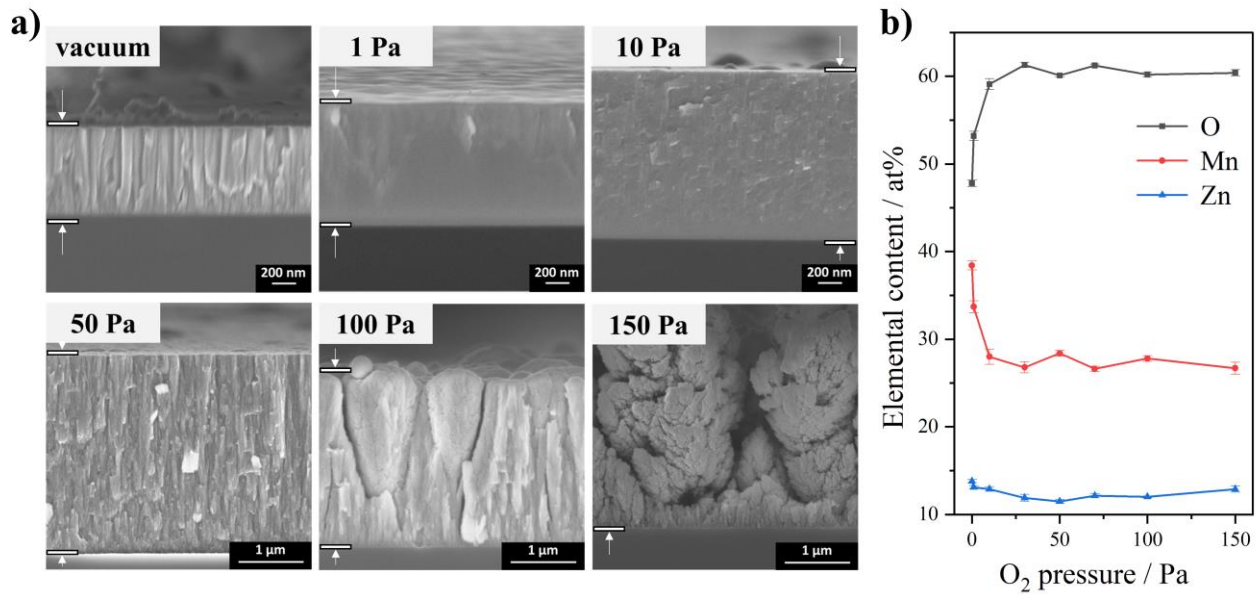


Fig. 1. (a) SEM cross-sectional images of the ZMO thin films deposited on Si at different O₂ pressure, at constant laser fluence of $\sim 3.7 \text{ J cm}^{-2}$ and 15 min deposition time. (b) EDX elemental analysis of as-deposited ZMO films.

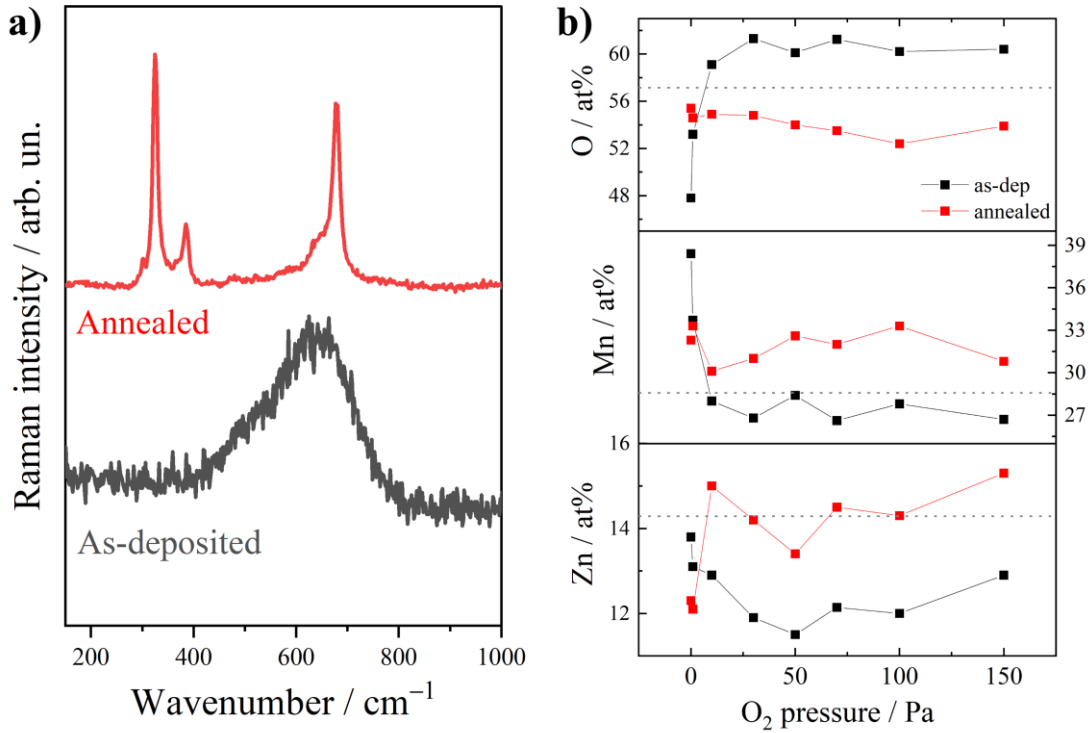


Fig. 2. (a) Comparison between the Raman spectra of the ZMO film deposited at 50 Pa of O₂ (~3.7 J cm⁻²) before and after air annealing at 600 °C, 3h. (b) EDX elemental analysis of air-annealed ZMO films (600 °C, 3h); for comparison, also the atomic content of as-deposited samples is reported. The grey dashed lines correspond to O, Mn, and Zn atomic percentages in ideally stoichiometric ZnMn₂O₄.

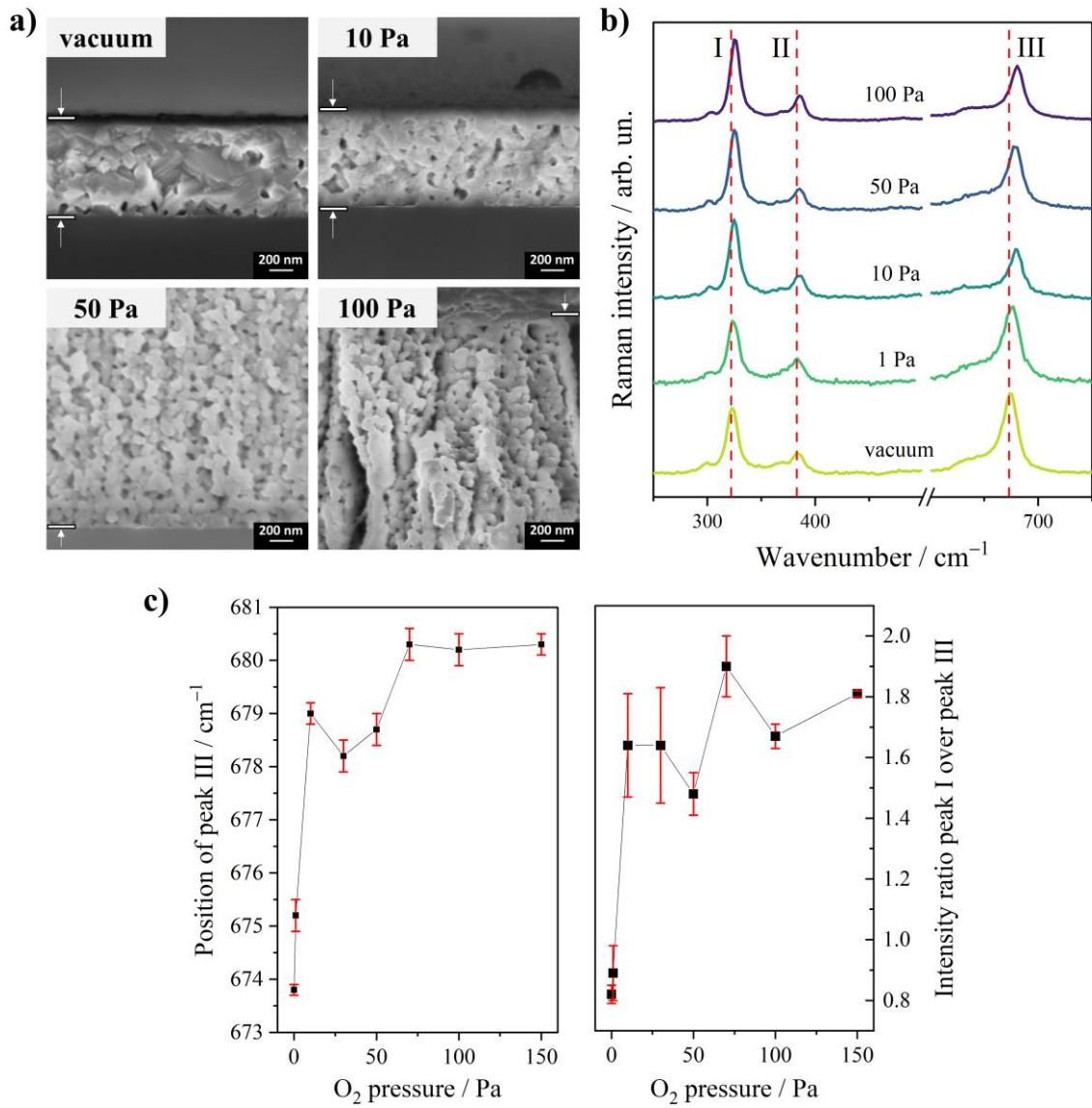


Fig. 3. (a) SEM cross-sectional images of the ZMO thin films air-annealed at 600 °C, 3h, and deposited on Si with constant laser fluence of $\sim 3.7 \text{ J cm}^{-2}$ and in vacuum, 10 Pa, 50 Pa, and 100 Pa of O₂. (b) Evolution of the Raman spectral features of crystallized samples as a function of the O₂ deposition pressure (the three main peaks are here labelled as I, II, and III). (c) Position of peak III (A_{1g} mode) and intensity ratio between peak I and peak III as a function of the O₂ deposition pressure.

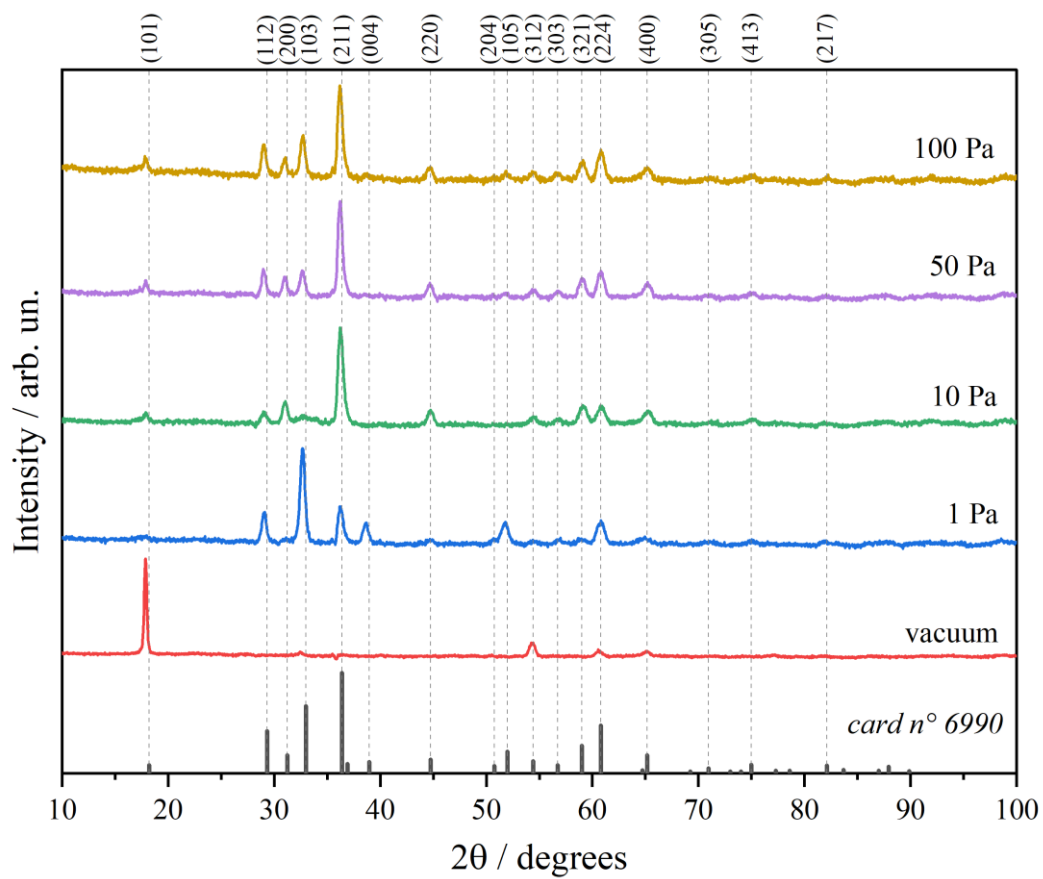


Fig. 4. GIXRD patterns of crystalline ZMO thin films, produced at different O₂ pressures and annealed in air at 600 °C, 3 h.

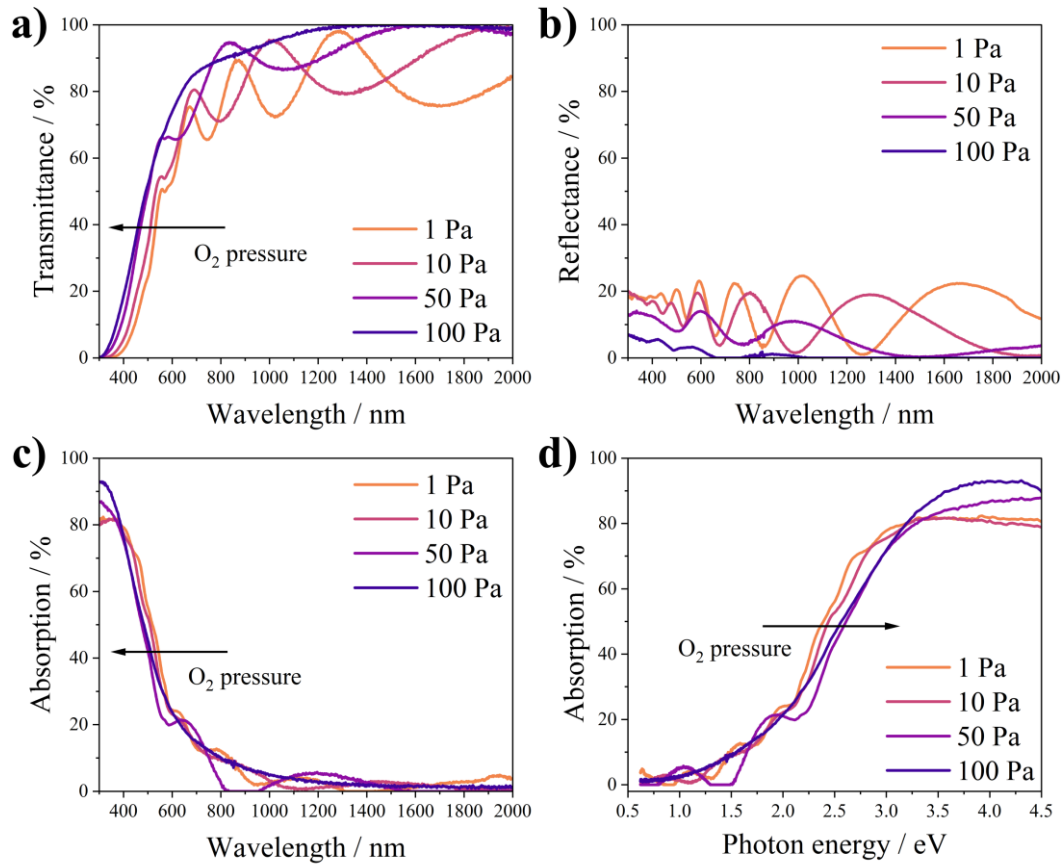


Fig. 5. UV-Vis (a) transmittance, (b) reflectance, and (c) absorption curves in the wavelength range 300–2000 nm of crystalline ZMO samples deposited at 1, 10, 50, and 100 Pa of O₂, and annealed in air at 500 °C for 2h. (d) UV-Vis absorption curves plotted as a function of photon energy in the range 0.5–4.5 eV.

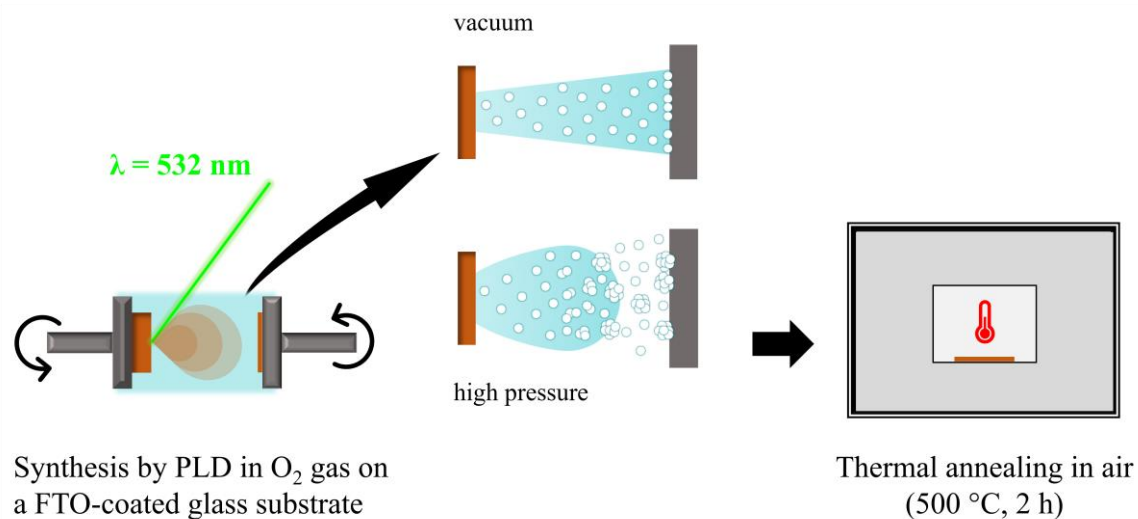


Fig. 6. Schematic illustration of the preparation of ZMO thin films for the purpose of the electrochemical characterization.

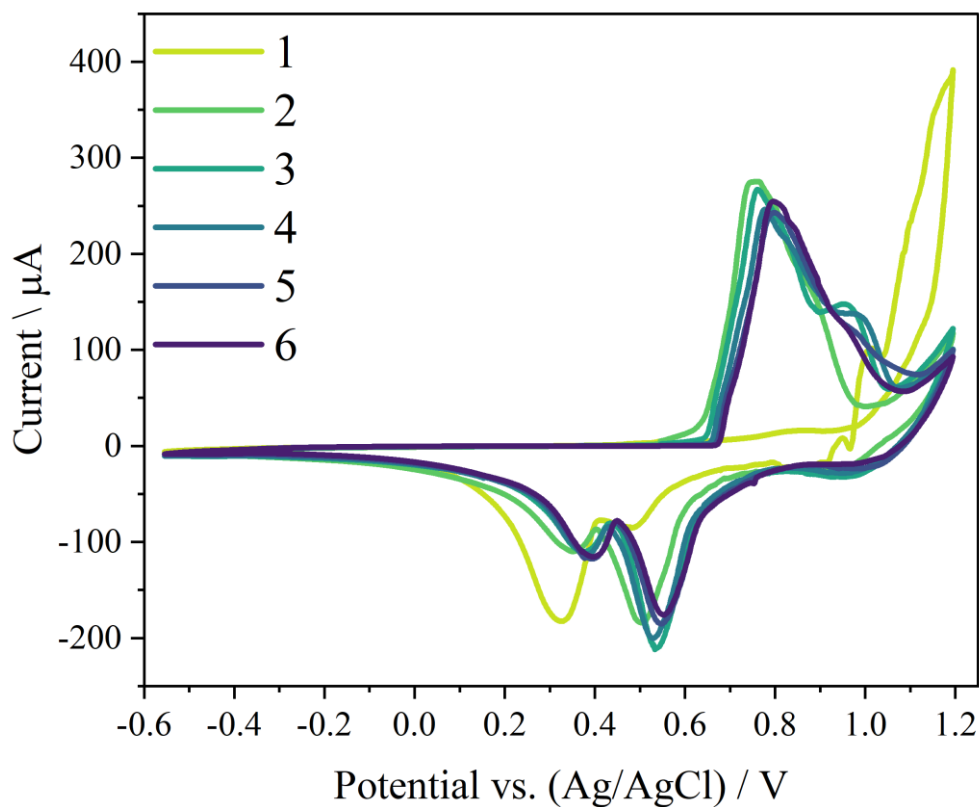


Fig. 7. CV curves at a scan rate of 1 mV s^{-1} of the ZMO thin film deposited at 50 Pa of O_2 and crystallized in air at $500 \text{ }^\circ\text{C}$, 2h.

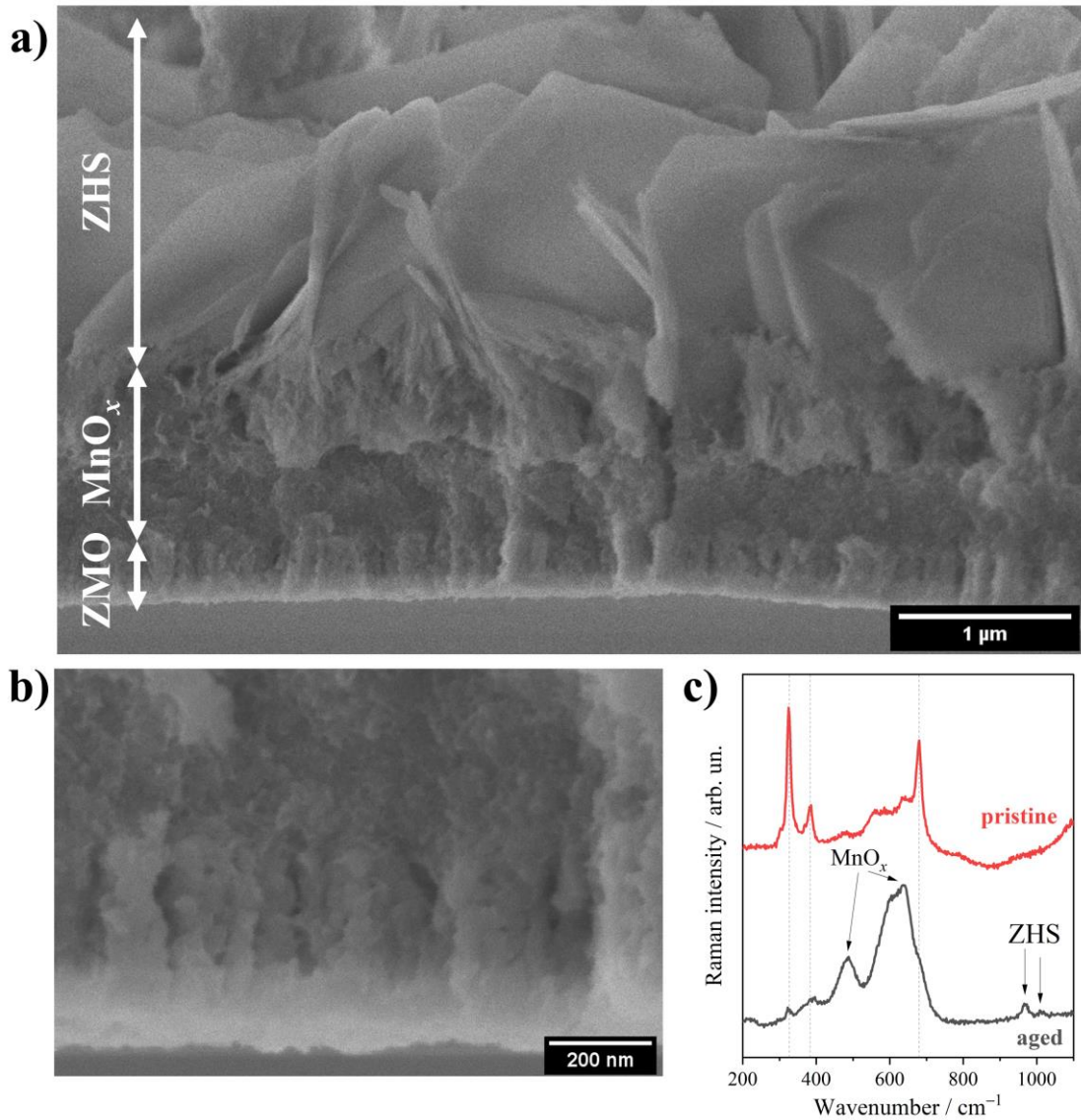


Fig. 8. SEM cross-sectional image of (a) the whole aged ZMO film and (b) the bottom layer after 6 CV cycles at 1 mV s⁻¹. (c) Raman spectra comparing the pristine (i.e., after annealing) and the aged film. The characteristic Raman features of MnO_x and ZHS phase are highlighted.

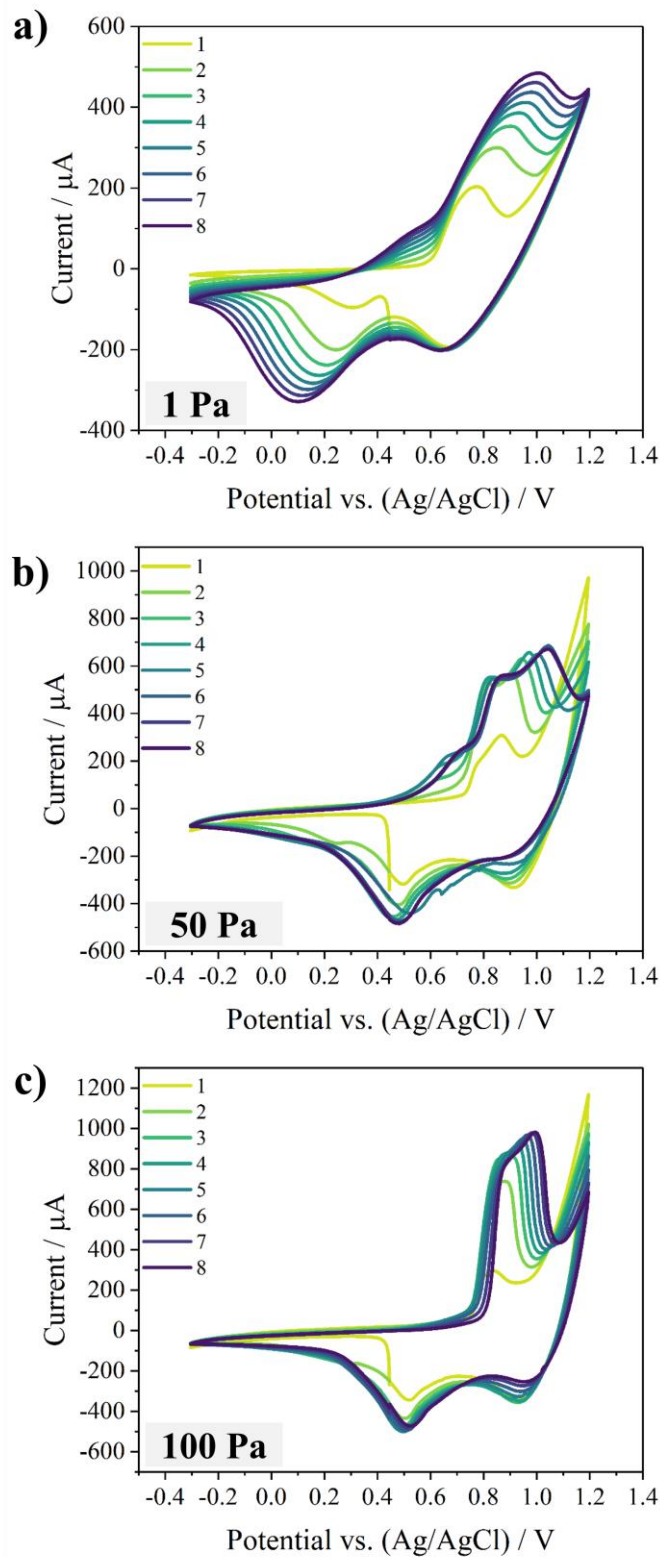


Fig. 9. CV curves at a scan rate of 25 mV s^{-1} of the ZMO films deposited at (a) 1, (b) 50, and (c) 100 Pa of O₂, and crystallized in air at 500 °C, 2h.

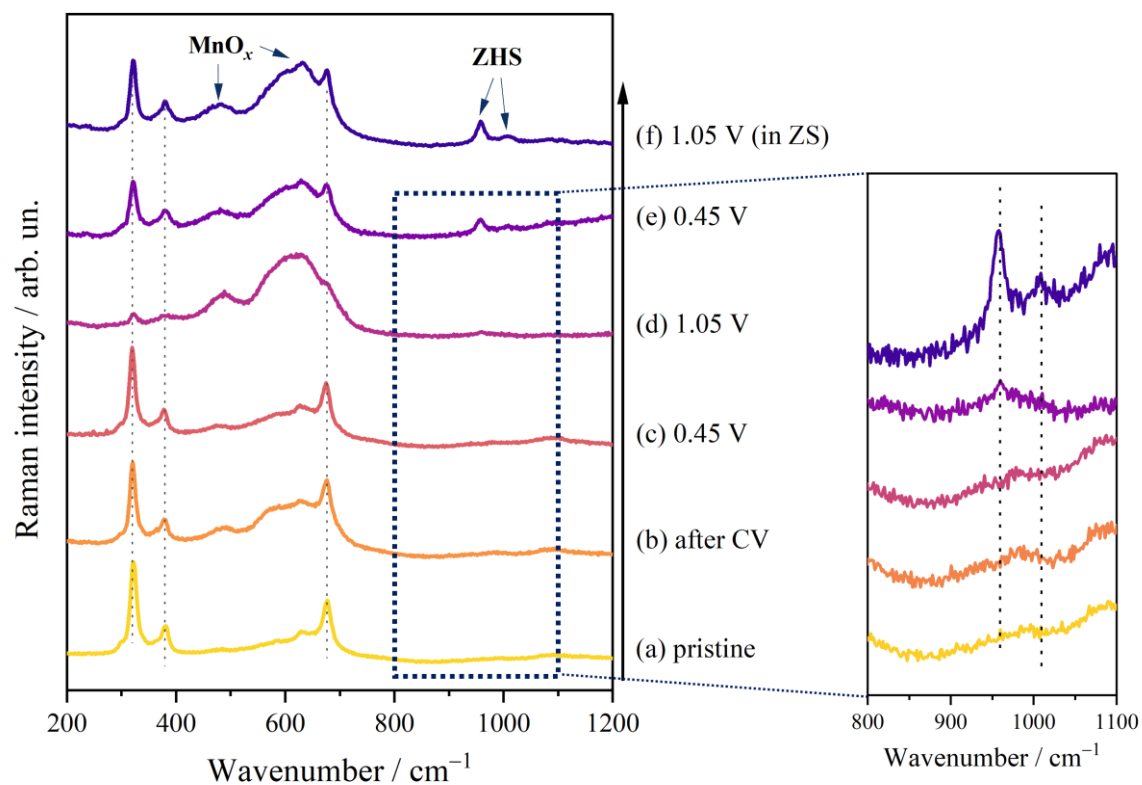
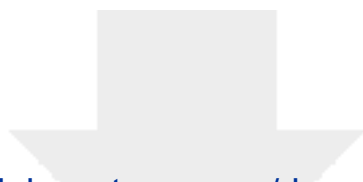


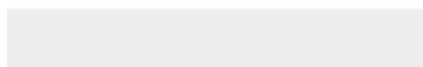
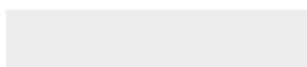
Fig. 10. Evolution of the quasi-*in situ* Raman spectra of a ZMO film (grown at 100 Pa of O₂ and annealed at 500 °C, 2h) during sequential electrochemical measurements. In the inset, the spectral region between 800 and 1100 cm⁻¹ is highlighted. Curves (a–e) were acquired after electrochemical polarization in ZMS electrolyte, while curve (f) was acquired after polarization in ZS electrolyte.



Click here to access/download

Supplementary Materials

5) Revised supplementary data.docx



CRedit authorship contribution statement

Andrea Macrelli: Conceptualization, Methodology, Validation, Formal Analysis, Investigation, Visualization, Writing – Original Draft, Writing – Review & Editing. **Marco Olivieri:** Formal Analysis, Investigation. **Alessio Lamperti:** Methodology, Investigation, Resources, Writing – Review & Editing. **Valeria Russo:** Methodology, Supervision, Writing – Review & Editing. **Benedetto Bozzini:** Conceptualization, Methodology, Formal Analysis, Resources, Writing – Review & Editing, Supervision. **Marco Menegazzo:** Methodology, Resources. **Gianlorenzo Bussetti:** Methodology, Resources. **Carlo S. Casari:** Conceptualization, Writing – Review & Editing, Supervision. **Andrea Li Bassi:** Conceptualization, Writing – Review & Editing, Supervision.